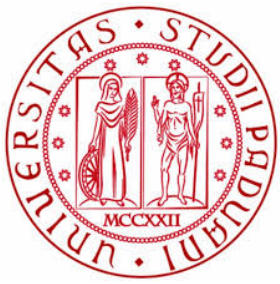

UNIVERSITÀ DEGLI STUDI DI PADOVA

DIPARTIMENTO DI SCIENZE CHIMICHE

CORSO DI LAUREA MAGISTRALE IN CHIMICA

TESI DI LAUREA MAGISTRALE

Coherent Dynamics in the Ultrafast Relaxation of BODIPY Dyes: 2D Electronic Spectroscopic Characterization

Relatore: Prof.ssa Elisabetta Collini
Controrelatore: Prof. Mauro Sambi

Laureando: Annalisa Polo

ANNO ACCADEMICO 2015/2016

Contents

Abstract

The work presented in this thesis deals with the investigation of the relaxation dynamics of molecules occurring after excitation, a process whereby the excess of energy provided to the molecule by the interaction with light is released. To this aim, we applied 2D electronic spectroscopy, a recently developed advanced optical technique now recognized as one of the best tool to capture the ultrafast relaxation dynamics occurring in the first picosecond after excitation. Indeed, its capability to reveal quantum coherent mechanisms acting during relaxation dynamics makes it one of the most powerful and informative spectroscopic techniques currently available. Recent experimental data obtained on biological light harvesting complexes suggested the presence of coherent effects during the electronic energy transport, surviving for times longer than expected even at physiological conditions. The understanding of this phenomenon in biological complexes and the possibility of control and engineer these effects in 'smart' artificial devices is one of the hottest topics across different communities. In this context, it is now agreed that environment, including surroundings and vibrations intrinsic to the molecular structure, plays a crucial role in the dynamics of coherences, being responsible of their manifestation as long-lived oscillations. Despite this, a systematic study on the role of the molecular structure, the nature of the vibrational modes and solvent involved in the coherent dynamics of the chromophores is still missing. The research activity described in this thesis aims to fill this gap. Indeed, we applied 2D spectroscopy to study the coherent relaxation dynamics of single chromophores as a function of their structure (i.e. mono or multi-branching, role of substituents, etc.), solvent and exciting bandwidth with the objective of identify possible 'structure-to-properties' relationships to be used in the design of multi-chromophoric systems with artificial light-harvesting capabilities. The attention has been focused in particular on organic dyes known as BODIPYs, structurally analogue to half-porphyrins, and thus possibly envisioned in the preparation of multi-chromophoric bio-mimetic systems. Particular attention was spent in understanding the effect of the introduction of specified substituents in significant positions of the BODIPY core and on the role of solvent in the ultrafast relaxation of these chromophores. The background of information acquired on these simplified systems is of pivotal importance for the characterization of quantum effects in energy transfer processes in dimers of BODIPY dyes, planned in the near future.

Abstract (Italiano)

Il lavoro presentato in questa tesi si occupa di investigare dinamiche di rilassamento di molecole a seguito di fotoeccitazione, un processo in cui la molecola rilascia l'eccesso di energia acquisito tramite l'interazione con la luce. A questo scopo, abbiamo applicato la spettroscopia elettronica 2D, una tecnica avanzata di spettroscopia ottica recentemente sviluppata, oggi riconosciuta come uno degli strumenti migliori per catturare la dinamica di rilassamento ultraveloce che ha luogo nel primo picosecondo a seguito dell'eccitazione. Infatti, la sua abilità nel rivelare meccanismi coerenti quantistici attivi durante il trasporto di energia elettronica, la rendono una delle più efficaci e informative tecniche di spettroscopia ad oggi disponibili. Recenti dati sperimentali ottenuti su complessi antenna biologici hanno suggerito la presenza di effetti coerenti durante il trasporto di energia elettronica, in grado di persistere per tempi maggiori di quelli attesi, persino in condizioni fisiologiche. La comprensione di questo fenomeno in complessi biologici e la possibilità di controllare e ingegnerizzare questi effetti in dispositivi artificiali, rappresenta una delle tematiche più di picco in diversi ambiti di ricerca. In questo contesto, ad oggi si è raggiunto un certo consenso sul fatto che l'ambiente, con cui si indica in modo generico sia l'intorno che le vibrazioni intrinseche alla struttura molecolare, rivesta un ruolo cruciale nella dinamica delle coerenze; si pensa infatti che l'interazione con l'ambiente sia responsabile del loro manifestarsi come oscillazioni di lunga durata. Nonostante ciò, uno studio sistematico sul ruolo della struttura molecolare, sulla natura dei modi vibrazionali e sul solvente, fattori coinvolti nella dinamica coerente dei cromofori, non è ancora ad oggi stato effettuato. L'attività di ricerca descritta in questa tesi ha lo scopo di colmare questa mancanza. Infatti, si è applicata la spettroscopia 2D allo studio della dinamica di rilassamento coerente di singoli cromofori in funzione della loro struttura (per esempio mono o multi ramificato, ruolo dei sostituenti, ecc.), del solvente e della banda di eccitazione con l'obiettivo di identificare possibili relazioni tra struttura e proprietà, da poter eventualmente utilizzare nel design di sistemi multicromoforici artificiali per *light-harvesting* artificiale. L'attenzione è stata focalizzata in particolare su coloranti organici noti come BODIPY, strutturalmente analoghi a metà porfirine, dunque potenzialmente utilizzabili nella preparazione di sistemi multicromoforici biomimetici. Particolare attenzione è stata inoltre rivolta alla comprensione dell'effetto del solvente e di specifici sostituenti introdotti in posizioni significative del BODIPY, sul rilassamento ultraveloce di questi cromofori. Il *background* di informazioni acquisite su questi sistemi semplificati è di centrale importanza per la caratterizzazione di effetti quantistici nei processi di trasferimento di energia in dimeri di BODIPY, pianificata per il futuro.

Introduction

The central role of Nature in human life has always stimulated interest about the laws that govern the dynamical evolution of natural processes. The failure of classical physics alone in interpreting life was debated by Erwin Schrodinger in 1943, who pioneered the idea that quantum principles are instead required [1], [2]. This observation was naturally followed by the question in Jordan's 1943 book "Are the law of atomic and quantum physics of essentially importance for life?" that introduced the extremely important concept of Quantum Biology [3]. It identifies "biological phenomena that make explicit use of quantum mechanics to attain functionalities or to carry out a process" [4]. While at the time the potential role of quantum physics in biology was essentially subjected to theoretical speculations, nowadays the progress in science and technology has lead to the revival of this interest by means of both theoretical and experimental explorations. Recently developed experimental tools have indeed provided the direct access to the observation of quantum effects in biological systems [1], [4], [5].

Why has quantum biology aroused growing excitement among the emergent fields of research? To answer this question we will explore the origins of the interplay between biological phenomena and quantum mechanics.

Life takes place out of the equilibrium state, therefore biological systems are continuously involved in energy exchanges and are referred as open systems, affected by environments [4], [6]. The main feature of quantum mechanics is to treat systems as superpositions of distinct physical states, leading to a probabilistic description of their evolution. While for a long time the influence of environment has been considered only in terms of suppression of quantum correlations between states, recent works have proven that constructive interplays between the quantum dynamical system and its environment are at the base of the quantum phenomena observed in biology [4]. The legitimate question is if quantum mechanisms actually play a specific role in improvement the functions of biological systems [1], [4], [7] and more importantly, if they can be exploited to improve the performances of man-made devices mimicking natural processes.

The best example in this sense is light harvesting and photosynthesis. Photosynthesis is the best example of how solar energy can be converted into a different form of energy more directly usable for the vital functions of the organisms. The parallelism with man-made devices able to capture solar light and convert it in electrical power is immediate. The first step of both natural and artificial processes is light-harvesting. i.e. the absorption of solar

light by the so-called antenna complexes and its efficient transport to reaction centres where it is exploited to start a series of charge separation reactions.

The ability of experimentally detect quantum mechanisms acting during energy transport, for example during light harvesting, is strongly connected with the recent development of 2D electronic spectroscopy (2DES), and 2D photon echo (2DPE) in particular.

2DPE, developed in the last decade, represents to date the most powerful tool to investigate subtle quantum effects in excitations relaxations in both biological and artificial light harvesting systems [1], [8]. The time and frequency resolution characterizing this technique allows following directly the evolution of quantum coherences in energy transfer processes. The possibility of experimentally detecting quantum coherences is indeed strictly correlated to the ability of excite the system with ultrashort laser pulses and being able of spreading the information contained in the final signals as function of 2 frequencies (2D frequency-frequency maps). In the eigenstate description, short laser pulses are required to prepare a superposition in which different eigenstates are excited in phase and emit to a final common level. These correlations between states in 2DES are detected as oscillations at the frequency matching the energy gap between two states coherently excited by laser. These oscillations are the main observable associated with quantum coherent dynamics and represent therefore the main focus of the spectroscopic analysis.

The application of 2DES techniques to the characterization of the energy transfer mechanisms and dynamics in several biological light-harvesting complexes lead to the discovery of astonishingly long lived oscillations in the optical response of these complexes.

These evidences suggested that these antenna proteins are able to capture and transfer energy according to quantum mechanical probability instead of classic laws, thus overpassing the classical limits for how fast and how far the excitation can migrate [9]. The most relevant evidence of efficient quantum energy transfer is represented by the detection in various light-harvesting systems of long-lived quantum coherences of sufficient duration to effectively funnel energy transport [10], providing robustness against energetic disorders and dynamical perturbations [11], [12]. Particularly, the observation that these observed coherences persist on time scales that are comparable to that of typical energy transfer in antennae systems, suggests that the coherent dynamics improves the function of the photosynthetic complex. However, in the presence of environmental noise, quantum features should be expected to be short-lived. As stated before, quantum correlations between states that survive for relatively long times are reasonably due to the coupling with favourable environment surrounding molecules. Coherences between electronic states dephase indeed very quickly at room temperature, and only the presence of suitable environmental fluctuations and vibrations

could help them to persist for longer times than expected or even to recreate after dephasing [7]. This demonstrates the relevance of environment surrounding molecules in their relaxation dynamics.

While the big claims of the last decade conjectured that long-lived coherences driving optimized energy transfer within photosynthetic systems are substantially of pure electronic nature [13], [14], recent works have demonstrated the crucial role of the coupling between electronic and vibrational degrees of freedom [15], [16]. This is what is known as "vibronic coupling" [15], [17]. This concept has been used for decades [18] but nowadays the interest on its description has been rejuvenated, despite the little agreement regarding the definition of "vibronic".

Generally speaking, the term "vibronic coupling" designates the general concept of the correction of electronic wavefunctions through the introduction of the coupling with vibrational degrees of freedom. Different models can be followed to this purpose, describing different microscopic mechanisms with different dephasing time scales [15]. The resulting scenario is that the interaction between coherently coupled electronic states and quasi-resonant vibrational modes of the molecular structure could sustain, regenerate, or even (re-) create long-lived room-temperature coherences [17].

Of course, the debate about how the coupling with vibrations and electronic transitions could sustain the detected long-lived coherences and the role of quantum transfer in natural processes is still open and stimulating a lot of questions. The observation of these robust, long-lasting quantum features in natural complexes has stimulated great interest in the researchers community because of the tremendous impact that their implications might have also in the design of artificial light-harvesting devices for the storage of solar energies [17], [19].

In this picture, the experimental detection of such mixed vibrational and electronic coherences and the interpretation of their influence in the overall energy transfer mechanism in multi-chromophoric complexes represent for sure a challenge, but it is of pivotal importance to understand the role of the molecular structure on the energy transfer efficiency. To better understand the fascinating phenomenon of coherent dynamics in energy migration, the preliminary knowledge of how quantum coherent phenomena affect the relaxation dynamics in single chromophores and which are the main structural factor regulating them is absolutely necessary. However, so far, a systematic study on the role of the molecular structure, the nature of the vibrational modes and solvent involved in the coherent dynamics of isolated chromophores is still missing.

This is indeed the object of this thesis. The idea is to deeply characterize the main factors influencing coherent dynamics trough the study of simplified model systems where the relationships between structure, vibrations and electronic properties are more easily identifiable. Focusing the attention on artificial dyes, the presence of quantum mechanisms in the ultrafast relaxation dynamics of chromophores known as BODIPYs has been analysed, a great example of biomimetic light-harvesters thanks to their structural analogy to the half-porphyrin moiety. Porphyrin systems are in turn the artificial analogue of chlorophylls, which are the main example of absorbers in natural photosyntesis. The characterization of these monomeric dyes is the first but not least important step of a more ambitious project, aiming to obtain further insights into the energy transfer process in dimers and multi-chromophores of BODIPY dyes linked by hydrogen bonds.

In light of the intimate correlation occurring between vibrational modes, the way they are coupled with electronic transitions and the molecular structure and the environment where chromophores are embedded, different are the aspects we propose to study by means of 2DPE technique.

Taking advantage of the ability of 2DPE in providing a great amount of information about the ultrafast dynamics of systems, the main aim of this thesis is the study of how the molecular structure, the interaction with solvent and the introduction of specific substituents in relevant positions of the molecular core may affect the relaxation dynamics of BODIPY dyes. To this purpose, the modulation of the electronic properties of these chromophores as a function of the molecular structure is preliminarily analysed by means of linear techniques applied to a great variety of differently substituted dyes. These analyses have allowed selecting the most interesting aspects to investigate through 2D spectroscopy. The 2D characterization of the main vibrations involved in the coherent coupling with electronic transition has been supported by Raman spectroscopy, which allows identifying the vibrational modes active in the ground state manifold of a system.

The dissertation is structured into four Chapters:

Chapter 1 provides a theoretical background necessary to understand the foundations of the optical techniques employed and to grasp the physical meaning of the observables experimentally measured. It is particularly focused on the formalism of the response function that provides the description of the optical response of a system at any order of perturbation.

Chapter 2 offers an insight on BODIPYs chemistry with a detailed description of all the investigated dyes and the experimental results of the linear characterization performed trough Absorption and Fluorescence spectroscopies. The results of the vibrational

characterization performed by means of Raman spectroscopy on selected samples are also presented.

Chapter 3 describes the experimental setup available in our lab to perform 2DPE measurements and the suitable analysis toolbox developed for data processing and interpretation.

Chapter 4 treats the experimental results of 2D characterization performed on the selected samples. Specifically, the influence of solvent and of certain substituents with different implications on the chemistry of the molecular core, on the ultrafast relaxation dynamics of BODIPY dyes is the focus of this analysis. The sets of measurements performed have been distributed in order to investigate the relaxation dynamics following the excitation of two different spectral regions.

Chapter 1

Response function formalism

1.1 Introduction

Optical spectroscopies can be firstly classified according to their power-law dependence on the external electric field. The key quantity is the so-called *optical polarization*, which represents the relevant macroscopic quantity induced in the material as a response of light perturbation. Denoting with $P^{(n)}$ the component of n^{th} order in the field, the polarization can be generally expressed through the following expansion:

$$P = P^{(1)} + P_{NL} \tag{1a}$$

$$P_{NL} = P^{(2)} + P^{(3)} + \cdots \tag{1b}$$

$P^{(1)}$ is the linear polarization related to processes such as absorption, light propagation, reflection and refraction, which involve a weak incoming perturbation. Nonlinear polarization is represented by the higher orders of the expansion and is connected with nonlinear spectroscopy [20].

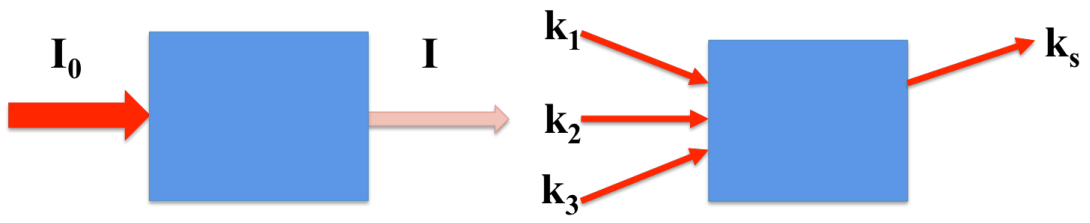

a) b)

Figure 1.1 Schematic representation of (a) absorption spectroscopy. Attenuation of an incident beam by the medium. (b) Example of nonlinear spectroscopy: four wave-mixing. Three incident beams $\mathbf{k}_1$, $\mathbf{k}_2$ and $\mathbf{k}_3$ generate a coherent signal $\mathbf{k}_s$ in one of the phase matched directions $\mathbf{k}_s = \mathbf{k}_1 + \mathbf{k}_2 + \mathbf{k}_3$.

As we will see in the following treatment, the polarization components are correlated to the different orders of the response function, a real observable quantity that describes how an

equilibrium system changes in response to a perturbation from a microscopic point of view [21].

Among the different physical models for the treatment of the interaction between light and matter [22], the perturbation theory is the most widely used tool to describe the different orders of perturbation at which the interaction occurs. In this approach, light, a purely classical oscillating field, interacts with the quantum states of the molecule, according to a semiclassical treatment [21].

In the perturbative approach the time-varying electromagnetic field is treated as a small perturbation on the quantum system, so that the total Hamiltonian can be expressed as the sum of a zero-order part H_0 that does not depend on time, and the time dependent perturbation H′(t) [23]. This is because in general the interaction with the electric field is much weaker than the internal fields of the molecule, thus can be treated perturbatively. It is assumed that the stationary states $|n\rangle$ of the molecule, solutions of the zero-order Hamiltonian H_0, are known. The time-dependent Schrödinger equation, which describes the evolution of a quantum system in terms of wavefunctions [24], takes the form:

$$[\mathcal{H}_0 + \mathcal{H}'(t)]\,|\psi\rangle = i\hbar\frac{\partial}{\partial t}|\psi\rangle \tag{2}$$

The eigenfunctions $|n\rangle$ of H_0 with associated eigenvalues E_n, are orthonormal and form a complete set, thus they can be used as a basis for expanding the perturbed wavefunction:

$$|\psi\rangle = \sum_n c_n\,(t)|n\rangle e^{\frac{-i(E_n)t}{\hbar}} \tag{3}$$

In the Schrödinger representation of the perturbed state as superposition of the stationary states, the time dependence is included in the phase factor $e^{\frac{-i(E_n)t}{\hbar}}$ and in the coefficients $c_n(t)$. The physical meaning of this relationship can be grasped analysing the following expression, which derives from substitution of the perturbed wavefunction in the time-dependent Eqn. 2, after some manipulations:

$$\frac{\partial c_n}{\partial t} = -\left(\frac{i}{\hbar}\right)\langle n|\mathcal{H}'|0\rangle e^{\frac{-i(E_n-E_0)t}{\hbar}} \quad , \quad n \neq 0 \tag{4}$$

It describes what happens when a weak electromagnetic field acts on an unperturbed system. We can assume that at equilibrium conditions only the lowest energy eigenstate 0 is populated, so that the coefficients relative to the excited states are zero, while $c_0 = 1$. The effect of light perturbation is thus to induce the population of the excited states, in the manner described by the time dependence of the relative coefficients.

1.2 Density matrix formalism

The density matrix or density operator is an alternative representation of the state of a quantum system, which results significantly advantageous to treat time-dependent problems, particularly relaxation and nonlinear spectroscopy in the condensed phase [21]. In condensed phase systems, we have in general to deal with statistical ensembles rather than pure states. While the behaviour of a pure state can be equally described using the wavefunction or the density matrix, the only way to treat a statistical average is to introduce the density matrix formalism [20], [25].

The density matrix is defined as the outer product of the wavefunction with its conjugate:

$$\rho \equiv |\psi(t)\rangle\langle\psi(t)| \tag{5}$$

This expression implies that, for a given state $|\chi\rangle$, the matrix element $\langle\chi|\rho|\chi\rangle$ represents the probability of finding a particle in the state $|\chi\rangle$ [21].

The elements of the density matrix can be obtained from Eqn. 5, considering the expansion of the wavefunction in the orthonormal basis $|n\rangle$:

$$\rho(t) = \sum_{n,m} c_n(t)c_m^*(t)|n\rangle\langle m| \equiv \sum_{n,m} \rho_{nm}|n\rangle\langle m| \rightarrow \rho_{nm}(t) \equiv c_n(t)c_m^*(t) \tag{6}$$

As we can see, the density matrix elements are expressed in terms of the time-evolving expansion coefficients.

Since the expectation value of an operator *A* takes the form:

$$\langle A(t)\rangle = \langle\psi(\mathrm{t})|\tilde{A}|\psi(\mathrm{t})\rangle = \sum_{n,m} c_n(t)c_m^*(t)\langle m|\tilde{A}|n\rangle \tag{7}$$

in the density matrix representation we can obtain:

$$\langle\tilde{A}(t)\rangle = \sum_{n,m} A_{mn}\rho_{nm}(t) = Tr\left[\tilde{A}\rho(t)\right] \tag{8}$$

meaning that expectation values can be evaluated simply by the trace over the product of matrices.

The main advantage of this formalism is that it enables us to distinguish populations from coherences. The diagonal elements ($n = m$) represent the probability to find a system at time *t* in a quantum state *n*, thus are referred to as populations:

$$\rho_{nn} = c_n c_n^* = p_n \geq 0 \tag{9}$$

The off-diagonal elements ($n \neq m$), instead, describe the oscillatory behaviour of coherent superpositions in the system, therefore are denoted as coherences [21]:

$$\rho_{nm} = c_n(t)c_m^*(t) = c_n c_m^* e^{-i\omega_{nm}t} \tag{10}$$

As we can see, they are complex and depend on the phase factor.

The density matrix formalism is particularly convenient to treat mixed states related to statistical ensembles, when we do not have complete information about the system and the only way to describe quantum observables is to perform statistical averages [21]. Therefore, the calculation of expectation values for mixed states cannot be made in terms of wavefunction and is greatly simplified by means of the density matrix.

The time evolution of the density matrix can be expressed by the *Liouville-Von Neumann* equation, which naturally follows from the definition of ρ and the time-dependent Schrödinger equation:

$$\frac{\partial}{\partial t}\rho = \frac{\partial}{\partial t}[|\psi\rangle\langle\psi|] = \frac{-i}{\hbar}[\mathcal{H}, \rho] \tag{11}$$

Let us consider the simple case of the two-level system characterized by the time-independent Hamiltonian [20]:

$$\mathcal{H} = \begin{pmatrix} \varepsilon_1 & 0 \\ 0 & \varepsilon_2 \end{pmatrix} \tag{12}$$

From the application of the equation of motion for the density matrix we get:

$$\frac{\partial}{\partial t}\begin{pmatrix} \rho_{11} & \rho_{12} \\ \rho_{21} & \rho_{22} \end{pmatrix} = -\frac{i}{\hbar}\begin{pmatrix} 0 & (\varepsilon_1 - \varepsilon_2)\rho_{12} \\ (\varepsilon_2 - \varepsilon_1)\rho_{21} & 0 \end{pmatrix} \tag{13}$$

thus it follows that:

$$\rho_{ii}(t) = \rho_{ii}(0) \tag{14}$$

$$\rho_{ij}(t) = e^{\mp\frac{(\varepsilon_i - \varepsilon_j)}{\hbar}}\rho_{ij}(0) \tag{15}$$

From this we see that populations are stationary in time, while coherences oscillate at a frequency corresponding to the energy splitting between the two states.

1.3 Perturbative expansion

The time evolution of a quantum system interacting with a weak light perturbation can be better described moving to the interaction picture and introducing the time evolution operator with respect to the system Hamiltonian H_0 [25], [20], [21], defined as follows:

$$U_0(t,t_0) = e^{\frac{-iH_0(t-t_0)}{\hbar}} \tag{16}$$

The new wavefunction in the interaction picture can be defined as:

$$|\psi(t)\rangle = U_0(t,t_0)|\psi_I(t)\rangle \tag{17}$$

where the subscript *I* denotes the interaction picture. $\psi(t)$ is the wavefunction relative to the full Hamiltonian H(t), whereas $U_0(t,t_0)$ is the time evolution operator with respect to the unperturbed Hamiltonian H_0 only. Hence, the time dependence of $\psi_I(t)$ describes the time evolution of the wavefunction caused by the difference between H(t) and H_0, which corresponds to the weak perturbation term H′(t) [20].

The Schrödinger equation can be now rewritten in terms of the only perturbative Hamiltonian operator:

$$\frac{\partial|\psi_I(t)\rangle}{\partial t} = -\frac{i}{\hbar}\mathcal{H}'(t)|\psi_I(t)\rangle \tag{18}$$

In the case of multiple field-matter interactions, as when we consider the polarization induced by a sequence of time-ordered laser pulses acting on the sample, it is useful to integrate iteratively the previous equation in the different time intervals:

$$|\psi_I(t)\rangle = |\psi_I(t_0)\rangle - \frac{i}{\hbar}\int_{t_0}^{t}\mathcal{H}_I'(t)|\psi_I(t)\rangle = \tag{19}$$

$$= |\psi_I(t_0)\rangle$$

$$+ \sum_{n=1}^{\infty}\left(-\frac{i}{\hbar}\right)^n \int_{t_0}^{t} d\tau_n \int_{t_0}^{\tau_n} d\tau_{n-1} \dots \int_{t_0}^{\tau_2} d\tau_1 \mathcal{H}_I'(\tau_n)\mathcal{H}_I'(\tau_{n-1}) \dots \mathcal{H}_I'(\tau_1)|\psi_I(t_0)\rangle$$

where the sequence $t_0 \rightarrow \tau_1 \rightarrow \tau_2 \rightarrow \tau_3 \dots \tau_n \rightarrow t$ represents the time intervals in which the perturbation acts.

Going back to the Schrödinger picture, after some algebraic manipulations, we obtain:

$$|\psi(t)\rangle \tag{20}$$
$$= |\psi^0(t)\rangle + \sum_{n=1}^{\infty}\left(-\frac{i}{\hbar}\right)^n \int_{t_0}^{t} d\tau_n \int_{t_0}^{\tau_n} d\tau_{n-1} \dots \int_{t_0}^{\tau_2} d\tau_1$$
$$\times U_0(\tau_n, t_0)\mathcal{H}_I{}'(\tau_n)U_0(\tau_n, \tau_{n-1})\mathcal{H}_I{}'(\tau_{n-1}) \dots U_0(\tau_1, t_0)\mathcal{H}_I{}'(\tau_1)|\psi_I(t_0)\rangle$$

The physical meaning of this expression is that the system evolves freely according to the time evolution operator for the unperturbed Hamiltonian, until time τ_1. At time τ_1 the system is perturbed by $H_I'(\tau_1)$, and subsequently propagates freely until the second perturbation occurs at time τ_2, and so on [20].

A similar expression can be derived in terms of the density matrix, which is particularly useful, as already anticipated, for the description of relaxation in multilevel systems, where it provides a simple notation for both populations of quantum states and coherences between them. To this end, making use of the relation:

$$\mathcal{H}_I{}'(t) = -E(t) \cdot \mu_I(t) \tag{21}$$

which expresses the perturbation in terms of interaction between the electric field and the dipole moment, we obtain:

$$\rho(t) = \rho^0(t) + \sum_{n=1}^{\infty}\left(-\frac{i}{\hbar}\right)^n \int_{t_0}^{t} d\tau_n \int_{t_0}^{\tau_n} d\tau_{n-1} \dots \int_{t_0}^{\tau_2} d\tau_1 E(\tau_n)E(\tau_{n-1}) \dots E(\tau_1) \tag{22}$$
$$\times U_0(t, -\infty)\left[\mu_I(\tau_n)[\mu_I(\tau_{n-1}) \dots [\mu_I(\tau_1), \rho(-\infty)] \dots]\right]U_0^{\dagger}(t, -\infty)$$

This equation represents the expansion at the n^{th} order of the density matrix in the perturbative limit, where each order accounts for the dipole interaction at a specific time between the system and the electromagnetic field. It results particularly useful in describing nonlinear signals deriving from interaction with *n* electromagnetic fields.

1.4 Polarization in nonlinear spectroscopy

The macroscopic polarization induced in the material by light perturbation give us a connection between the n^{th} order expansion of the density matrix and the nonlinear optical response.

In linear optics the polarization depends linearly on the electric field *E* [20]:

$$P = \varepsilon_0 \chi^{(1)} \cdot E \tag{23}$$

with ε_0 the vacuum dielectric constant and $\chi^{(1)}$ the linear susceptibility. In the presence of intense electric fields, nonlinear effects acquire relevance and we have to consider the expansion of the polarization in powers of the electric field:

$$P = \varepsilon_0\left(\chi^{(1)} \cdot E + \chi^{(2)} \cdot E \cdot E + \chi^{(3)} \cdot E \cdot E \cdot E + \cdots\right) \tag{24}$$

where $\chi^{(n)}$ are the n^{th} order nonlinear susceptibilities. Since the electric field is a vector, linear and nonlinear susceptibilities are tensors.

The macroscopic polarization can be also derived from the expectation value of the dipole operator μ:

$$P(t) = Tr\left(\mu\rho(t)\right) \equiv \langle\mu\rho(t)\rangle \tag{25}$$

For example, in the case of a two-level system:

$$\mu = \begin{pmatrix} 0 & \mu_{12} \\ \mu_{21} & 0 \end{pmatrix} \tag{26}$$

and we obtain for the polarization:

$$\langle\mu\rho(t)\rangle = \left\langle \begin{pmatrix} 0 & \mu_{12} \\ \mu_{21} & 0 \end{pmatrix} \begin{pmatrix} \rho_{11} & \rho_{12} \\ \rho_{21} & \rho_{22} \end{pmatrix} \right\rangle = \rho_{12}\mu_{21} + \rho_{21}\mu_{12} \tag{27}$$

We can see that the macroscopic polarization is only made by off-diagonal elements of the density matrix, which thus emit light.

Substituting Eqn. 22 in 25 and writing explicitly the electric field E, we can see that the expansion of the density matrix corresponds to the increasing orders of nonlinear polarization in Eqn. 24, so that:

$$P^{(n)}(t) = \left\langle\mu\rho^{(n)}(t)\right\rangle \tag{28}$$
$$= \left(-\frac{i}{\hbar}\right)^n \int_{t_0}^{t} d\tau_n \int_{t_0}^{\tau_n} d\tau_{n-1} \dots \int_{t_0}^{\tau_2} d\tau_1 E(\tau_n)E(\tau_{n-1}) \dots E(\tau_1)$$
$$\times\langle\mu(t)[\mu(\tau_n)[\mu(\tau_{n-1}) \dots [\mu(\tau_1), \rho(-\infty)] \dots]]\rangle$$

Now, we replace the time variables τ_n, denoting absolute time points, with time intervals between the interactions with the electric fields, choosing τ_1=0 for the first interaction. In this way, we arrive at the following expression for the nonlinear polarization $P^{(n)}$:

$$P^{(n)}(t) = \left(-\frac{i}{\hbar}\right)^n \int_0^\infty dt_n \int_0^\infty dt_{n-1} \int_{t_0}^{\tau_2} dt_1 E(t-t_n)E(t-t_n-t_{n-1}) \ldots \quad (29)$$

$$E(t-t_n-t_{n-1} \ldots - t_1) \times S^{(n)}(t_n, t_{n-1}, \ldots t_1)$$

where $S^{(n)}$ is the nth nonlinear response function:

$$S^{(n)}(t_n, t_{n-1}, \ldots, t_1) = \left(-\frac{i}{\hbar}\right)^n \langle \mu(t_n + \cdots t_1)[\mu(t_{n-1} + \cdots t_1) \ldots [\mu(0), \rho(-\infty)] \ldots]\rangle \quad (30)$$

The nonlinear polarization induced in the sample is thus given by the convolution of the various optical fields with the response function. It is important to notice the role of the last interaction $\mu(t_n + t_{n-1} + \cdots t_1)$, which is no part of the commutator, compared to the previous interactions. The interactions at all the other times in the series of commutators generate a non-equilibrium density matrix whose off-diagonal elements emit a radiation, and the last interaction acts as a probe.

The third-order response function is the lowest accessible in nonlinear spectroscopy of isotropic media such as chromophores dissolved in solution.

The commutator in Eqn. 30 contains, explicitly, 2^n terms, with the various interactions acting either on the left side (ket) or the right side (bra) of the density matrix. For example, in the case of the third order response function (n=3) we have [20]:

$$\left\langle \mu(t_3+t_2+t_1)\left[\mu(t_2+t_1),\left[\mu(t_1),[\mu(0),\rho(-\infty)]\right]\right]\right\rangle = \quad (31)$$

$$= \langle \mu(t_3+t_2+t_1)\mu(t_2+t_1)\mu(t_1)\mu(0)\rho(-\infty)\rangle$$
$$-\langle \mu(t_3+t_2+t_1)\mu(t_2+t_1)\mu(t_1)\rho(-\infty)\mu(0)\rangle$$
$$-\langle \mu(t_3+t_2+t_1)\mu(t_2+t_1)\mu(0)\rho(-\infty)\mu(t_1)\rangle$$
$$+\langle \mu(t_3+t_2+t_1)\mu(t_2+t_1)\rho(-\infty)\mu(0)\mu(t_1)\rangle$$
$$-\langle \mu(t_3+t_2+t_1)\mu(t_1)\mu(0)\rho(-\infty)\mu(t_2+t_1)\rangle$$
$$+\langle \mu(t_3+t_2+t_1)\mu(t_1)\rho(-\infty)\mu(0)\mu(t_2+t_1)\rangle$$
$$+\langle \mu(t_3+t_2+t_1)\mu(0)\rho(-\infty)\mu(t_1)\mu(t_2+t_1)\rangle$$
$$-\langle \mu(t_3+t_2+t_1)\rho(-\infty)\mu(0)\mu(t_1)\mu(t_2+t_1)\rangle$$

We can see that each term has a conjugate complex.

1.5 Double Sided Feynman Diagrams

The response function can be thus seen as the sum of many interactions acting both on the ket and bra of the density matrix [20], [25], [26]. A pictorial and useful way to visualize all these interactions is given by Feynman diagrams, which represent the time evolution of the ket and bra of the density matrix trough vertical lines on the left and the right side,

respectively. In these diagrams time is vertically increasing and arrows pointing in or out the time lines denote the interactions with the dipole operator, absorption and emission of radiation, respectively.

The series of absorption and stimulated emission events shown in each diagram have a conjugate complex, according to what seen in the explicit expression of the commutator for third-order response function in Eqn. 31. By convention, only diagrams with the last interaction emitting from the ket are usually shown [20]. The last interaction corresponds to emission of light, thus it always points away from the lines. Because of its different nature, as described in the previous section, it is indicated using a different arrow. Note also that its frequency and wavevector are the sum of that of all the input pulses, according to the momentum and energy conservation of the system.

Each diagram represents a virtual path, known as Feynman path, developing trough real or virtual states coupled at each interaction point by the perturbation ω. The sum of all the possible Feynman diagrams combinations corresponds to the total n^{th} response function.

Let's start from the simplest case of the linear response for a two-level system, made up of the states $|g\rangle$ and $|e\rangle$:

$$S^{(1)}(t_1) = -\frac{i}{\hbar}\left(\langle\mu(t_1)\mu(0)\rho(-\infty)\rangle - \langle\mu(t_1)\mu(0)\rho(-\infty)\rangle^*\right) \tag{32}$$

The Feynman diagrams corresponding to the two terms of the equation are:

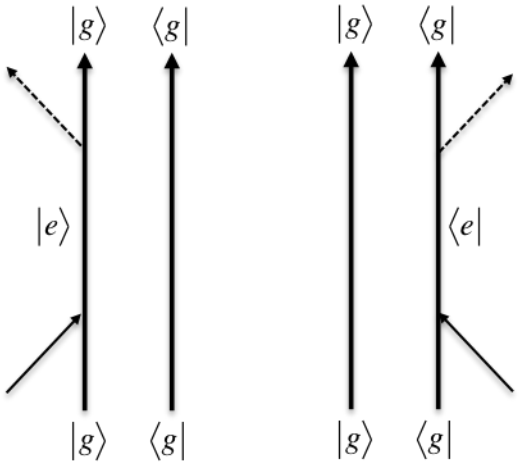

Figure 1.2 Feynman diagrams describing the terms which contribute to the linear response of a two-level system.

The density operator of the unperturbed system is in a ground state population. At t=0 the interaction with a laser pulse occurs and a coherence between the ground and the excited state is generated. During the time interval t_1 the coherence emits a polarization, whose decay restores the ground state population. This process describes a free induction decay,

whose Fourier Transform allows obtaining the absorption lineshape relative to the $|g\rangle\langle e|$ transition. We have reported for example in Figure 1.2 the two complex conjugate diagrams referring to the two terms in Eqn. 32. From now on we will focus only to the set of diagrams representing the last emission of light from the left side.

For the purpose of studying the evolution of excited states, the interaction with at least three pulses is necessary. Nonlinear optical phenomena described in this work are related to the third order response function [27]:

$$S^{(3)}(t_1, t_2, t_3) = -\frac{i}{\hbar^3}\langle \mu(t_3 + t_2 + t_1)[\mu(t_2 + t_1)[\mu(t_1)[\mu(0), \rho(-\infty)]]]\rangle \tag{33}$$

From the expansion of the commutators, which is already reported in Eqn. 34, it results that the expression for $S^{(3)}$ is composed by 8 terms, i.e. 4 pairs of Hermitian conjugates:

$$\Big\langle \mu(t_3 + t_2 + t_1)\Big[\mu(t_2 + t_1), [\mu(t_1), [\mu(0), \rho(-\infty)]]\Big]\Big\rangle = \tag{34}$$

$$\begin{aligned}
&= \langle \mu(t_3 + t_2 + t_1)\mu(t_2 + t_1)\mu(t_1)\mu(0)\rho(-\infty)\rangle && \Longrightarrow R_4 \\
&-\langle \mu(t_3 + t_2 + t_1)\mu(t_2 + t_1)\mu(t_1)\rho(-\infty)\mu(0)\rangle && \Longrightarrow R_1^* \\
&-\langle \mu(t_3 + t_2 + t_1)\mu(t_2 + t_1)\mu(0)\rho(-\infty)\mu(t_1)\rangle && \Longrightarrow R_2^* \\
&+\langle \mu(t_3 + t_2 + t_1)\mu(t_2 + t_1)\rho(-\infty)\mu(0)\mu(t_1)\rangle && \Longrightarrow R_3 \\
&-\langle \mu(t_3 + t_2 + t_1)\mu(t_1)\mu(0)\rho(-\infty)\mu(t_2 + t_1)\rangle && \Longrightarrow R_3^* \\
&+\langle \mu(t_3 + t_2 + t_1)\mu(t_1)\rho(-\infty)\mu(0)\mu(t_2 + t_1)\rangle && \Longrightarrow R_2 \\
&+\langle \mu(t_3 + t_2 + t_1)\mu(0)\rho(-\infty)\mu(t_1)\mu(t_2 + t_1)\rangle && \Longrightarrow R_1 \\
&-\langle \mu(t_3 + t_2 + t_1)\rho(-\infty)\mu(0)\mu(t_1)\mu(t_2 + t_1)\rangle && \Longrightarrow R_4^*
\end{aligned}$$

However, substituting these terms into the convolution integral in Eqn. 29, we obtain a third order polarization consisting of 864 terms, which are the permutations of all possible Feynman paths [20]. The treatment of a signal with this considerable number of contributions is complex, thus it is very difficult to extract information. Fortunately, suitable experimental conditions provide selectivity for some terms of the total response which will contribute to the measured polarization [20], [27]:

- Time ordering: if the laser pulses are shorter than the time delays between them, it is reasonably to assume that each interaction arises from each field.
- Rotating Wave approximation: only one of the exponential terms $e^{\pm i\omega t}$ is responsible of a significant interaction with the system.
- Phase Matching: the wavevector of the signal derives from the combination of the wavevectors of the incident fields, so that it is possible to experimentally select a

particular direction of the emitted radiation. In this way, only some group of Feynman paths contribute to the selected signal.

As example we report the phase matching relative to the experiment described in this work (Figure 1.3).

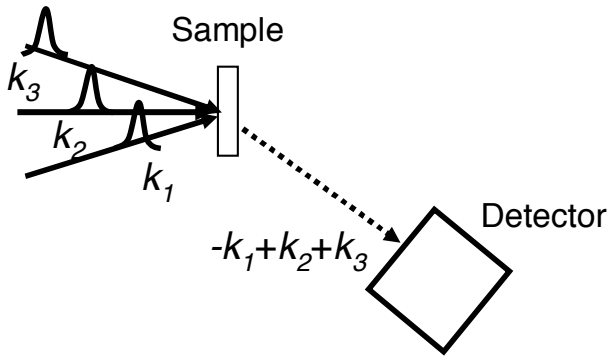

Figure 1.3 Phase matching for the rephasing contribution of the 2D Photon Echo experiment. The detector is put in the direction $-\mathbf{k}_1+\mathbf{k}_{2+}\mathbf{k}_3$, thus selecting only the R_2 and R_3 diagrams [20].

Under the experimental conditions the third order response function for a two-level system would be reduced to only 4 (and their complex conjugate) terms R_n corresponding to the Feynman diagrams in Figure 1.4 [20]:

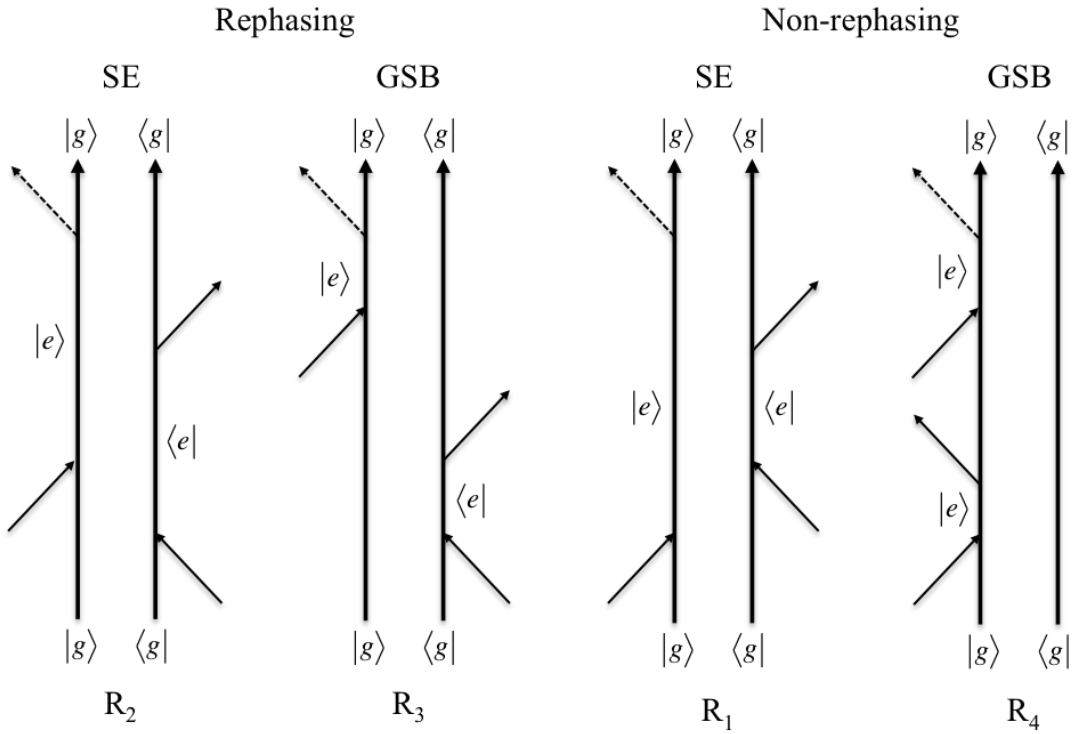

Figure 1.4 Feynman diagrams corresponding to different Feynman paths contributing to the third order response, classified as SE and GSB.

R_1 and R_2 Feynman paths correspond to a process known as stimulated emission (SE) and are the ideal terms to study the evolution of excited states along t_2. The first two pulses generate

the pure excited state $|e\rangle\langle e|$ and the third interaction stimulates the emission of the third order signal.

R_3 and R_4 Feynman paths correspond to ground state bleaching (GSB) process, in which the evolution along t_2 time interval is relative to ground state. R_1 and R_2 Feynman paths cannot be separated from R_3 and R_4 in any experimental conditions. However, phase matching conditions allow separating R_2 and R_3 Feynman paths, collected in the so-called rephasing configuration, from R_1 and R_4, known as non-rephasing paths. In the two cases the signal is recorded in the phase matching directions $k_s=-k_1+k_2+k_3$ and $k_s=k_1-k_2+k_3$, respectively.

As we can see from the Feynman diagrams in Figure 1.4, in the rephasing paths R_2 and R_3 the coherences during t_1 and t_3 are conjugated, meaning that the phase during these two time periods evolves in opposite direction, allowing for the emission of a photon-echo. The opposite is true for R_3 and R_4 paths, which maintain the same phase for coherences evolving during the two time intervals; for this reason, they are referred as non-rephasing contributions.

If at least a second excited state at about double the energy of the laser pulse is present, also excited state absorption (ESA) terms contribute in both the rephasing and non-rephasing phase matching conditions (Figure 1.5).

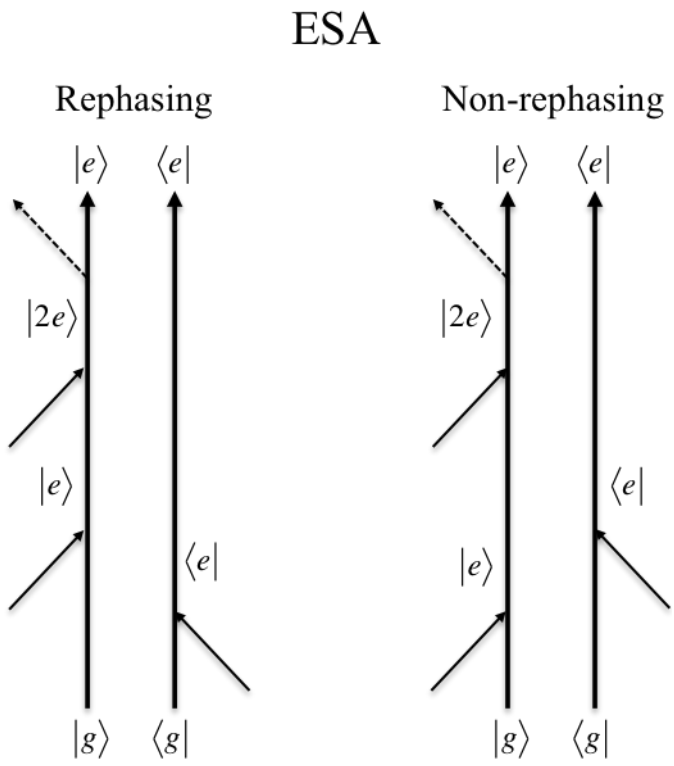

Figure 1.5 Feynman diagrams corresponding to rephasing and non-rephasing ESA paths.

In the ESA process the first two interactions induce the population of an intermediate excited state, and the third laser pulse stimulates a further absorption to the final higher energy state. Consequently, ESA paths give rise to negative signals because of the depletion of the field in the last absorption event [27]. On the other hand, signals deriving from SE and GB pathways are positive.

1.6 Ensemble Averaging and Line-Broadening

As demonstrated in the previous sections, the signal is radiated by the off-diagonal elements of the density matrix, which represent coherences between states simultaneously excited by the laser pulse. If the superposition occurs between two states of an isolated system, it will oscillate continuously between the two states put in coherence and the radiation emitted is a continuous oscillation at the frequency matching their energy gap. However, in spectroscopy we detect a macroscopic polarization induced by the interaction with light perturbation in ensembles made up of a great number of individual systems. Each of them is surrounded by a different environment, which acts with a specific influence on each case. The resulting effect on the ensemble is the average of all that manifested on each individual component. As consequence, the macroscopic oscillation responsible of the radiated signal results from the combination of several components oscillating at different frequencies and with different phases, so that it appears damped.

In this section we will focus on how a fluctuating environment influences the transition frequency of a chromophore and the spectrum lineshape. To better understand this phenomenon, the simplest case of the linear absorption spectrum of a sample is treated in detail, and then the result is extended to higher-order signals.

The linear signal is represented by the free induction decay, which is proportional to the linear polarization induced on the sample. According to the relationship $A(\omega) \propto -2\Re(E^{(1)}(\omega))$ [20], the absorption spectrum is proportional to the electric field emitted by the off-diagonal elements of the density matrix. A general expression of the absorption spectrum can be derived from the commutator of Eqn. 30 [20]. The case in which the radiation is in resonance with the transition from the state *a* to *b* has been considered:

$$A(\omega) \propto Re \int_0^\infty dt\, e^{-i\omega t} \langle \mu(t)\mu(0)\rho(-\infty)\rangle = Re \int_0^\infty dt\, e^{-i\omega t} \langle \mu_{ab}(t)\mu_{ba}(0)\rho_{aa}\rangle \tag{35}$$

It results that the absorption spectrum can be obtained by Fourier Transforming the time evolution of the correlation function of the dipole moment* [20], [21]. Specifically, the longer is the correlation time, the narrower is the relative spectrum.

In the ideal case of an isolated system, the radiation emitted by coherences oscillates indefinitely at the frequency matching the energy gap between the two states *a* and *b*; the corresponding spectrum can be described by a delta function:

$$A(\omega) \propto Re \int_0^\infty dt e^{-i\omega t} e^{i\omega_{ab} t} = 2\pi\delta(\omega_{ab} - \omega) \tag{36}$$

Therefore, in the absence of interactions, the observed resonance frequency is ω_{ab}.

However in real systems we have to deal with ensembles of molecules interacting between them and with the bath, so that each molecule has a different ω_{ab}. Consequently, a distribution of different frequencies transition ω_{ab} subjected to dynamical fluctuations characterizes the macroscopic system. Therefore, the absorption lineshape becomes time dependent and takes the form:

$$A(\omega) \propto Re \int_0^\infty dt\, e^{-i\omega t} e^{i\int_0^t d\tau \omega_{ab}(\tau)} \tag{37}$$

If we separate the frequency $\omega_{ab}(t)$ into its time average $\overline{\omega_{ab}}$ and the time dependent fluctuation part $\delta\omega_{ab}(t)$:

$$\omega_{ab}(t) = \overline{\omega_{ab}} + \delta\omega_{ab}(t) \tag{38}$$

Eqn. 37 can be rewritten as:

$$A(\omega) \propto Re \int_0^\infty dt\, e^{-i\omega t} e^{i\overline{\omega_{ab}} t} e^{i\int_0^t d\tau \delta\omega_{ab}(\tau)} \tag{39}$$

The integral at the exponential is commonly calculated by means of the cummulant expansion, as described in [20]. Some suitable approximation provides the following new expression for the absorption spectrum:

*Time-correlation functions are an effective and intuitive way of representing the dynamics of a system in quantum mechanics. They provide a statistical description of how long a given property of an ensemble at thermal equilibrium persists until it is averaged out by microscopic motions and interactions with surroundings. The time-correlation function of the dipole moment $\langle\mu(t)\mu(0)\rangle$, representing the dynamics of the dipole moment, can be used to describe absorption spectroscopy.

$$A(\omega) \propto Re \int_0^\infty dt\, e^{-i\omega t} e^{i\overline{\omega_{ab}}t}\, e^{-g(t)} \tag{40}$$

with $g(t)$ the so-called lineshape function:

$$g(t) = \int_0^t \int_0^{\tau'} d\tau' d\tau''\ \langle \delta\omega(\tau'')\delta\omega(0)\rangle \tag{41}$$

where $\langle \delta\omega(t)\delta\omega(0)\rangle$ is the frequency correlation function [21], which describes all linear spectroscopy in the limits of the cummulant expansion [20].

The correlation function will decay very quickly when the transitions frequency fluctuations are very fast, whereas it will decay slowly in time in the opposite case. It is often modelled by an exponential function:

$$\langle \delta\omega(t)\delta\omega(0)\rangle = \Delta^2 e^{-\frac{t}{\tau_C}} \tag{42}$$

where Δ is the fluctuation amplitude, i.e. the amplitude of the deviation $\delta\omega$ from ω_{ab}, and τ_C the correlation time. In this way we can derive the so-called Kubo-lineshape function [28],[29]:

$$g(t) = \Delta^2 \tau_C^2 \left[e^{-\frac{t}{\tau_C}} + \frac{t}{\tau_C} - 1 \right] \tag{43}$$

This model is very important since it can describe all the possible broadening phenomena, which can be substantially separated into dynamic processes intrinsic to the individual system known as homogeneous broadening, and static disorder which derives from an ensemble averaging effect, classified as inhomogeneous broadening [21].

This model is thus suitable to discuss the following limiting cases:

Long correlation times: it corresponds to the inhomogeneous limit when the lineshape reflects a static distribution of resonance frequencies of the molecules of the ensemble, but they do not fluctuate. It arises from the different structural environments available to the system molecules. In this limit:

$$g(t) = \frac{\Delta^2 t^2}{2} \tag{44}$$

and the absorption lineshape is:

$$A(\omega) \propto Re \int_0^\infty dt e^{-i\omega t} e^{i\overline{\omega_{ab}}t} e^{\frac{\Delta^2 t^2}{2}} = \sqrt{\frac{2\pi}{\Delta^2}} \exp\left(-\frac{(\omega - \overline{\omega_{ab}})^2}{2\Delta^2}\right) \tag{45}$$

that corresponds to Gaussian function centred at $\overline{\omega_{ab}}$ with width Δ described by the frequency distribution.

Short correlation times: it corresponds to the rapid fluctuations of each molecule in phase and in frequency in the whole range Δ. These are dynamical and intrinsically molecular processes that can contribute to damping and line-broadening. It is the case of the homogeneous limit, in which we obtain:

$$g(t) = \Delta^2 \tau_C t = \frac{t}{T_2} = \Gamma t \tag{46}$$

where $\Delta^2 \tau_C = \frac{1}{T_2} = \Gamma$ represents the decay constant responsible of damping the oscillation between the states *a* and *b*. For the absorption lineshape:

$$A(\omega) \propto Re \int_0^\infty dt e^{-i\omega t} e^{i\overline{\omega_{ab}}t} e^{-\Gamma t} = \frac{2\Gamma}{(\omega - \overline{\omega_{ab}}) + \Gamma^2} \tag{47}$$

that is a Lorentzian shape function centred at $\overline{\omega_{ab}}$. The decay constant Γ includes the contribution of decay of the excited state $1/2T_1$, and the pure dephasing $1/T_2^*$. The first term accounts for the loss of population in the excited state, while the last is due to the distribution and randomization of ω_{ab}.

Homogeneous and inhomogeneous broadening are limiting cases of the frequency fluctuation correlation function and correspond to a strict separation of timescales, the first being infinitely fast and the second infinitely slow [20]. An additional case is that of the so called spectral diffusion process. In this regime, given a distribution of configurations that the system can adopt, for example in the case of a chromophore in a liquid, any molecule of the system at equilibrium and over a long enough time will sample all the available configurations [21]. In this case the absorption lineshape results in a Voigt profile, i.e. a Lorentzian lineshape convoluted with a Gaussian distribution.

This treatment can be extended to higher order signals and the lineshape function $g(t)$ can be used to calculate the corresponding polarizations. We report as example the response function corresponding to R_2 Feynman path that contributes to the total third order response function:

$$R_2(t_1,t_2,t_3) = \langle \mu(t_1+t_2+t_3)\mu(t_1)\rho(-\infty)\mu(0)\mu(t_1+t_2)\rangle = \tag{48}$$
$$-\left(\frac{i}{\hbar}\right)^3 \mu^4 e^{-i\omega(t_3-t_1)} e^{-g(t_1)+g(t_2)-g(t_3)-g(t_1+t_2)-g(t_2+t_3)+g(t_1+t_2+t_3)}$$

In addition to the Kubo's lineshape model, which is a classical theory, there are different ways to describe $g(t)$, for example the fully quantum mechanical Brownian oscillator model. While the Kubo model does not specify the type of coupling with the solvent responsible of the fluctuating transition frequency, the Brownian oscillator exactly specifies the coupling. It indeed substitutes the phenomenological amplitude of the fluctuations Δ with a more meaningful displacement on the nuclear potential surface due to temperature.

1.7 Vibronic coupling in the lineshape function

The description of the spectral line shape $g(t)$ must also include the vibronic coupling between electronic and vibrational states, which modulates the electronic transition.

We know that the complete wavefunction of a molecule must describe both nuclei and electrons, which are reciprocally interacting. For this reason, the Schrödinger equation cannot be resolved exactly, and the introduction of the so-called adiabatic approximation becomes necessary.

In quantum mechanics, the adiabatic approximation refers to a time-scale separation between fast and slow degrees of freedom, to make use of approximate solutions to the Schrödinger equation as product of the states in the fast and slow degrees of freedom. In other terms, this approach is based on the reasonable assumption that electrons move much faster than nuclei owing to their large mass difference, so that they adapt rapidly in response to shifting nuclear positions [21], [26].

The general scheme of the adiabatic approach, common to its three versions known as crude adiabatic (CA), Born-Oppenheimer (BO) and Born-Huang (BH) approximation [18], describes the total wavefunction as product between the electronic and vibrational wavefunctions, thus the total energy as the sum of the electronic and vibrational ones:

$$\Psi = \psi_{el}(r,R)\chi_{vibr}(R) \qquad \mathrm{E} = E_{el} + E_{vib} \tag{49}$$

where *r* and *R* denote the electronic and nuclear coordinates, respectively. In this description, the electronic function depends on both electronic and nuclear coordinates, while the nuclear wavefunction only accounts for the nuclear ones. According to the main assumption of adiabatic approximation, this means that electrons do not have any influence on the nuclear motion, except for the fact that they provide the potential surface on which the nuclear motion occurs freely.

Our interest is to understand how the vibrational functions coupled to the electronic transition play a role in the determination of the spectral lineshape function $g(t)$. For this purpose, we consider the transition from a particular vibronic level of the ground electronic state $\Psi_{g,a}(r,R) = \psi_g(r,R)\chi_a(R)$ to a vibronic level of an excited state $\Psi_{e,b}(r,R) = \psi_e(r,R)\chi_b(R)$. The transition dipole moment, calculated as expectation value of the dipole moment operator acting on the two vibronic wavefunctions, can be expressed as follows:

$$\mu_{ge,ab}(Q) = \langle \Psi_{g,a}(r,R) | \tilde{\mu}(r) | \Psi_{e,b}(r,R) \rangle \tag{50}$$

A convenient way to solve this expression is to expand the transition dipole moment around the equilibrium nuclear coordinate R_0

$$\mu_{ge,ab} = \langle \Psi_{g,a}(r,R_0) | \tilde{\mu}(r) | \Psi_{e,b}(r,R_0) \rangle \langle \chi_a(R) | \chi_b(R) \rangle + \\ + \left(\frac{\delta \mu(R)}{\delta R} \right)_0 \langle \chi_a(R) | R | \chi_b(R) \rangle + \ \ldots \tag{51}$$

Within the so-called Franck-Condon approximation, which assumes that there is no dependence for the dipole operator on the nuclear coordinate *R* [20], we can truncate the expansion at the first term. This approximation implies that transitions between electronic surfaces occur without a change in nuclear coordinate (vertical transitions). It results that that the overall transition dipole $\mu_{ge,ab}$, which is related to the intensity of the transition between the two vibronic states, is proportional to the *nuclear overlap integral* $\langle \chi_a(R) | \chi_b(R) \rangle$ known as Condon factor [26]. In other terms, transition intensities are correlated to the vertical overlap between vibrational wavefunctions in the two electronic surfaces [21]. A reasonable assumption is that the vibrational structure does not change from the ground to the excited state, thus also the shapes of the vibrational functions in the two electronic states are the same. Therefore, the Condon factor only depends on the displacement along the nuclear coordinates between the ground and the excited states.

Panel a of Figure 1.6, adapted from [21], shows a model for vibronic transitions described by harmonic potentials representing the ground and the excited state, with a vibrational mode at frequency ν coupled with them. According to the Franck-Condon principle, transitions occur vertically and the shift between the minimal of the two potential curves is denoted with D. It represents a measure of the strength of coupling of the electronic states to the nuclear degree of freedom, and is connected with Huang-Rhys parameter [21].

Now, let's investigate how the absorption lineshape depends on *D*. Under typical conditions, at equilibrium the system is on the ground electronic state. In this case the spectral lineshape $g(t)$ takes the form [21]:

$$g(t) = -D\left(e^{-i\nu t} - 1\right) \tag{52}$$

If $D = 0$ there is no dependence of the electronic energy gap ω on the nuclear coordinate and only one resonance, corresponding to the nuclear overlap $\langle 0_g(Q)|0_e(g)\rangle$, is observed. Panel b Figure 1.6 illustrates the time dependence of $g(t)$, which oscillates with the frequency ν of the single vibrational mode, modulating in time the correlation function of the dipole moment, reported in panel c. This induces the appearance of an additional peak at frequency ω+ν in the absorption spectrum obtained from the Fourier Transform of the dipole correlation function [21], and shown in panel d.

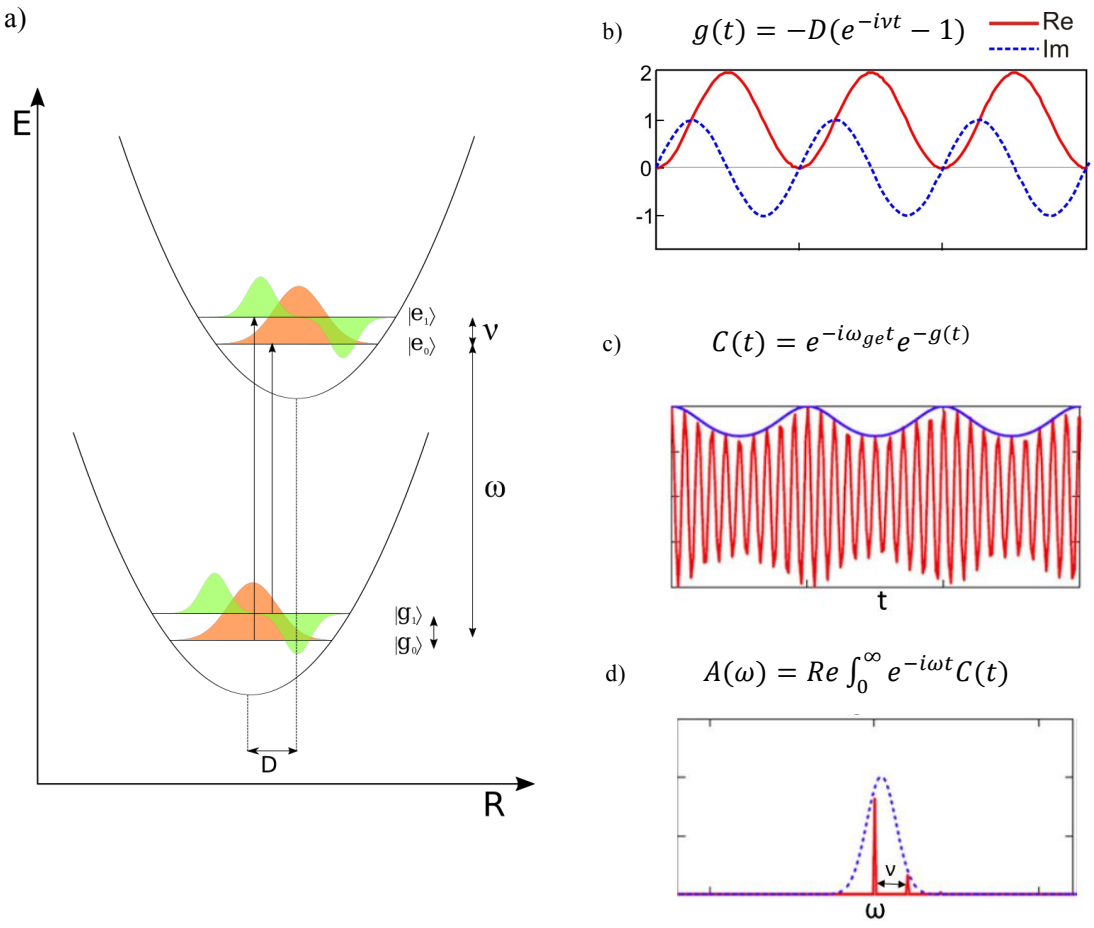

Figure 1.6 (a) Vibrational levels lying in the ground and excited electronic potential curves. The displacement D between the minimal of the two potential curves drives the transition toward the excited state into a different vibronic state. (b) The time dependence of the spectral lineshape *g(t)*. (c) The time dependence of the correlation function of the dipole moment *C(t)*. (d) Absorption spectrum *A(ω)* obtained from the FT of *C(t)*. The modulation of *C(t)* induced by *g(t)* generates a new peak at frequency ω+ν. Panels b, c and d are adapted from Tokmakoff's lessons slides.

Despite the complexity of the treatment, it is important to outline that the vibronic coupling quantified by the Huang-Rhys parameter D has a relevant role in the time modulation of the electronic transition, trough its contribution to the description of the spectral lineshape $g(t)$.

This result, obtained in the simple case of the linear response, can also be extended to the higher-orders response functions and can be applied to describe the time-resolved spectra treated in this thesis.

1.8 Third-order polarization

The third-order polarization is related to four-wave mixing processes, which involve the interaction of 3 laser fields with wave vectors k_1, k_2 and k_3, and frequencies ω_1, ω_2 and ω_3 respectively, with the material system [25], [30]. They play an important role in the current studies of nonlinear optical phenomena and include third harmonic generation, transient grating, photon echo and coherent anti-Stokes Raman (CARS). In this application the signal field is generated in a new direction k_s, different from any of the incoming waves.

According to the general expression in Eqn. 29, the third order polarization takes the form:

$$P^{(3)}(t) = \int_0^\infty dt_3 \int_0^\infty dt_2 \int_0^\infty dt_1 E(t-t_3)E(t-t_3-t_2) \\ E(t-t_3-t_2-t_1)S(t_3,t_2,t_1) \tag{53}$$

and, if we write explicitly the field, the number of terms contributing to the polarization in Eqn. 53 is very large. However, as stated in section 1.5, under suitable experimental conditions it is possible to restrict the number of terms contributing to the third-order signal. In these conditions, the third-order response function can be written as the sum of four terms and their complex conjugates in the following way:

$$S^{(3)}(t_3,t_2,t_1) = \left(-\frac{i}{\hbar}\right)^3 \sum_{n=1}^{4} [R_n(t_3,t_2,t_1) - R_n^*(t_3,t_2,t_1)] \tag{54}$$

where R_n are the Feynman paths corresponding to the Feynman diagrams reported in Figure 1.4.

The third order polarization is the most informative for the study of the excited state dynamics. It can be understood considering from a pictorial point of view how the Feynman paths develop under the sequence of laser pulses interacting with the sample. With this aim, we take the example of a three level system composed by the ground state *g* and two excited states *e* and *f*. It is reasonable to assume that at equilibrium conditions only *g* is populated. It is also assumed that the laser spectrum is broad enough to simultaneously excite both the excited states. As example, only the time evolution of R_2 Feynman path is followed.

Panel a of Figure 1.7 shows schematically what happens when the first laser pulse reaches the sample. The interaction with k_1 creates a coherence between the ground and each of the

excited states, which in the density matrix representation corresponds to the generation of the corresponding off-diagonal element $|g\rangle\langle e|$ and $|g\rangle\langle f|$. Note that in R_2 the interaction occurs on the right side of the diagram because of the particular phase matching condition of this diagram. During the first time interval t_1 between the first and the second pulse the two coherences start to dephase through the interaction with environment, but they have not to dephase completely before the second pulse reaches the sample.

In the R_2 path shown in panel b of Figure 1.7 the second pulse interacts with the left side of the diagrams promoting the ket from *g* to *f* or to *e*. Here for simplicity only the former case is analysed. This gives rise in the first case to a coherence between the two excited states, $|f\rangle\langle e|$, which oscillates during the time interval t_2 at the frequency corresponding to the energy gap between the *e* and *f* states, until it dephases completely. While this coherence represents an oscillatory contribution to the total signal, the pure state $|f\rangle\langle f|$ generated in the second case freely evolves along t_2.

The third pulse reaching the sample after a time interval t_2, generates coherences between *g* and each of the excited states *e* and *f* again, and sends the bra of the R_2 path to the ground state, as shown in panel c of Figure 1.6. Now, the generated coherences dephase during the time interval t_3 emitting the third order signal in the direction $k_s = -k_1 + k_2 + k_3$, which is the phase matching condition to obtain the rephasing signal. In the same direction also the R_3 and ESA paths contribute to the signal, as stated in Section 1.5.

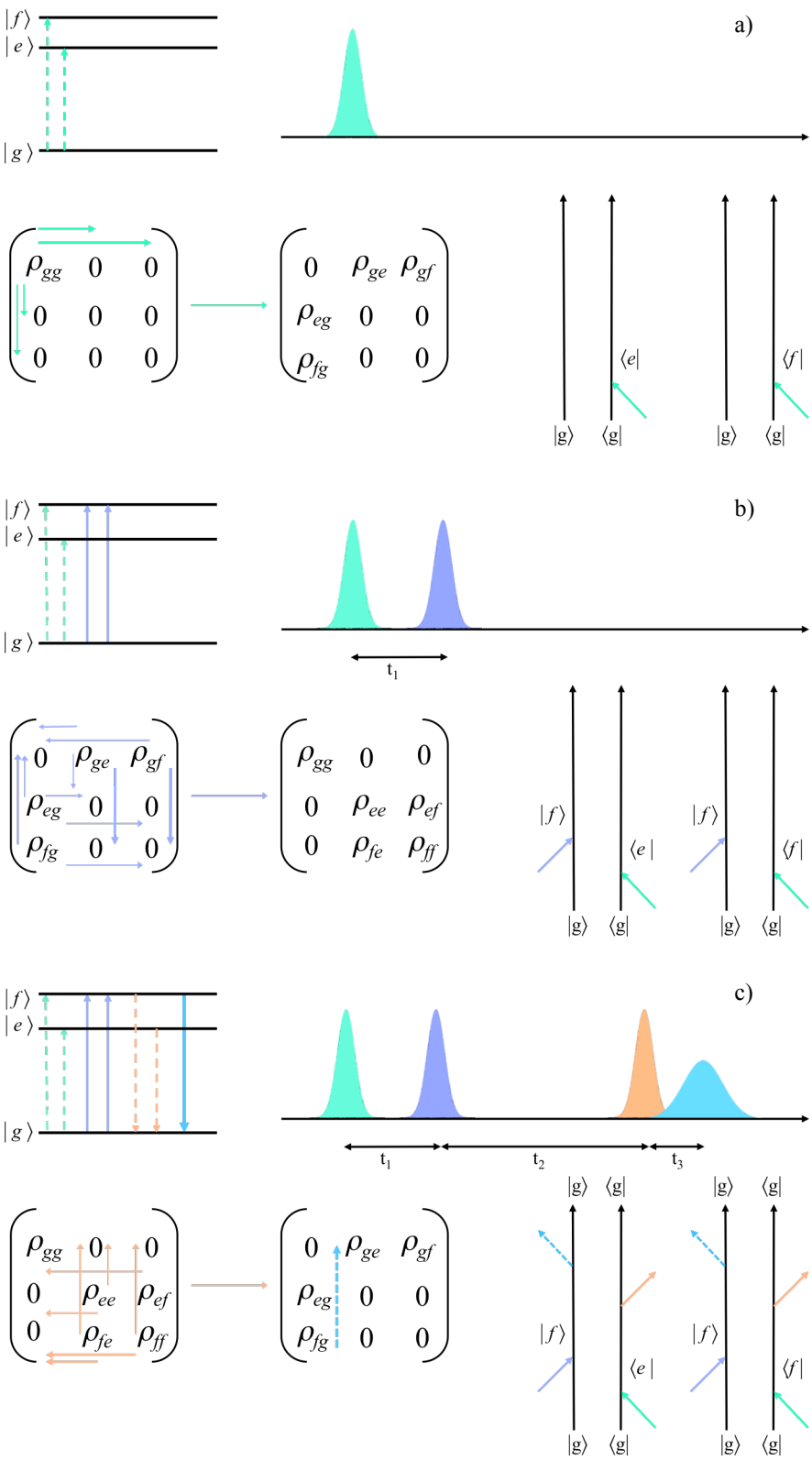

Figure 1.7 Time evolution of a three-level system under the perturbation of three laser pulses inducing a third-order polarization following R_2 Feynman path. The upper left panel shows the interaction with pulses in the energy levels picture, where solid and dashes lines correspond to interactions with ket and bra, respectively. The upper right panel shows the time-ordering of the pulses. The lower panels illustrate in the density matrix picture (left) and in the diagrammatic formalism (right) the variations in the density matrix induced by the perturbation. The interaction with the first, the second and the third laser pulses are illustrated in (a), (b) and (c), respectively.

1.9 2D Photon Echo

1.9.1 Phase matching and pulse sequence

2D Photon Echo spectroscopy (2DPE) is a third-order nonlinear technique, belonging to the class of four-wave mixing spectroscopies. Three femtosecond laser pulses interact with the sample and cause the stimulation of the third-order coherence response, and a fourth pulse called local oscillator (LO) is used for detection purposes (see below). The four pulses are arranged at the vertices of a square in a BOXCARS geometry, until they are focalized on the sample.

The approach outlined in the previous section describing the example of some of the R_2 excitation pathways, can be generalized to the other terms of the third order response in the following way. During the time period between the first two pulses, the response evolves as a coherence between the ground and resonant excited states, defined as a one-quantum coherence. The initial time delay t_1 is therefore often referred to as the *coherence time* τ. The second interaction promotes the evolution of populations of the ground or excited states, or coherences between excited states, defined as zero-quantum coherences. The time delay between the second and the third pulse is referred to as the *population* or *waiting time* T. Depending on the system under investigation, vibrational states or vibrational coherences can also be excited, which evolve during T. The third pulse stimulates the system to relax creating a second coherence that dephases during the time delay t_3 and emits the third-order signal. The delay between the third pulse and the emitting signal is referred to as the *rephasing* or *echo time* t. The signal is emitted in the same direction of LO and the measured quantity is indeed their interference, according to the so-called heterodyne detection, which is discussed in detail in the following section. In 2DPE a photon echo will be recorded only when the phase acquired during τ is reversed during t, which is the case of the rephasing paths where during the first period τ the density matrix evolves in a coherence ρ_{ij}, which is the flipped to a ρ_{ji} coherence in the last period t. On the contrary, non-rephasing experiment ($\tau<0$, E_2 coming before E_1) does not generate any echo, but provides complementary information with respect to the properly time ordered pathways ($\tau>0$, E_1 coming before E_2) giving rise to the photon echo signal. From now on, we will use τ, T and t to indicate the three time delays in 2DPE.

The pulse sequence and the BOXCARS geometry adopted in the 2D measurements presented in this thesis are shown in Figure 1.8.

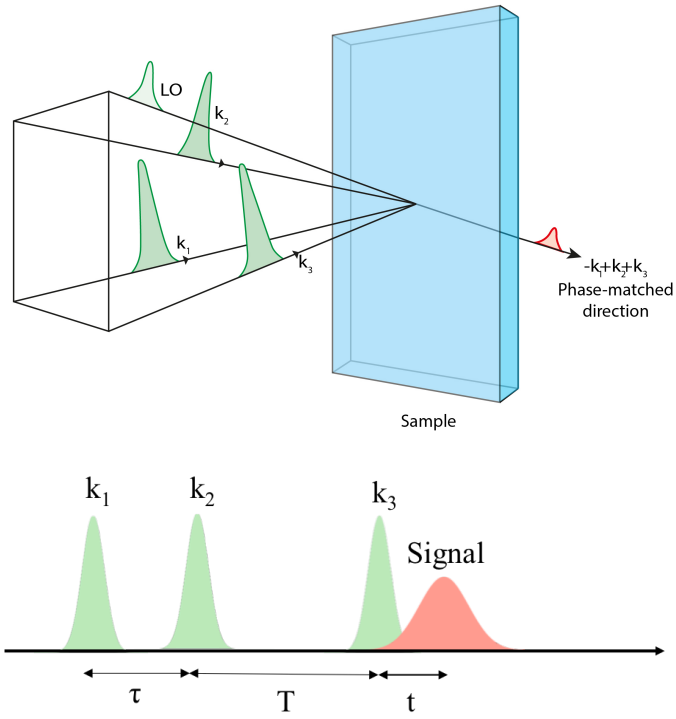

Figure 1.8 Sequence of laser pulses and time delays. Boxcars geometry of pulses: $k_s = -k_1 + k_2 + k_3$ when τ >0 (rephasing) or $k_s = +k_1 - k_2 + k_3$, when τ <0 (non-rephasing).

This geometry allows easily performing both rephasing and non-rephasing experiments simply exchanging the time ordering of the pulses. In this thesis we will focus on the rephasing experiment that is the source of primary information about vibronic coupling and relaxation dynamics.

1.9.2 Heterodyne detection

An important advantage of wave-mixing techniques is that the signal can be generated in a new direction, different from the incoming fields. This allows to drastically reducing the background with respect to other spectroscopies, such as pump-probe, for example. Despite this advantage, typically non-linear polarization and the related signal are weak. Therefore, the homodyne detection of the signal directly in terms of its intensity $I_S(t) \propto \left|\vec{E}_S(t)\right|^2$ is not convenient, since the square of a small quantity is very small. An improved sensitivity and signal to noise ratio is achieved by means of a different detection scheme, known as heterodyne detection [25]. In this scheme the LO field, having the same wavevector as the radiated signal field, is introduced to interfere with it. In this way, the interference between the LO pulse and the signal is acquired, giving rise to a linear instead of quadratic dependence of the recorded intensity on the weak signal field. The total detected intensity is then:

$$I_{tot} = \frac{n(\omega_S)c}{4\pi}|E_{LO}(t) + E_S(t)|^2 = I_{LO}(t) + I_S(t) + 2\frac{n(\omega_S)c}{4\pi}Re[E_{LO}^*(t) \cdot E_S(t)] \quad (55)$$

where I_{LO} is the intensity of the local oscillator field and I_S the homodyne contribution which is usually negligible compared to the third term. The contribution of the local oscillator alone can be measured independently and easily subtracted from the total recorded intensity, giving rise to the heterodyne signal:

$$I_{HET}(t) = \frac{n(\omega_S)c}{4\pi} Re[E_{LO}^*(t) \cdot E_S(t)] \quad (56)$$

The resulting heterodyne signal is linear rather than quadratic in the weak nonlinear polarization, therefore it is much stronger and easier to detect.

Another advantage of the heterodyne detection is that, since the polarization is a complex quantity, it allows separating the imaginary and real components, corresponding to the refractive and absorptive parts respectively. This is possible by controlling the relative phase of E_{LO} and $P_S(t)$, which makes the heterodyne detection a *phase-sensitive* method [25], [31], [32]. Experimentally, there are different methods to separate the two contributions, which are referred as 'phasing' procedures [33]. However, the phasing procedure is not easily applicable and in certain cases can lead to artifacts. Therefore, the analysis can be restricted to the absolute part of the signal, which is phase independent. For this reason, in this thesis we will focalize on absolute spectra.

1.9.3 2D Signal: Physical meaning

Since it is difficult to visualize the total signal as function of the three time delays, Fourier Transforms along both the τ and t directions are performed, to obtain:

$$S(\tau, T, t) \rightarrow S(\omega_\tau, T, \omega_t) \quad (57)$$

The resulting signal is easier to interpret since it expresses the intensity of the coherences between ground and excited states in terms of frequency. It is also possible to build 2D maps at different values of T where x and y axes correspond to ω_τ and ω_t respectively, and to merge them along the z-direction (T) to form a 3D matrix. From another point of view, the x coordinate can be interpreted as the frequency at which the excitation of the system occurs, and the y axis as the emission frequency. This is particular meaningful since the signals and the relative intensities of the states involved in the relaxation dynamics of the system following excitation, can be easily detected as features of the 2D maps appearing at different coordinates. Specifically, a diagonal peak means that the emission occurs from the same state that has been excited by the laser pulse. Diagonal peaks thus represent populations, i.e.

pure states, whose evolution along the population time provides information about the decay dynamics of the corresponding states. More significant are the off-diagonal peaks of the 2D maps, which represent coherent superpositions of states we are interested to. Independently of the nature of the states involved, a cross peak means that excitation and emission occur from different states. Therefore, it is possible to study the dynamics of transfer processes, such as energy transfer between electronic states or ultrafast relaxation following excitation, characterizing the oscillatory behaviour of coherences along the population time.

In order to assess the nature of the different signals appearing in the 2D maps, it is very useful to identify the main Feynman paths contributing at the signal on different positions.

To better understand how the Feynman paths are correlated to the signals in the 2D maps, let us start from the simplest case of the two level system described by ground and excited states *g* and *e*. Then the description will be generalized to the more informative three level system introduced in the previous section.

As explained in Section 1.5, the third order response of a two level system can be described trough R_3 and R_1 paths corresponding to the rephasing and non rephasing terms respectively for GSB process, and trough the SE paths, R_2 and R_4 for the rephasing and non-rephasing signal. The GSB and SE contributions only differ in the pure state evolving during T, the ground state and the excited state, respectively. If we focus only on the rephasing diagrams, we can see that both R_2 and R_3 are characterized by the evolution of the conjugated coherences $|g\rangle\langle e|$ or $|e\rangle\langle g|$ in the time delays τ and t. This means that the signals arising from these GSB and SE diagrams contribute at the same diagonal position, corresponding to the frequency matching the energy gap between the ground and the excited state. The evolution of the signal along the population time provides in this case information about the relaxation dynamics of ground and excited state populations.

More interesting and a bit more complex is the interpretation of the features characterizing the 2D map in the case of the three level system in Figure 1.7. An example of rephasing map for this system is shown in Figure 1.9. In addition to the complexity due to the large number of contributions to the third order response, the effects of homogeneous and inhomogeneous broadening on the shape of the signals are included. Note that no assumption has been made about the nature of the excited states, meaning that they could represent different electronic states or vibrational sub-levels within the same electronic state. The position of each signal in the map is again related to the frequency associated with the evolution of the system during the coherence and the rephasing times. Two diagonal signals relative to GSB and SE diagrams account for the populations of the pure states $|f\rangle\langle f|$ and $|e\rangle\langle e|$. In addition, the cross peaks due to the SE pathways, indicate coherences between the states *e* and *f*. As

explained in the Section 1.8, the evolution of the pure states $|f\rangle\langle f|$ and $|e\rangle\langle e|$ along T represents the decay dynamics of the corresponding states. On the other hand, the cross peaks due to the Feynman paths where the coherences $|f\rangle\langle e|$ or $|e\rangle\langle f|$evolve during T, oscillate at the frequency matching the energy gap between the two states, until the coherences survive.

The presence of more than two levels induces to consider also the possibility of ESA processes, highlighted by negative signals usually away from the diagonal.

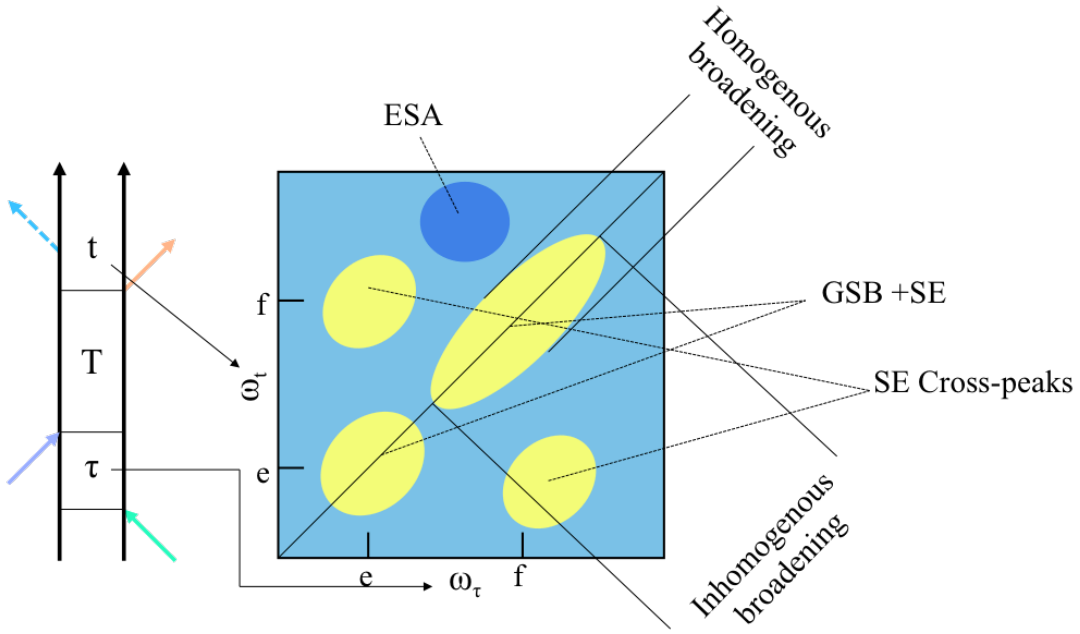

Figure 1.9 Typical 2D map relative to a three level system with ground state g and excited states e and f.

One of the main advantages of 2D electronic spectroscopy is the possibility to easily reveal the coherent superposition of states and their dynamics, since they appear at off-diagonal positions, far from the congested diagonal region where the populations relaxation takes place. A detailed explanation about how it is possible to identify coherences between states of different nature is reported in the next section.

1.9.4 Vibrational and electronic coherences

The possibility of experimentally detecting coherences is linked to the ability to excite the system with ultrashort laser pulses. Referring to the eigenstates description, a short pulse is indeed able to prepare a superposition of eigenstates excited in phase. On the other hand, if the pulse is not short enough, many systems with different phases are excited, and the relative beating disappears upon averaging [1]. 2DPE spectroscopy takes advantage of femtosecond laser pulses that have spectral bandwidth in the order of thousands of cm^{-1}, thus, together with several vibrational transitions, also different electronic transition can be

excited simultaneously. Particularly, organic chromophores studied in this thesis, have vibrational transitions with frequencies in the range between 400-3000 cm^{-1}; this means that all the vibrational states coupled to the electronic transition can be coherently excited by the first two laser pulses [26].

In general, both vibrational and electronic coherences may contribute to the appearance of beating in the spectroscopic signal, since ultrafast pulses may excite superposition of electronic as well as vibrational states. The result is a very complex oscillating pattern along T, and particular care must be taken in the attribution of the beating signals.

The assessment of the nature of the states involved in the coherent dynamics is a still an open challenge. A lot of possible protocols are being debated in the literature, about the possibility to distinguish between vibrational and electronic coherences [1], [34]–[36].

Such protocols are mainly based on the analysis and comparison of the beating behaviour at different positions in the 2D maps in the rephasing and non-rephasing portion of the signal. The preliminary analysis of the Feynman paths contributing to the signals and the knowledge of the states of the system accessible by the exciting laser bandwidth is a very important support in the identification of signals.

Here, we treat two simplified models describing two common situations: a) the case of one vibration coupled with both ground and excited states in a two level system; b) the case of the coherence between two electronic states in a homodimer described by two excitonic states α and β.

Particularly useful in this type of analyses are the so-called Fourier or frequency maps, i.e. 2D maps as function of the excitation ω_τ and emission frequency ω_t as the ones previously described, but calculated at fixed relevant values of the Fourier analogue of the population time, ω_T. The advantage is that they provide a direct visualization of the positions in the 2D map where a specific beating frequency contributes more, giving rise to typical patterns which characterize the two types of coherences we are more interested to (electronic and vibrational). A detailed explanation on how Fourier maps can be generated is reported in Chapter 3.

The ideal pattern that one would expect for the pure vibrational coherences characterizing the model system a) is illustrated based on the description of Turner et al. [34] in Figure 1.10.

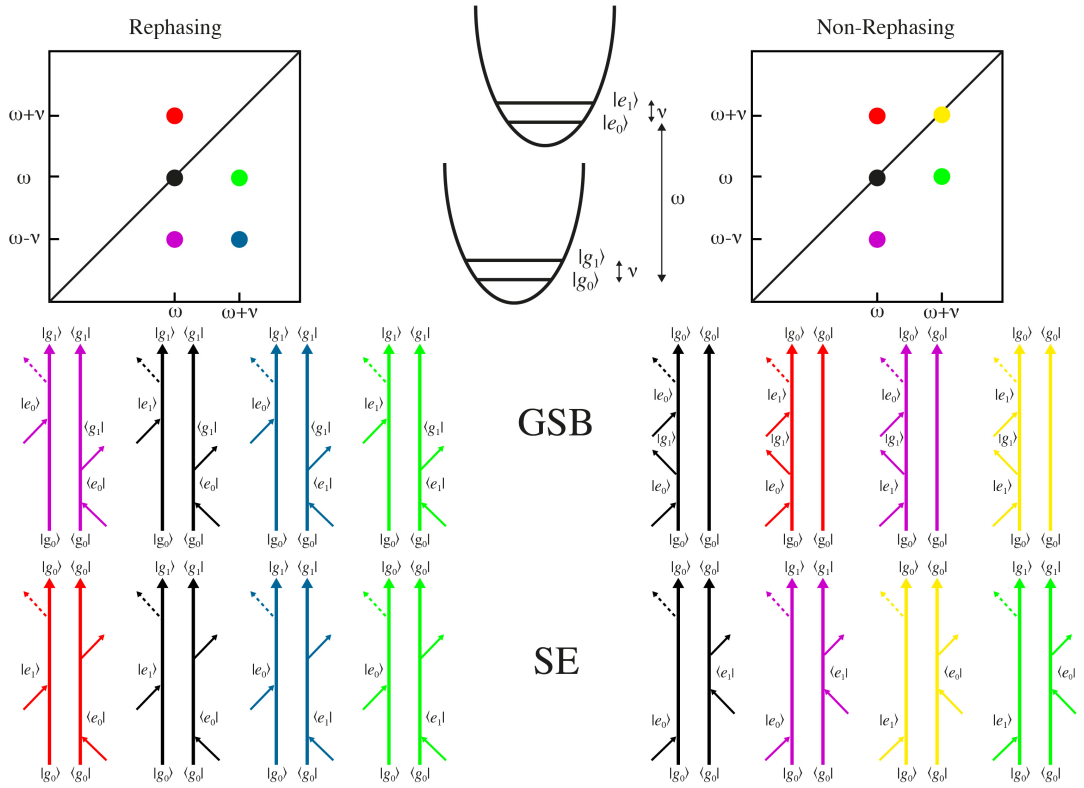

Figure 1.10 Typical patterns generated by vibrational coherences in the rephasing and non-rephasing maps corresponding to the GSB and SE paths. In the simplified model system considered, only a vibration is coupled with both the ground and the excited state.

Only Feynman diagrams contributing to the beating signal along T are considered and shown. The ESA contributions are neglected since they become relevant in the presence of higher energy states. The different diagrams are classified on the base of the corresponding GSB and SE paths, and are labelled with colours in agreement with the position in the Fourier map to which they contribute. In the rephasing map beating signals related to vibrational coherences occupy positions having a 'chair-like' symmetry. Note that it differs for only one point from the non-rephasing map: here an oscillation at coordinates (ω+ν ; ω+ν), totally absent in the previous case, substitutes the beats at (ω+ν ; ω-ν), typically detected in the rephasing signal. It must be considered that the model illustrated here is very simplified compared to the realistic case where more than one vibrational mode is coupled with the electronic transition. In this case, we would expect that the different components oscillate with frequency ν_x at coordinates $\omega \pm \nu_x$.

The typical patterns due to coherences involving two pure electronic states for the rephasing and non-rephasing maps are shown in Figure 1.11. Firstly we can note a great difference from the behaviour manifested by vibrational coherences. In the case of the homodimer, only diagonally symmetric cross peaks oscillating with frequency $\omega_\beta - \omega_\alpha$ characterize the rephasing map. In the non-rephasing map, instead, electronic coherences oscillate on

diagonal positions. This is a very useful feature in the recognition of vibrational and electronic coherences. The patterns shown in Figure 1.11 for the homodimer model also characterize coherences between any pair of electronic states simultaneously excited by laser.

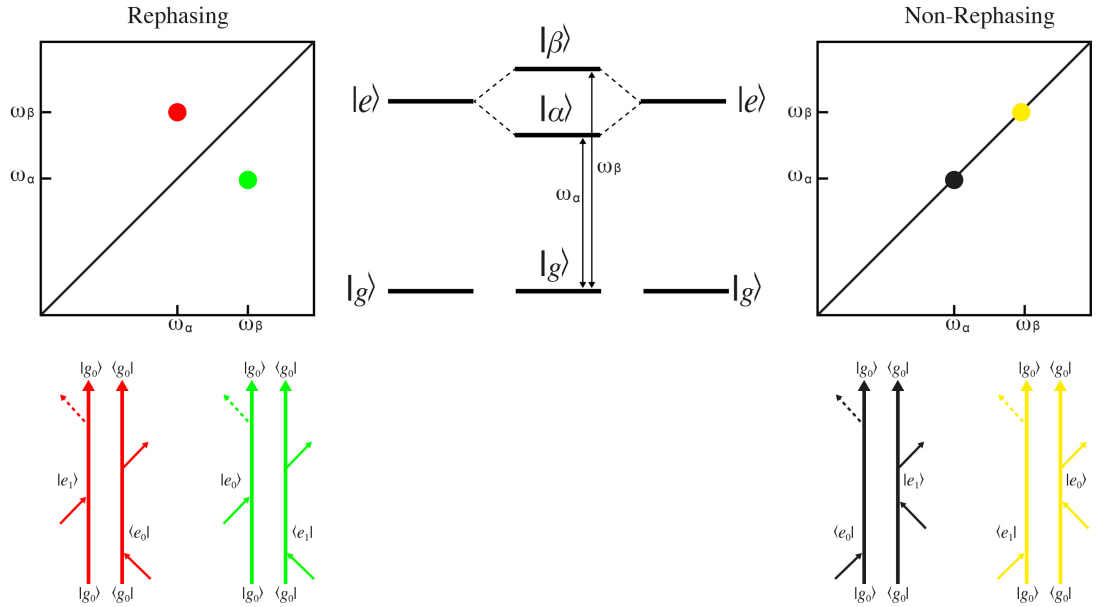

Figure 1.11 Typical patterns due to electronic coherences for the rephasing and non-rephasing maps corresponding to the SE Feynman paths. The model considered is a homodimer system.

Another property that distinguishes vibrational from electronic coherences is their different dynamics: the first survive for longer times in the order of picoseconds, whereas electronic coherences are typically damped in about tens of fs. This is because vibrational wavefunctions and their energies are less influenced by environment fluctuations than electronic ones.

Among the two limit cases of pure electronic and pure vibrational coherences, the possible presence of vibrations in close resonance with energy gaps between electronic states may give rise to intermediate situations. The possible coupling between vibrational and electronic transitions is arising increasing interest since it has been theoretically proposed that it may be responsible of extraordinary long-lived coherences experimentally detected [1], [37], [7]. For this reason, a thorough investigation of how vibrations interact with electronic degrees of freedom in organic molecules and how this is manifested in 2D spectra is absolutely timely and necessary.

Chapter 2

The system: characterization of linear and vibrational properties

2.1 BODIPY dyes: a new *El Dorado* for spectroscopic studies

Among the large variety of fluorescent molecules the BODIPY† [38] family has gained recognition as being one of the most versatile and has been the focus of considerable research interest over the last three decades for many different applications across a wide scientific community [39]–[42]. The first member was introduced by Treibs et al. in 1968 [43], but a little attention was given to the discovery until the end of the 1980 [44]–[46]. Then, with the recognition of their high potential as biological labelling as well as tunable laser dye, BODIPYs have spectacularly risen in popularity as indicated by the growth of the number of papers and patents on these dyes [40], [47]–[49]. In the years, they became an improved photostable substitute for fluorescein with also narrower spectral bandwidths, insensitivity to pH and higher solubility in non-polar solvents [39], [47]. These properties, together with the high fluorescence quantum yield, intense absorption profile, negligible triplet-state formation, resistance towards self-aggregation, structural versatility and reasonable stability to physiological conditions, all contribute to the general attractiveness of these compounds [39]–[42], [49]–[51].

Their large number of applications, in addition the ones already outlined, includes chemosensors, fluorescent switches, labels in fluorescence imaging, drug delivery agents, electroluminescent films, light-harvesters, sensitizers for solar cells, energy transfer cassettes and so on [52]–[61].

† 4,4-difluoro-4-bora-3*a*,4*a*,-diaza-*s*-indacene better known as BODIPY, difluoroboron-dipyrromethene (or BDP).

2.1.1 BODIPY dyes: structural and photophysical properties

The basic structure of BODIPY, referred as the core of the chromophore, depicted in Figure 2.1 consists of two pyrrole rings linked by methene and BF_2 groups, with the boron atom coordinated to the heteroatoms [62], [59]. As the name of the dye class suggests, the type of structure is commonly described as being boradiazaindacene in analogy with all-carbon tricyclic rings, and the numbering of any substituent reported in Figure 2.1 follows rules set up for the carbon polycycles [39], [63].

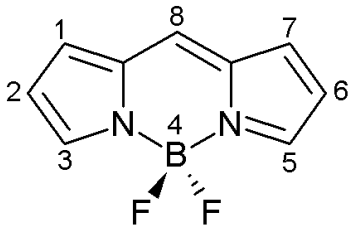

Figure 2.1 Structure of the BODIPY core.

In analogy with porphyrinic systems, the 8-position is often referred to as being the *meso* site. The greatly restricted flexibility of the BODIPY structure leads to unusually high fluorescence quantum yields and to consider these compounds as an example of 'rigidified' mono-methine cyanine dye [63], [39], [64].

The coordination of the boron atom holds the frame of carbon atoms of the dipyrromethene ligand in a rigidly planar conformation, thus BODIPY properties are broadly similar to those of aromatic systems although these dyes do not formally fit the Hückel's rule for aromaticity [40], [39]. The BF_2 group does not take part in the delocalized π-system but only acts as a linking bridge. Theoretical calculations and X-ray diffraction data have confirmed the planar structure recognizing the C_{2v} point symmetry group for the optimized geometry of the BODIPY core in the ground state [64].

BODIPY dyes are neutral molecules, but with a zwitterionic structure in which it should be expected a net negative charge on the B atom because of its tetra-coordination, while a positive charge is delocalized through the electronic π-system. The resonant structures, and their symmetrical counterparts, reported in Figure 2.2 illustrate the charge distribution of the BODIPY core [64]–[68].

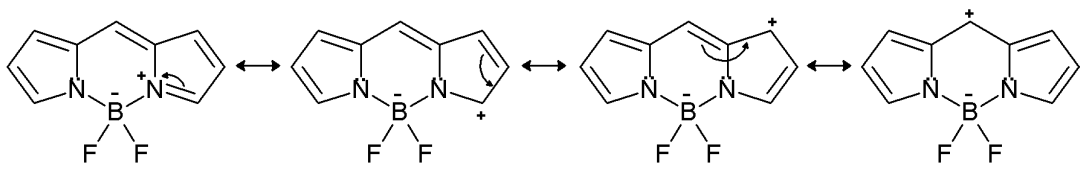

Figure 2.2 Resonance structures of BODIPY core.

Two extreme resonance structures can be identified: the structure ‘a’ with a lower distance charge separation, since the positive charge is on the N atom, close to the B atom with the negative charge, and the structure ‘d’ where the positive charge at the C atom in the 8-position provides a higher distance charge separation along the short molecular axis.

Because of C_{2v} symmetry reasons, the dipole moment of the BODIPY molecule is oriented along the short molecular axis.

Theoretical calculations suggest that the transition from the ground to the first excited electronic state in BODIPY is mainly due to a promotion of one electron from the HOMO to the LUMO orbital [69]–[71]. As explained in [64], the major contribution to the HOMO and LUMO states is given by the resonant structure ‘d’, and the results of calculations suggest an important enhancement of the electron density at the central 8 position of the dye in the LUMO with respect to the HOMO state [72], [65]–[67]. As consequence, the excitation from the ground to the first excited electronic state leads to a decrease in the dipole moment. We will verify the importance of this result in our photophysical characterization of BODIPY dyes in Section 2.3.

In addition to the wide range of potential applications in numerous research fields, the general attractiveness of these dyes is also related to their facile synthesis and structural versatility and to their excellent spectroscopic properties.

BODIPY dyes without any substituent are strongly UV-absorbing small molecules with high molar absorption coefficient ($\varepsilon \approx 10^5 M^{-1} cm^{-1}$) and they are highly fluorescent relatively to porphyrins and phthalocyanines [59]. The absorption spectra of BODIPYs generally show an intense band corresponding to the transition from the ground to the first vibrational level of the first excited state, from now on denoted as S_0-$S_{1\text{-}0}$, and a more or less pronounced shoulder related to the transition to the first excited vibrational level of the excited state, S_0-$S_{1\text{-}1}$. The energy spacing between the two transitions can be assigned to a C-H out-of-plane vibration typical of the molecular C=C framework of the BODIPY core. The main absorption band and the emission band of the BODIPY core are located within the UV/vis region, at around 490 and 500 nm and are characterized by mirror symmetry, suggesting similar vibrational structures in both electronic states and consequently small Stokes shifts [63]. Other weaker absorption bands at shorter wavelengths can be assigned to the less probable transitions to higher singlet excited states [59], [40].

The shape of the absorption spectrum is quite independent on the dye concentration, suggesting the absence of significant intermolecular interactions and a scarce tendency to

self-associate [64]. This is a very important advantage with respect to other dyes because aggregation drastically reduces fluorescence intensity.

The favourable properties of BODIPYs as fluorescent dyes can largely be attributed to the rigidity of the π-system that leads to a high fluorescence quantum yields, which approaches the unit for certain BODIPY dyes. The shape of the fluorescence band is independent of the excitation wavelength, suggesting that a very fast internal conversion process occurs from the upper excited states to the fluorescent excited state [59].

The spectroscopic and photophysical properties of BODIPY dyes can be fine-tuned by functionalization at the appropriate positions of the core leading to absorptions from wavelengths of about 500 nm to NIR region. This is necessary to make use of these dyes as fluorescent probes and sensors in living systems. Now, we focus on the particular types of functionalization of the BODIPY core characterizing the samples under study in the following sections.

The introduction of appropriate aromatic groups at the *meso* position of the BODIPY core allows obtaining selective sensors of redox active molecules, pH probes, metal-chelators and biomolecule conjugating groups [50]. BODIPY dyes with an amino donor or a nitro acceptor linked by means of an aromatic ring at the *meso*-position work as fluorescent probes, and in particular as pH indicators [39], [73]. Their action is based on the so-called Photoinduced electron transfer (PET) mechanism through which the fluorescence of a molecule is quenched in polar environment at ambient temperature when the competitive electron transfer between the high fluorescent group (the BODIPY core in this case) and the non-fluorescent substituent occurs. The amino or nitro substituents, depending on their oxidation potentials relative to the excited state of the BODIPY core, can act as electron donor or acceptor, respectively. In the first case, if electron transfer occurs, the excited state of the fluorescent group is acting as an acceptor and is reduced (reductive-PET or a-PET). In the second case instead, the energy states are such that the BODIPY core can donate electron to the substituent, being oxidized (oxidative-PET or d-PET). For example, 8-(anilino) compounds are typically used as pH sensors: at low H_3O^+ concentration, the fluorescence is quenched because reductive-PET occurs, whereas the coordination of the proton restores the typical fluorescent properties inherent to the BODIPY molecule [50], [39].

Theoretical calculations have demonstrated that the introduction of alkyl groups, also the less bulky methyl groups, at the 1 and 7 positions of the BODIPY molecule (Figure 2.1) in presence of a phenyl group substituent at the *meso* site, leads to a nearly perpendicular configuration with respect to the core [74]–[77]. This conformation, due to the geometrical restrictions imposed by the two methyl groups at the 1 and 7 positions, avoids any possible

resonance interaction between both aromatic systems. These theoretical results are supported by experimental proofs showing that the introduction of the phenyl group at the 8 position of the BODIPY core does not induce drastic change in the photophysical properties of the chromophore. On the other hand, Li et al. [75] proposed a coplanar conformation for the 8-phenyl substituted dye in absence of the alkyl groups at the positions 1 and 7, with consequently drastic changes on the absorption and fluorescence spectra.

On the base of these considerations, the 8 (or *meso*) position of the BODIPY core in presence of the alkyl groups at the adjacent positions is also referred as orthogonal position.

The increasing interest for BODIPY dyes has also involved the field of biotechnology. If opportunely functionalized with carboxylic acid functional groups, these dyes can act as fluorescent probes of proteins or DNA derivatives [78]. The BODIPY core is hydrophobic and it is advantageous to have water-soluble dyes that can exists in the aqueous environment surrounding a biomolecule and that can be easily conjugated without perturbing it. Despite their practical value, only few water-soluble BODIPYs are reported in literature. Among these, sulfonated derivatives at the position 2 and 6, resulted the most susceptible to electrophilic attack, are the best examples. From the spectroscopic point of view, it has been verified that the introduction of sulfonate groups does not change significantly the absorption and fluorescence maxima with respect to the unsulfonated dyes [50].

The typical emission of an 8-phenyl substituted BODIPY dye occurs at wavelengths shorter than the ones required for a fluorophore compatible with biological media. This is because scattering of light, significant background emission or absorption by tissues and cells are minimized in the so-called biological window - between 650 and 900 nm - and thus it results particularly convenient to work in this spectral region. Besides the wavelength of absorption, an ideal NIR dye should be characterized by high molar absorption coefficient and fluorescence quantum yields, and by the possibility of facile functionalization for labelling purposes. In this respect, BODIPY dyes has increasingly gained attention in the last decades [79], [80]. Among the different strategies to push the absorption and emission of these dyes to the far-red and NIR region, the introduction of styryl substituents in position 3 and/or 5 have proven to be particularly useful to extend the conjugation of the π-system [39], [40], [50]. In this way, several PET operative far-red and NIR BODIPY-probes have been realized, in which the probe moiety is usually attached at the ortho-position to decouple with the fluorophore [63].

2.2 BODIPYs under investigations

The BODIPY dyes characterized in this thesis have been supplied through the collaboration with the Dept. of Chemistry of the University of Messina (Prof. M.Cordaro) and ISMN-CNR Messina (Dr. M. Castriciano) and are functionalized *ad hoc* with the final aim to obtain dimers of BODIPY molecules linked by hydrogen bonds. Figure 2.3 illustrates their structures. In order to easily identify the different samples, we have chosen suitable acronyms reflecting their differences in functionalization:

- NO_2-BDP (a) and NH-BDP (b) to indicate the introduction of the nitro and of the secondary amine at the para position of the phenyl ring in the *meso* site of the BODIPY core;
- SO_3-BDP (c) to indicate the presence of the sulfonate groups at the 2 and 6 positions of the BODIPY core;
- MONO BDP (d) to denote the introduction of a styryl branch at the 3 position of the molecule; BIS BDP (e) to indicate also a second styryl moiety at the 5-position;
- NO_2-BIS BDP (f) to refer to the presence of both the nitro group in the phenyl ring at the 8 position and to the styryl branches at the 3 and 5 sites.

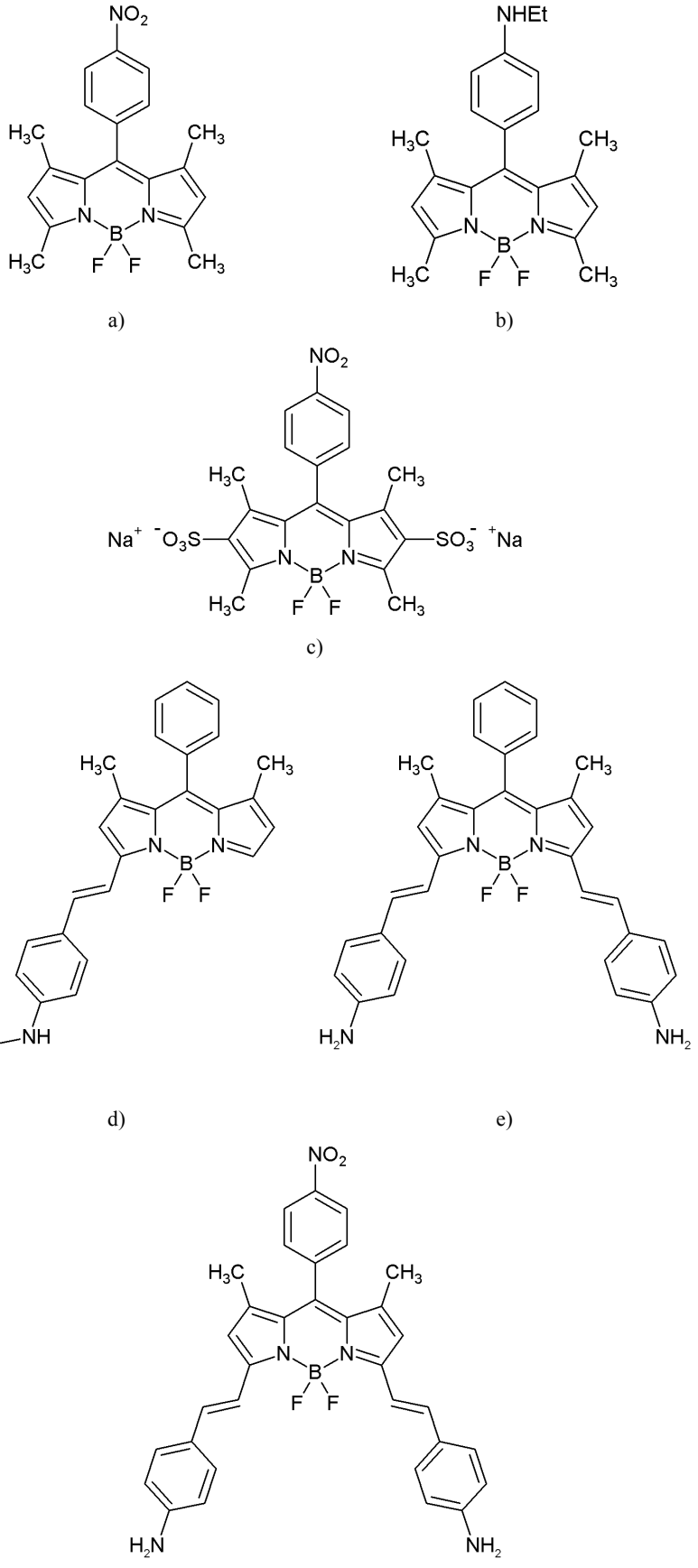

Figure 2.3 BODIPYs under investigation: NO_2-BDP (a) NH-BDP (b) SO_3-BDP (c) MONO BDP (d) BIS BDP (e) NO_2-BIS BDP (f).

It is possible to notice that all samples have two methyl groups at the 1 and 7 positions and a phenyl substituent at the 8 site. As explained in the previous section, the aromatic ring is expected to have a nearly perpendicular orientation with respect to the BODIPY core owing to the steric hindrance promoted by the methyl groups [64]. For this reason, there is no conjugation between the two π systems in all the cases and we should expect that the photophysical properties observed for these dyes are not influenced by the introduction of the phenyl substituent at the 8 position. On the other hand, effects that are not related to π-conjugation but to the presence of the donor NHEt or acceptor NO_2 group on the phenyl ring in the cases a), b), c) and f) are reasonably expected. Note that the presence of sulfonate groups in sample c) makes it compatible with aqueous solvents. Three of the samples of interest are functionalized with styryl groups at the 3 or/and 5 positions. The para position of the phenyl ring of styryl groups is in turn functionalized with an amide group in the case of MONO BDP d) and with an amino group in that of BIS BDP and NO_2-BIS BDP. In literature the effect of these donor substituents at the two styryl moieties that are conjugated with the BODIPY core is well explained [63], [50]. Depending on their electron-donor power, they may lead to a further red shift, although smaller, in addition to that due to the extension of conjugation provided by the styryl groups, with respect to the unsubstituted dyes. However, in our analysis we cannot distinguish between the two sources of red shift in absorption and fluorescence spectra since we have not the sufficient combinations of substituted samples to make this comparison. Therefore, aware of this, we will attribute the bathochromic shifts observed in the spectra of the styryl-substituted dyes only to the effect of the extended conjugation. Finally, the study of the influence provided by the introduction of the nitro group at the phenyl substituent in the orthogonal position to the BODIPY core is proposed.

In the light of this, the purposes of the following analysis are:

- to study how the different electronic properties of the NHEt and NO_2 groups, differing in their electronegativity, act on the photophysics of samples a) and b);
- the characterization of the only water-soluble sample c) in aqueous environments, keeping in mind that possible changes of the photophysical properties are not due to the presence of sulfonated groups [50], [64];
- the comparison between MONO and BIS BDP in order to study the influence of the different degree of both conjugation and branching;
- the study of the effects provided by the introduction of the nitro group at the phenyl ring orthogonal to the BODIPY core, by comparison with the unsubstituted BIS BDP;

- the study of the influence of solvent on the photophysical properties of these dyes, focusing the attention particularly on BIS and NO_2-BIS BODIPY, that are the main object of the 2D characterization developed in Chapter 4.

The characterization of the photophysical properties correlated to the structural changes of the available dyes will be extended to BODIPYs differently functionalized in further future analyses, with the final aim to focus the attention on dimers of BODIPY dyes.

2.3 Linear characterization and electronic properties of BODIPYs

The results of the absorption and fluorescence analysis of BODIPYs under investigation are reported below, focusing particular attention on the aspects highlighted in Section 2.2.

The small amounts of samples available prevent us from characterizing the photophysical properties in a quantitative way (in terms of extinction coefficients and quantum yields). For this reason only normalized spectra will be shown. Solutions have been prepared in different solvents according to the nature of each sample and the purposes of the characterization.

2.3.1 Absorption and fluorescence spectra

Absorption spectroscopy measures the intensity of light absorbed by samples, scanning a range of wavelength selected by a monochromator, and provides information about the energy of electronic excited states. Emission spectroscopy, measuring the intensity of light emitted by a sample after excitation, is performed keeping excitation wavelength fixed and scanning the emitted light. It is also possible to record excitation spectra scanning the excitation wavelength. Emission spectra provide complementary information to absorption ones about the vibrational structure of the ground state. Excitation spectra supply the same information of absorption spectroscopy, with the advantage to be applicable also in the case of opaque samples or mixtures of chromophores adsorbing in the same spectral region but emitting at different wavelength. Absorption and fluorescence spectra in this thesis have been recorded by means of a Varian Cary 5 spectrometer and a FluoroMax by Jobin Yvon, respectively.

NH-BDP and NO_2-BDP: effect of the substituent in 8 position

The absorption and fluorescence emission end excitation spectra reported in Figure 2.4 for both NO_2-BDP and NH-BDP are recorded in tetrahydrofuran (THF).

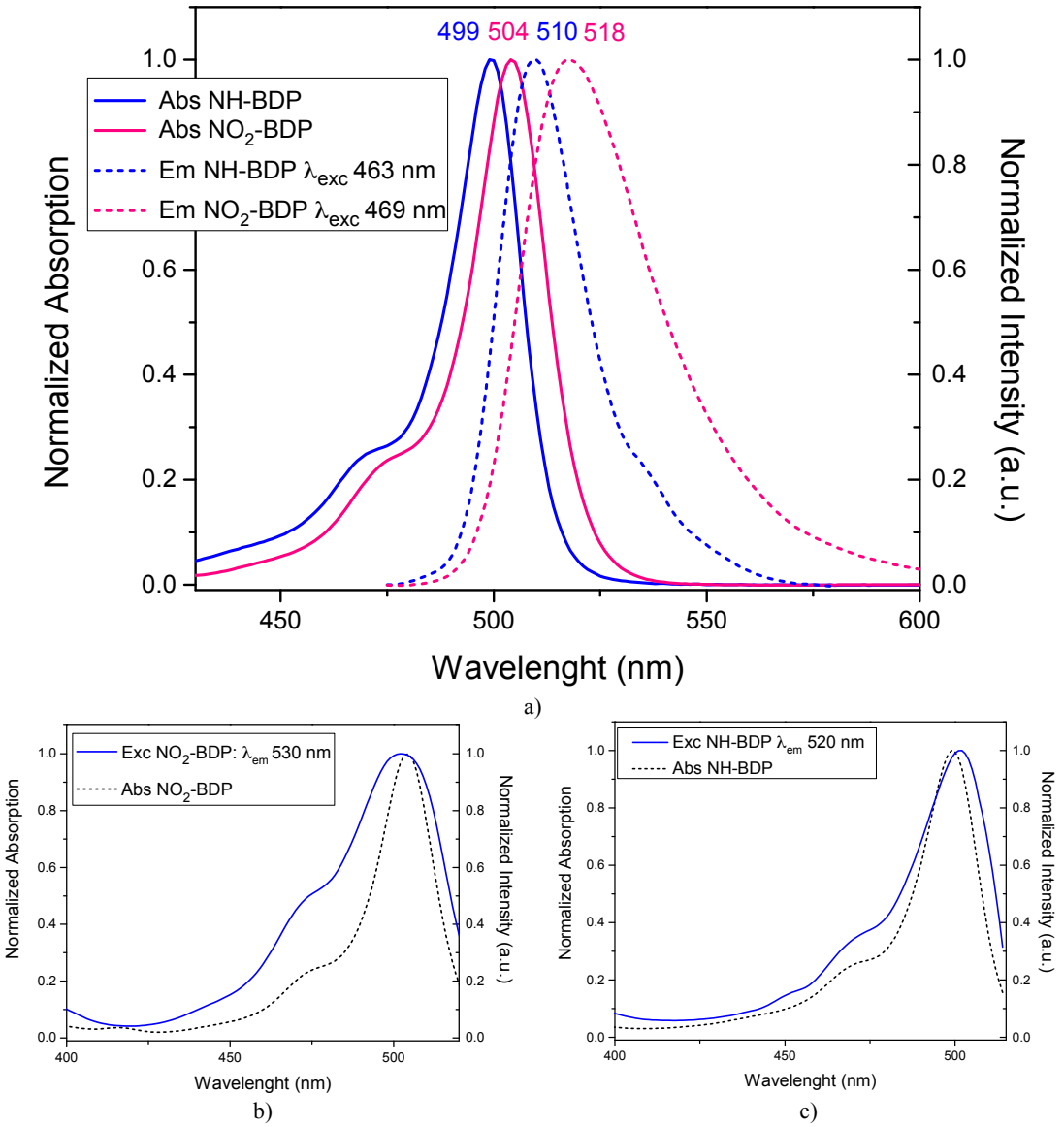

Figure 2.4 Normalized absorption and emission spectra of NO_2-BDP and NH-BDP in THF (a). Normalized excitation spectrum compared with the normalized absorption spectrum for NO_2-BDP (b) and NH-BDP (c) in THF.

The absorption spectra of both NO_2- and NH-BDP show the main absorption band, relative to the S_0-$S_{1\text{-}0}$, at 504 and 499 nm respectively and the shoulder relative to the S_0-$S_{1\text{-}1}$ transition. In both cases mirror symmetry characterizes absorption and emission bands, these last falling at 518 and 510 nm in NO_2- and NH-BDP respectively, suggesting the similarity of the vibrational structure in the ground and excited states. The Stokes shifts are of 11 nm and 14 nm in NH- and NO_2-BDP respectively. The shift of the spectra can be justified in the light of what explained in Section 2.1.1. Indeed, theoretical calculations suggest that the 8 position is very sensitive to the substituent effect because during the S_0-$S_{1\text{-}0}$ transition it

undergoes an increase of the electronic density going from the HOMO to the LUMO state. For this reason, the presence of an electron-donor substituent such as the amino group at the *meso*-position of the BODIPY core induces a net destabilization of the LUMO state, because of its high electronic density at this position, while the HOMO state is unaltered. Consequently, the energy gap increases and is reflected in a blue-shift of the spectral bands. The opposite for the presence of an electron-withdrawing nitro group at the same position: in this case its electron-removal effect relaxes the high electronic density acquired by the LUMO orbital during the electronic transition, inducing a net stabilization relatively to the HOMO state. It follows a decrease of their energy gap and a correlated bathochromic shift of the spectral bands [66], [67], [81]–[83].

The excitation spectra of both the dyes do not match perfectly the corresponding absorption spectra; the bands are wider in the first than in the latter case, little shifted and characterized by a different intensity ratio between the main peak and the vibrational shoulder. This behaviour may suggest the presence of a complex relaxation dynamics. This discussion will be completed with the results from the time-resolved fluorescence in Section 2.3.2.

Water-soluble SO_3-BDP

The absorption and fluorescence spectra of this unique case of BODIPY compatible with aqueous environments have been recorded in both water and methanol (MeOH) solutions. They are shown in Figure 2.5. The dielectric constants for these solvents and THF are reported in Table 2.1.

Table 2.1 Dielectric constants of the three selected solvents

Solvent	Dielectric constant
THF	7.58
MeOH	32.7
Water	80.1

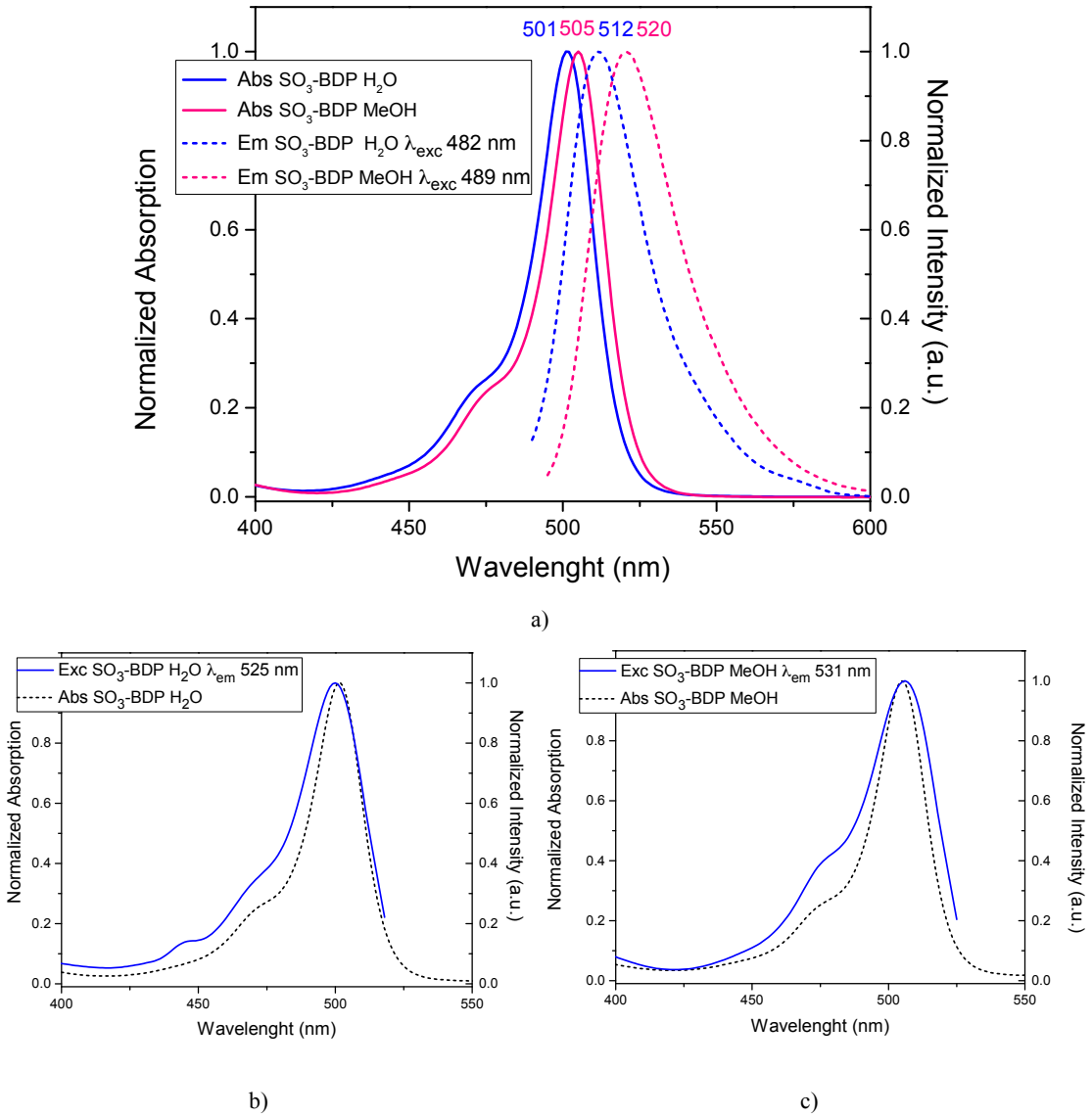

Figure 2.5 Normalized absorption and emission spectra of SO_3-BDP in H_2O and MeOH solutions (a). Normalized excitation spectrum compared with the normalized absorption spectrum in H_2O (b) and MeOH solution (c).

Also in this case, both the S_0-$S_{1\text{-}0}$ and S_0-$S_{1\text{-}1}$ vibronic bands can be observed, the first centred at 501 and 505 nm in H_2O and MeOH solution, respectively. A slightly greater shift affects the fluorescence bands, at 512 and 520 nm respectively, which are the mirror image of the S_0-$S_{1\text{-}0}$ absorption band. The Stokes shifts are of 11 nm and 15 nm in H_2O and MeOH solution respectively. A slight hypsochromic shift of both absorption and emission spectra has been recorded with increasing the solvent polarity. This effect is correlated with the decrease of the dipole moment upon excitation, with the LUMO being destabilized by the more polar solvent with respect to the other [67], [64].

The excitation spectra do not match the corresponding absorption ones suggesting also in this case a complex relaxation dynamics for SO_3-BDP.

Therefore, as reported in literature, the small changes observed in the photophysical properties of the SO_3-BDP with respect to the analogue NO_2-BDP are not correlated to the presence of the sulfonate group in the first case, but to the different solvent [50], [65].

MONO and BIS BDP: the effects of branching and conjugation

The absorption and fluorescence spectra for MONO and BIS BDP in Figure 2.6 are recorded in THF.

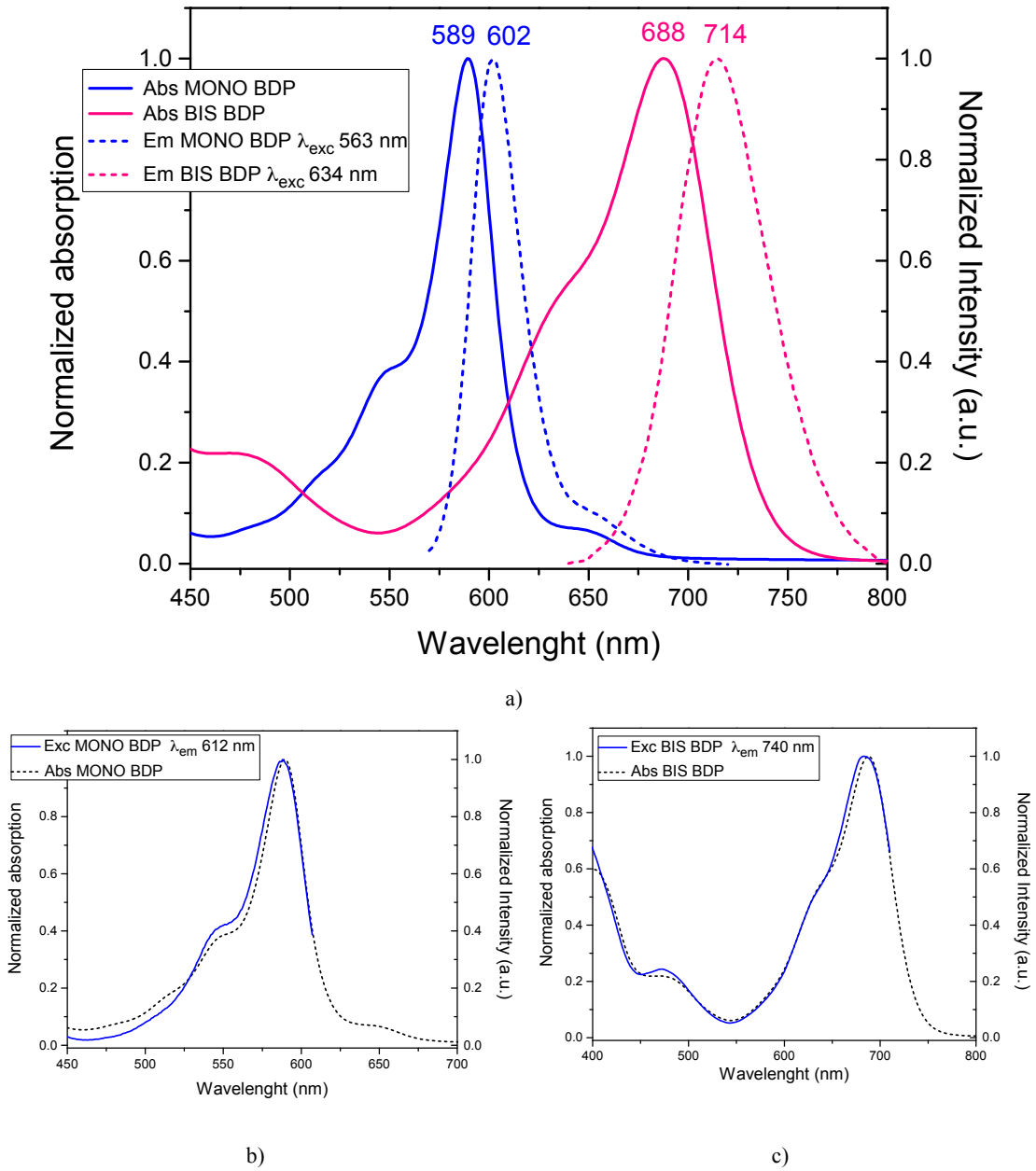

Figure 2.6 Normalized absorption and emission spectra of MONO and BIS BDP in THF (a). Normalized excitation spectrum compared with the normalized absorption spectrum for MONO BDP (b) and BIS BDP (c) in THF.

The main absorption and emission bands of MONO BDP are located at 589 nm and 602 nm resulting in a red shift of about 90 nm and 100 nm with respect to the previous samples. The

introduction of the second branch in BIS BDP induces a further red shift of about 100 and more than 100 nm with respect the mono-substituted dye, resulting in an absorption and emission maxima centred at 688 and 714 nm, respectively. The Stokes shift doubles going from MONO BDP (13 nm) to BIS BDP (26 nm).

In addition, a greater bandwidth is observed in the absorption and emission bands of the BIS BDP with respect to that of the MONO BDP. The presence of different possible configurations in solution for molecules with two styryl branches is a presumable explanation.

Contrarily from the previous cases, the excitation spectra of both MONO and BIS BDP are in a fairly good agreement with the absorption ones. Only little discrepancies due to scattering effects and instrumental factors are observed.

BIS BDP and NO_2-BIS BDP: the nitro-substituent effect and the solvent influence

The normalized absorption and fluorescence spectra of BIS BDP and NO_2-BIS BDP in both THF and MeOH are shown in Figure 2.7. Table 2.2 reports the values of the absorption and emission maxima and of the relative Stokes shift.

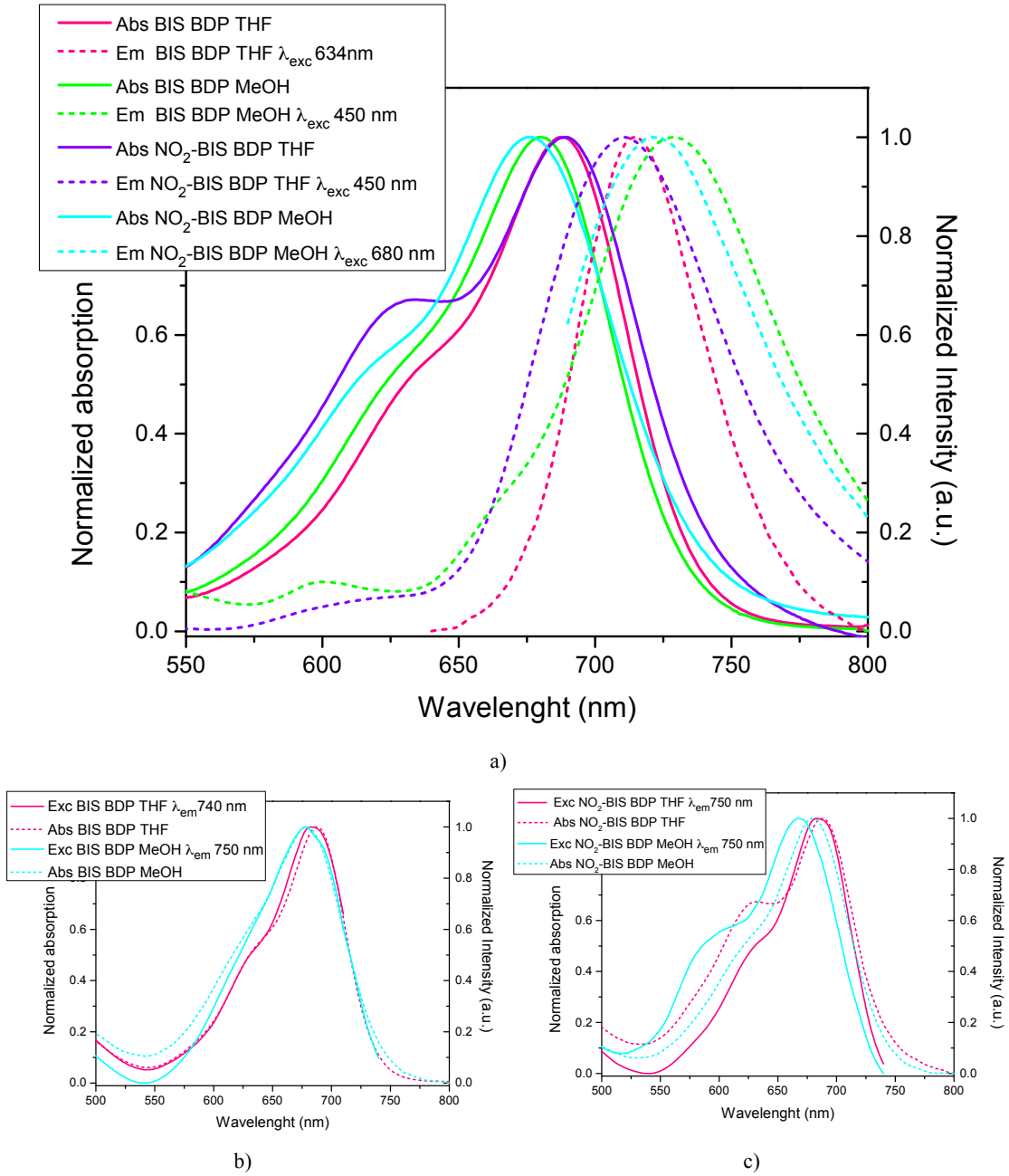

Figure 2.7 Normalized absorption and emission spectra of BIS BDP and NO_2-BIS BDP in THF and MeOH (a). Normalized excitation spectra compared with the normalized absorption spectra in THF and MeOH for BIS BDP (b) NO_2-BIS BDP (c).

Table 2.2 Absorption and Emission maxima for BIS BDP and NO_2-BIS BDP in both THF and MeOH.

Sample	Absorption maximum	Emission maximum	Stokes shift
BIS BDP THF	688 nm	714 nm	26 nm
BIS BDP MeOH	680 nm	729 nm	49 nm
NO_2-BIS BDP THF	688 nm	711 nm	23 nm
NO_2-BIS BDP MeOH	676 nm	721 nm	45 nm

In the comparison of the normalized absorption and emission spectra, the effect of the introduction of the nitro group on the relative shifts of the spectral bands is not well distinguishable owing to the broadening of the spectral bands characterizing the nitro-substituted dye. The nitro substitution induces a change of the shape of the spectra that appear more broadened than in its absence, and particularly the absorption spectrum in THF presents a more pronounced vibronic shoulder in presence of the substituent. This behaviour could be related to the change in the vibrational structure of the bands induced by the nitro group [82].

As we can notice from the values reported in Table 2.2, the Stokes shifts characterizing the two dyes in MeOH are greater than in THF. This is the consequence of the opposite shifts observed for the absorption and emission spectra in the more polar MeOH solvent to higher and lower energies respectively, with respect to what happens in THF. The first behaviour is expected since, as previously described, a more polar solvent destabilizes the LUMO, characterized by a smaller dipole moment. The behaviour observed for the emission spectra in THF and MeOH can be correlated to the different stabilization of the excited vibrational states provided by the two solvents.

The comparison between the absorption and fluorescence excitation spectra shows a fairly good agreement for BIS BDP in both solvents. On the other hand, the introduction of the nitro group leads to a drastic change in the shape of the excitation profiles with respect to absorption spectra. We can associate also this behaviour to the change of the vibrational structure induced by the introduction of the nitro substituent.

2.3.2 Time-resolved fluorescence

In order to verify the presence of the complex relaxation dynamics suggested by the very broadened excitation spectra, fluorescence lifetime of some of the investigated dyes, selected on the base of the amount of sample available, have been characterized through the so-called single photon counting technique (TCSPC) [84] available in our lab. By exciting the sample with a pulsed light source, such as a laser, and following the decay of the fluorescent intensity by means of an ultrafast photodiode, it is possible to measure the fluorescent lifetime. The TCSPC measurements have been made on NO_2-BDP, NH-BDP, MONO and BIS BDP in solutions of THF. A 150 fs frequency doubled Ti:Sapphire laser (exc-370-490 nm) is used as exciting source; the TCSPC apparatus has a time resolution of about 150 ps and allows investigating a time range of 12 ns after photoexcitation. Frequency resolved measures cannot be performed with this setup since the detector system integrates the signal emitted at all wavelengths. We are only able to make a roughly selection of the detection

wavelength by means of bandpass filters. The resulting fluorescence lifetime of the selected samples are compared by normalization procedure in Figure 2.8.

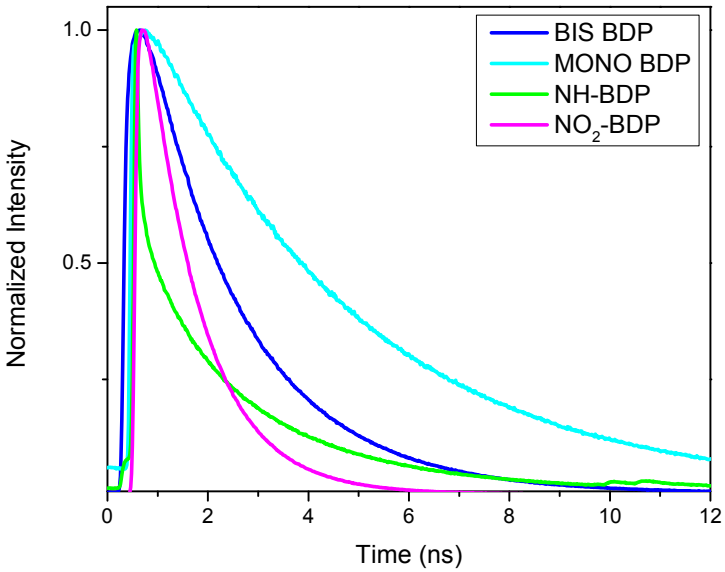

Figure 2.8 Normalized fluorescence decays of BIS BDP, MONO BDP, NH-BDP and NO_2-BDP in THF solutions.

The recorded dynamics reveals complex fluorescence decays that have been tentatively fitted with bi-exponential models for all the samples except for MONO BDP, showing a mono-exponential decay. These results are in accordance with the analysis of the excitation profile and their comparison with absorption spectra. The time constants provided by the mono and bi-exponential fits are reported in Table 2.3.

Table 2.3 Time constants of the fluorescence decays. The numbers in parentheses indicate the percentage contribution of each component. The reported time constants are the results of repeated sets of measurements and the estimated experimental error amounts at about 10% of the reported value.

	τ_1 (ns)	τ_2 (ns)
MONO BDP	4.29	/
BIS BDP	1.87 (89%)	3.14 (11%)
NO_2-BDP	1.07 (99%)	4.96 (1%)
NH-BDP	0.83 (33%)	2.62 (67%)

The recorded lifetimes are in agreement with those reported in literature for differently functionalized BODIPYs, characterized by typical lifetimes in the order of 1-10 ns [42]. A full comprehension of the revealed complex dynamics in the nanosecond regime and the attribution of the different time constants to specific processes is non trivial and needs further measures that are planned in the future. A detailed characterization of the

fluorescence lifetime goes beyond the scope of this thesis, since the focus here was on the characterization of the ultrafast relaxation dynamics (less than 1ps after excitation), that we report in the Chapter 4.

2.4 Vibrational properties characterization

With the final aim to have a support for the characterization of the vibrational modes involved in the coherent dynamics investigated by means of 2D spectroscopy, the vibrational modes active in the ground state of the samples of interest have been preliminary characterized by means of Raman Spectroscopy [85]. The Raman experiment is based on the scattering of light occurring when a monochromatic radiation provided by a laser source passes trough a medium. The intensity of the diffuse radiation is measured at a certain angle with respect to the incident direction. The Raman spectrum provides information about the vibrational modes characterizing the sample, which are the responsible of the phenomenon of scattering. The positions of the peaks observed in a Raman spectrum are usually reported as Raman shift in order to make the energy of the vibrational states responsible of the scattering independent on the excitation frequency. If performed in resonance conditions with respect to an electronic transition, i.e. the laser energy is chosen to match as closely as possible that of the absorption band, the Raman spectrum provides information about the vibrational modes that are strongly coupled with the electronic transition, whose intensity gets enhanced with respect to the spectrum recorded in non-resonant conditions.

The Raman characterization reported here has been performed with the collaboration of Prof. D. Pedron of the Dept. of Chemical Sciences in Padova, by means of a home-built micro-Raman system, based on a Triax-320 ISA spectrograph coupled to different excitation sources. Given the complexity of the Raman analysis, we fully characterized only the samples that, from what reported in Section 2.3, resulted to be more suitable for the characterization trough 2D spectroscopy. In particular, we will focus the attention on MONO, BIS and NO_2-BDP whose main absorption bands fall in the best spectral region covered by our laser.

Non-resonant Raman spectra under the best experimental conditions for this apparatus (excitation at 514 nm) have been recorded for all MONO, BIS and NO_2-BDP, while it has been possible to record the resonant Raman spectrum at 633 nm only for NO_2-BDP, owing to the smaller amounts available of the other samples. The overlap between the resulting non-resonant Raman spectra for MONO and BIS BDP, and the non-resonant and resonant spectra for NO_2-BDP are shown in Figure 2.9 and Figure 2.10, respectively. The identification of the main vibrational modes observed is reported in Table 2.4 for MONO

and BIS BDP and Table 2.5 for NO_2-BIS BDP. These tables will be vey important in the interpretation of the 2D response, as will be outlined in Chapter 4.

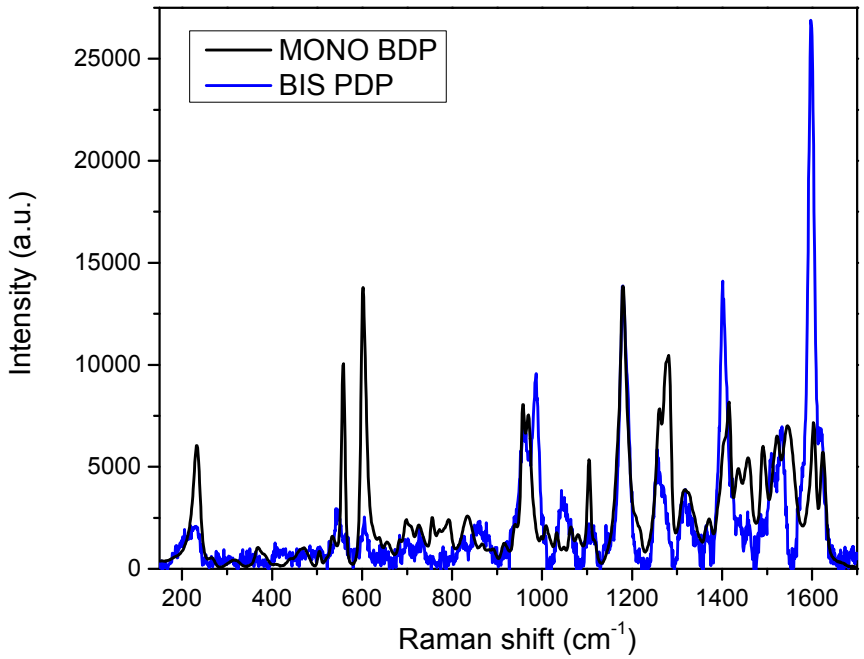

Figure 2.9 Non-resonant Raman spectra for MONO and BIS BDP.

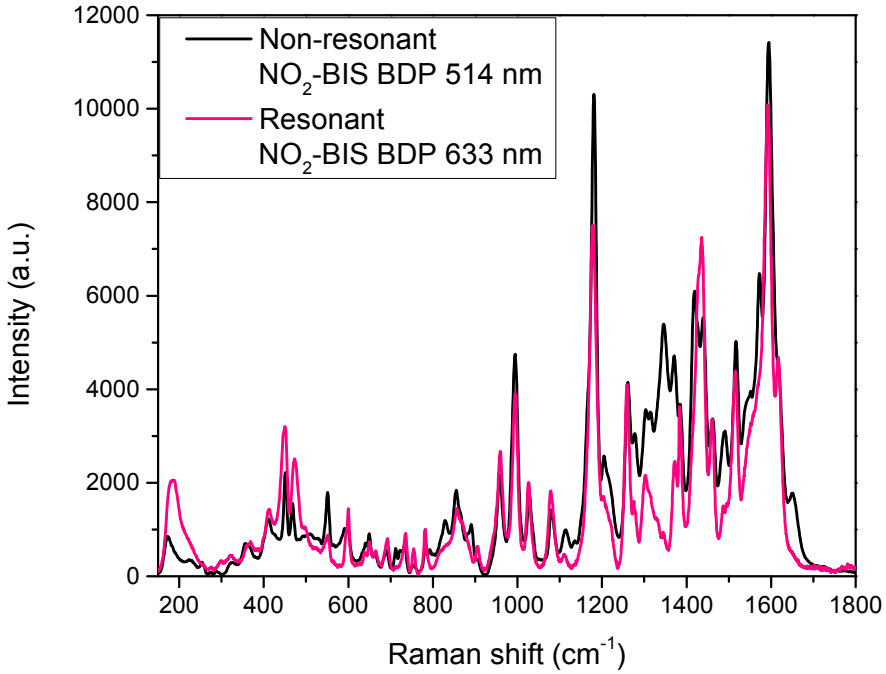

Figure 2.10 Comparison between non-resonant and resonant Raman spectra for NO_2-BIS BDP.

Table 2.4 Identification of the main vibrational modes observed in the non-resonant Raman spectra for MONO and BIS BDP. Data are reported in cm^{-1}.

Raman modes MONO BDP (cm^{-1})	Raman modes BIS BDP (cm^{-1})
230	230 weak signal
560	540 weak signal
600	600 weak signal
700-790 weak signals	
830 weak signal	860 weak signal
960	960
	990
	1040
1100	1100 weak signal
1180	1180
1260-1280	1260
1320	1320
1400	1400
1430-1545	1530
1600	1600

Table 2.5 Identification of the main vibrational modes observed in the non-resonant and resonant Raman spectra for NO_2-BIS BDP. Data are reported in cm^{-1}.

Non-resonant modes NO_2-BIS BDP (cm^{-1})	Resonant modes NO_2-BIS BDP (cm^{-1})
180 (weak signal)	180
450	450
550	550 (weak signal)
600 (weak signal)	600
650-780 (weak signals)	650-780 (weak signals)
860	860
960	960
990	990
1030	1030
1080	1080
1180	1180
1260	1260
1300-1370	1300
	1380
1420-1430	1430
1520	1520
1590	1590

In the analysis of the spectra it is important to stress that is not fully possible to make quantitative comparison between spectra, for example comparing the intensity of a signal at a certain frequency in MONO and BIS BDP. This operation would require indeed sophisticated calibration procedures that go beyond the scope of this thesis.

It is however possible to capture some qualitative interesting features. There is a fairly good agreement between the frequencies of signals detected for MONO and BIS BDP. However, it can be noticed that in the BIS BDP the low frequency modes in the range 400-800 cm^{-1} seem to be suppressed with respect to the higher frequency modes above 1000 cm^{-1}. A similar trend will be also observed in 2D measures (Chapter 4).

Resonant and non-resonant Raman spectra recorded for NO_2-BIS BDP are in good agreement as for the frequency modes, as for their relative intensities, although the 180 and 450 cm^{-1} modes seem to be slightly enhanced by resonant conditions. This may suggest a relevant coupling of these vibrations with the main electronic transition of NO_2-BIS BDP.

Chapter 3

2DPE: experimental setup and raw data analysis

3.1 Experimental setup

The 2DES experiment consists in detecting the third order signals as function of the time delays between pulses, deriving from the interaction of the ultrafast laser pulses with the sample solution.

Our 2DPE experiment is implemented with a fully non-collinear setup in which four beams having different wave vectors propagate parallel along the vertices of a square to be finally focalized on the sample. This approach is that of the so-called BOXCARS geometry, ideal for the non-collinear configuration. It allows in fact reducing potential sources of contamination of the echo signal, so that background consists only of spurious scatter. In this way lower excitation energies are required, minimizing saturation effects and the risk of higher order non-linear signals which could obscure the response function of interest [27]. The signal detection is based on the heterodyne scheme, in which the interferences between the signal and a local oscillator propagating in the same direction are acquired. It presents many advantages with respect to the homodyne detection based on the acquisition of the signal intensity, which we are going to treat in more detail in the next discussion. The scheme in Figure 3.1 illustrates the experimental setup built in our lab, whose elements are described in the next sections, as for the sequentially steps necessary to perform the experiment.

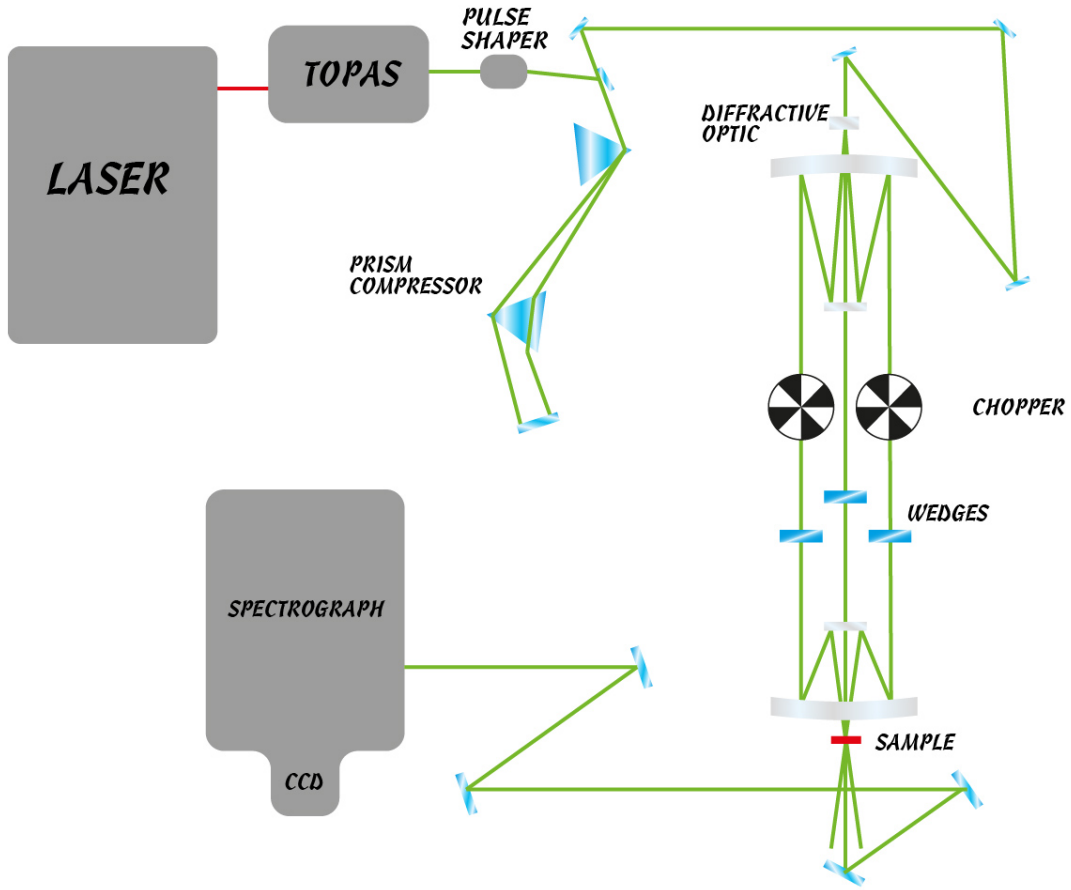

Figure 3.1 2DPE schematic setup.

3.1.1 Laser source

The laser source consists of a Coherent® Libra laser box based on a Ti:Sapphire system, containing a Vitesse oscillator pumped by a green laser (Verdi) and a regenerative optical amplifier (Regen cavity) pumped by a Nd:YAG laser (Evolution). A schematic representation is shown in Figure 3.2.

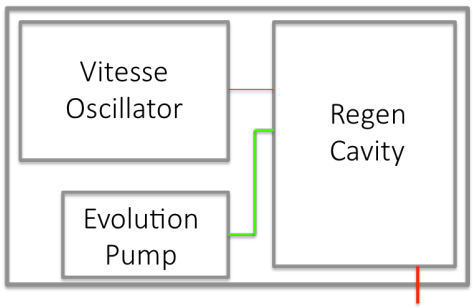

Figure 3.2 Libra laser composition.

The Ti:Sapphire crystal in the Regen cavity is pumped by the train of pulses at 800 nm generated by the Vitesse oscillator, with 80 MHz of repetition rate, each of 100 fs duration, bandwidth of 12 nm and an energy of 3,5 nJ. Seed pulses are first stretched in time by a grating before injection in the amplifier, in order to preserve the Ti:Sapphire crystal from the

high peak power of the pulses. The population inversion in the crystal is provided by Evolution, which generates pulses at 527 nm. The pulses in the Regen cavity are amplified up to 100.000 times and then sent to the grating compressor to restore the initial pulse duration of 100 fs. The output of the laser box is a pulse train at 800 nm with an energy of 0,8 nJ and 3 KHz of repetition rate [86].

3.1.2 Non-collinear optical parametric amplifier - *TOPAS*

The pulses emitted by the Libra laser enter the Light Conversion® Topas White, an automated non-collinear optical parametric amplifier (NOPA) [87], which converts the incoming 800 nm pulses into radiation whose central range can be tuned between 500 and 1100 nm. A beam splitter divided the incoming pulse into two parts: the 1% is focalized on a sapphire plate generating white-light continuum by means of non-linear effects, while the remaining 99% enters in the power-amplifier stage.

The white light beam is collimated with spherical mirrors and then focused into a phase shaper controlling the chirp of the pulse. This stage is also necessary to modulate the bandwidth of the final amplified pulse.

At the same time the remaining 99% of the main beam passes through a BBO ($Ba(BO_2)_2$) non-linear crystal which generates the 400 nm second harmonic of the pulse, then separated into a pre-amplification (5%) and a main pump beam (95%).

The white light pulse crosses the pre-amplification pump beam within a second non-linear BBO crystal and the resulting pre-amplified beam interacts with the main pump beam within the same crystal [87]. In this way only the white-light continuum components selected by the crystal angle is amplified. The final amplified beam exits the Topas White after collimation trough a mirror telescope and is then compressed by means of a compression system implemented in our lab.

3.1.3 Wavelength and phase control

A better spectral resolution can be obtained with shorter pulse duration. To this purpose it is important to work with the broadest bandwidth possible according to the Heisenberg indeterminacy principle: $\Delta E * \Delta t \geq \hbar/2$.

The pulse duration is also related to the phases of its spectral components, since the shortest pulse is obtained when all the wavelengths are in phase. The control of the chirp is therefore necessary to obtain the so-called transform-limited (TL) pulse. Optical materials, such as glass or fused silica, are usually characterized by wavelength-dependent refractive index, thus the different frequency components propagate with different speeds when the pulse

passes trough the transmissive medium. For example, the red component travels faster then the blue one. In this way a chirped pulse, whose wavelengths are characterized by different phases, results with a consequent time duration increase.

The frequency dependence of the phase of each spectral component can be expressed with a series expansion around the central laser wavelength ω_0:

$$\varphi(\omega) = \varphi(\omega_0) + \frac{d\varphi}{d\omega}(\omega - \omega_0) + \frac{d^2\varphi}{d\omega^2}(\omega - \omega_0)^2 + \cdots \quad (1)$$

While the first order is related to the time arrival of the pulse, the second and higher order terms must be zero since they represent the distortions of its temporal profile. Particularly, the second order is responsible of the linear drift of the phases of the different frequencies, also known as linear chirp. The higher orders are related to other phase distortions.

The correction of the second and higher orders to obtain a TL pulse is of crucial importance since chirped pulses are responsible of artifacts in the 2D experiment [88].

The pulse coming from the TOPAS is therefore subjected to the prism compressor, which is helpful to remove linear chirp, and the pulse shaper, which removes the higher order chirp terms. In this way a complete control of the phases of the pulse components can be achieved.

Prism compressor

It consists of a pair of transparent prisms made of a highly refractive material whose distance can be modulated to correct the linear chirp. The first prism deflects the wavelengths of the laser beam of different angles, thus introducing a different path-length in the red and the blue components when the laser pulse crosses the second prism. The prism compressor does not allow the correction of the higher chirp orders [27], which is provided by the next stage.

Pulse shaper: Fastlite-Dazzler

The Dazzler is an acousto-optic pulse shaper providing a complete control on the phases of ultrafast pulses, introduced by Pierre Tournois in 1997 [89]. It consists in a small rectangular box (10x5x2 cm), where the interaction between optical and acoustic waves, the latter generated by a piezoelectric device, takes place when the laser beam passes trough the crystal. The integrated software guarantees the control of the phase of each frequency component of the pulse.

3.1.4 BOXCARS geometry and time delays control

The 2DPE experiment consists in measuring the third order signal deriving by the interaction of three ultrafast pulses with the sample at different times. A fourth pulse called Local Oscillator (LO) is used for detection purposes. In order to select only those contributions to the signal corresponding to the Feynman paths we are interested, the phase matching and the time delay between pulses have to be chosen. The four pulses are arranged in a BOXCARS geometry, which is the ideal configuration for our non collinear setup (see Section 1.9 and Figure 1.8). The three exciting beams and the LO propagate parallel along the vertices of a square, before being focalized on the sample solution. BOXCARS geometry guarantees that the third order signal can interact with the LO that propagates in the same direction, thus allowing the detection of their spectral interferences. To this purpose the different wave vectors characterizing the three exciting pulses satisfy the phase-matching condition ($k_s = -k_1 + k_2 + k_3$) so that the signal is radiated in the direction of the fourth vertex and follows the LO path. The square geometry is obtained by means of a diffractive optic (DO) able to generate four identical replicas of the incoming beam. The power of diffractive optic in obtaining phase-stability and signal enhancing has been demonstrated by Miller et al. in 2004. The four pulses generated by DO have a common phase reference and the correct spatial relationship for non-collinear phase-matching [90].

The four beams are then collimated and propagate parallel to each other trough a series of optics, set up on the base of that proposed by Nemeth et al. [91], before reaching the sample. The excitation beams k_1 and k_3 are modulated by means of two optical choppers in order to improve the signal-to-noise ratio (double modulation technique). The LO intensity is attenuated by a neutral density filter by three to four orders of magnitude before it hits the sample; this guarantees that LO does not influence the system response [92].

Pairs of fused-silica wedges (1°) are applied on each of the exciting beams to realize time delays between them. One wedge of each pair is mounted on a translation linear stage (Aerotech Ant95) computer-controlled, which moves the wedge respect to the other with nm accuracy. Adding or subtracting fused-silica, the path of each of the three exciting beams in the glass can be increased or decreased. The definition of the time delays is recalled in Figure 3.3.

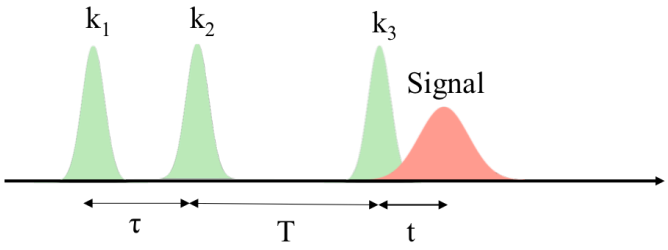

Figure 3.3 Time ordering of the pulses and definition of time delays: τ = coherence time; T=population time and t = rephasing or echo time.

Finally, a calibration procedure [92] provides the conversion of the positions of the translation stages in time delay, whit an accuracy of about 0,07 fs. This system allows obtaining time-delayed pulses without altering their directions. The four beams are then focalized on the cuvette of 1 mm pathlenght containing the sample solution. One of the main advantages of our setup is that the pulses at the sample position are identical, since they have travelled trough almost the same paths, crossing the same optics.

3.1.5 Signal detection

The third order signal is generated only when all excitation beams reach the sample and it is collected by a spectrograph (Andor Shamrock), which separates and focalizes different wavelength contributions on a charge coupled device CCD (Andor Newton) detector [93]. The spectrograph has three exchangeable gratings to work with the best resolution in different conditions; the CCD works at -40°C, with a sensor of 1024 pixel and a resolution of λ/1024.

For 2D setups, the direct collection of the intensity of the signal, corresponding to the square modulus of its electric field, (homodyne detection*)* is not convenient. For this reason, heterodyne detection is adopted, consisting in the acquisition of the interference between the signal and the LO propagating in the same direction. Heterodyne detection requires that LO has exactly the same direction of the signal and a comparable intensity. For this reasons BOXSCARS geometry is the ideal configuration satisfying the first requirement, and a neutral density filter is used to attenuate the LO before reaching the sample. The heterodyne acquisition is particularly convenient for weaker signals recorded by higher order spectroscopies, since it is able to improve the signal-to-noise ratio providing a linear (instead of quadratic) dependence of the signal intensity on its electric field. Another relevant advantage is that, knowing the phase between LO and the signal, it is possible to separate the complex electric field into real (absorptive) and imaginary (dispersive) parts trough the phasing procedure described in Section 3.2.1.

The signal collected by the CCD contains however many unwanted contributions, such as the homodyne signal ($|E_S|^2$), the LO spectrum ($|E_{LO}|^2$) and scattered exciting pulses which interfere in the direction of the signal and LO. A time filtering method based on Fourier filters described in Section 3.2.1 is applied in data processing routine in order to remove the interferences coming at times different from the delay between LO and the signal.

Applying the subtraction method proposed by Brixner et al. for scatter suppression [92], the spurious signals can be partially removed during the experiment by means of an automated shutter which blocks and unblocks the path of one of the parallel pulses (k_3). The signal recorded by the CCD when the path is blocked is subtracted to that acquired with the same path unblocked to give the final signal, partially cleaned from the unwanted contributions.

However, this procedure is not sufficient to remove fully all the unwanted contributions, therefore "*ghost"* features that lead to misinterpretations of the 2D signals still affect the 2D maps after application of this method [94]. To this purpose Zigmantas introduced a double modulation of exciting pulses by means of two optical choppers, in order to remove all non-modulated noise [94]. In our set up it is obtained by chopping k_1 and k_3 and collecting the third order signal at specific combinations of the modulated frequencies. This modulation technique is also able to eliminate contributions of slowly accumulating long-lived species, such as long-lived triplet states or isomers [94].

The total signal acquired by the CCD in presence of the double modulation can be expressed as follows:

$$I_{CCD}(\tau, T, \omega_t) = I_S(\tau, T, \omega_t) + Es(\tau, T, \omega_t)E_{LO}(\omega_t) * e^{-i(\omega_t t_{LO} + \varphi)} + cc. \quad (2)$$

A LabVIEW software automatically saves the 3D matrix of the interference between LO and the signal as function of the coherence time τ, the population time T and the Fourier analogue of the rephasing time t, ω_t.

3.1.6 FROG

The temporal profile of the pulse is characterized before each set of measurements through the frequency resolved optical gating (FROG) technique, in order to determine the temporal resolution of the experiment [95]. It is a third order technique based on the interaction between three pulses and a non-resonant material. We perform FROG taking advantage of the BOXCARS geometry of our 2D setup, simply replacing the sample with a solvent, typically CS_2 or DMSO and setting to zero the time delay between the two first pulses (k_1 and k_2). In this way the three pulses are characterized by the same properties of that in 2D measurements. The FROG experiment consists in scanning T in a range of about 100 fs,

which represents the delay between the two first pulses that arrive simultaneously on the solvent cuvette, and the third beam. As solvent transitions do not fall in the laser spectral range, the third order signal is emitted only when all the three pulses interact on the cuvette and is recorded in the same direction of the 2D signal, by means of the same detection scheme.

We are able to obtain information about the time duration of the pulses from the width of the FROG signal, which can be visualized trough a time-frequency map (Figure 3.4), which reports the temporal distribution of the instantaneous frequencies of the pulse [95].

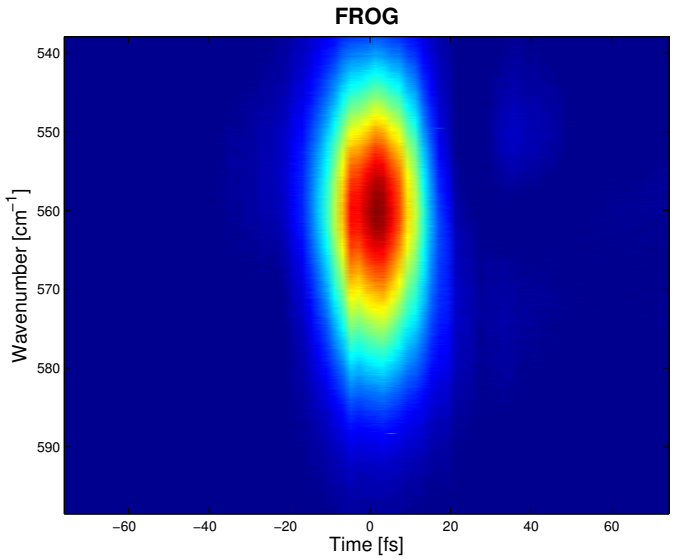

Figure 3.4 Experimental FROG signal in DMSO.

In order to generate the shortest pulse possible, we adopt an iterative procedure in which we optimize the pulse by adjusting the spectral phase with the Dazzler, until the best conditions are reached.

3.2 Data processing

The data processing is a very complex procedure totally based on a homemade routine by means of the proprietary MATLAB® software.

Each acquisition is performed scanning the population time T and the coherence time τ, using a randomized scan in order to remove the noise deriving from the background oscillations. The evolution along the rephasing time *t* is provided by the CCD calibration, which acquires the Fourier analogue of the third time delay *t*.

3.2.1 Raw data analysis

The raw data consists in a sequence of interferograms for each value of T acquired through LabVIEW software. The interferograms are 2D spectra of the interference between the echo and the local oscillator alone, which have τ and the wavelength values associated to the CCD pixels as x- and y-axis respectively, as shown in Figure 3.5 a).

First of all, we proceed with the interferogram manipulation. As the recorded signal is of the form of Eqn. 2, first of all the third order signal $I_S(\tau, T, \omega_t)$ has to be isolated from all the unwanted contributions to the total signal collected by the CCD. To this aim, a time Fourier filter procedure is applied in order to remove the residual scattering, the homodyne contributions and the interferences at times different from the delay between the signal and LO. The procedure consists in Fourier transforming the ω_t direction, setting to zero the noise contributions whose time delays differ from the delay echo-LO, and obtaining the clean interferogram by an inverse Fourier Transform.

To remove the LO contribution and recall the clean signal the following operations are applied:

- multiply the complex signal by $e^{-i(\omega_t(t_{LO}-t_{k3}))}$ in order to remove the time delay between LO and k_3;
- divide by $E_{LO}(\omega_t)$ which corresponds to the square root of the LO spectrum ($\sqrt{I_{LO}(\omega_t)}$), which is independently recorded for each acquisition in addition to the interferogram.

Finally, a Fast Fourier Transform along τ allows obtaining the final 3D matrix, consisting of a sequence of 2D maps having two frequency dimensions (along x and y), at increasing values of the population time corresponding to the z axis. Figure 3.5 illustrates the initial raw interferograms (a), the intermediate clean interferograms (b) and the final 2D maps (c), where all these spectra are piled up as a function of T.

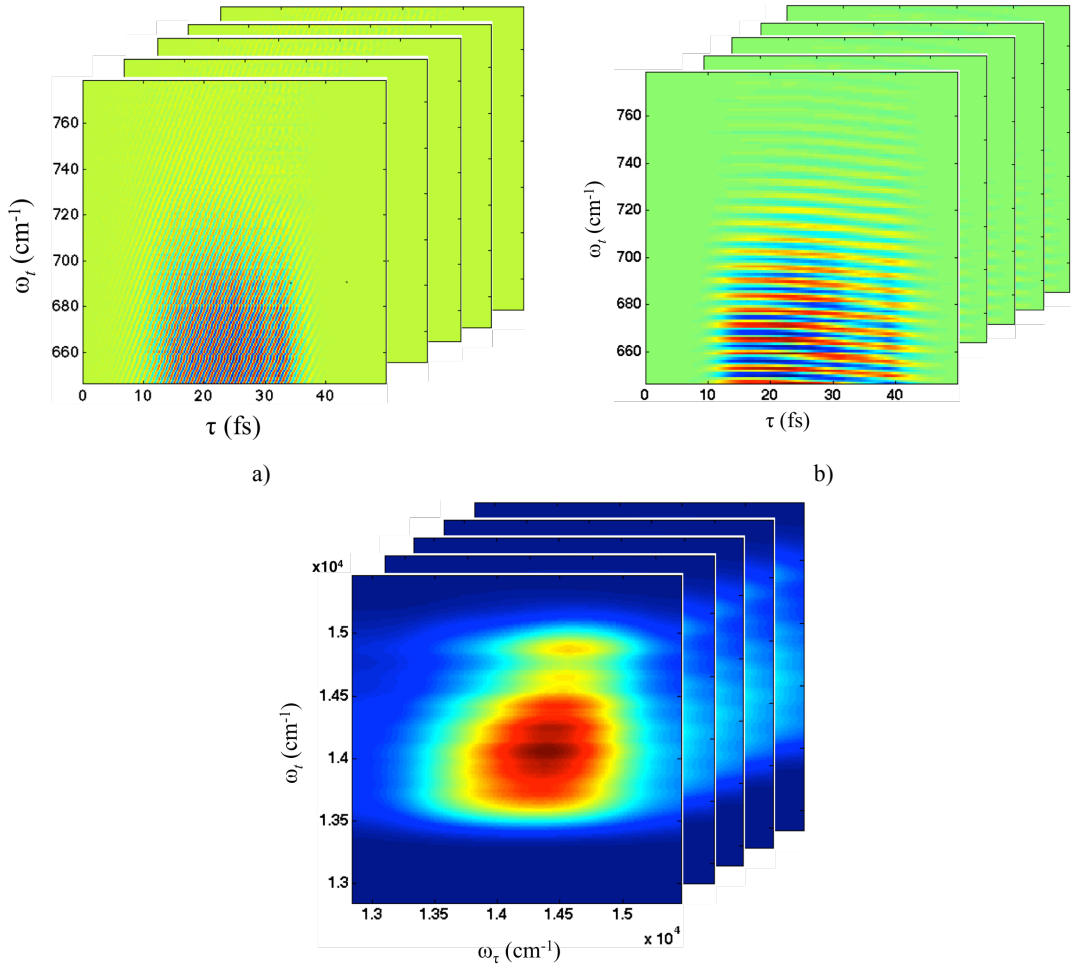

Figure 3.5 Correlation between the raw interferogram and the final 2D map. The excitation coordinate ω_τ (cm^{-1}) is obtained Fourier transforming τ (fs). The emission coordinate ω_t (cm^{-1}), corresponding to the Fourier analogue of the rephasing time *t*, and it is directly measured in wavelengths by the CCD. Raw interferograms along T (a). Clean interferograms along T (b). Final 2D maps along T (c).

As shown in Eqn. 2 the recorded signal is complex, thus it is necessary to separate the real component, corresponding to the absorptive phenomena, in which we are interested, from the refractive imaginary part. The extraction of the real signal can be performed in different ways [96], [97] and needs a phasing procedure, which may be source of artifacts. In our research group a *global phasing procedure* is adopted, and still under optimization. For this reason, the resulted presented in this work are mainly based on the absolute part of the recorded signal, in order to avoid the risk of artifacts due to this procedure.

3.2.2 2D maps analysis

Once that the 3D matrix of the third order signal is obtained, all the information relative to the relaxation dynamics of the system under investigation can be obtained, in an ultrafast time resolution.

Two-dimensional maps provide a lot of information in addition to that carried by the conventional absorption spectra: first of all, the analysis in both the frequency and time domain is allowed, meaning that it is possible to follow the ultrafast decay dynamics immediately after photoexcitation. The evolution of electronic, vibrational or vibronic coherences along the population time, by means of the response theory in the manner already discussed in Chapter 1, is also revealed. The features characterizing 2D maps provide information on the energy of the main states modulating the relaxation dynamic of the system, but also on the entity of their contributions in terms of intensity of the relative peaks. In addition, the shape of the observed signals is informative of homogeneous and inhomogeneous broadening deriving from the interaction with the environment fluctuations (see Chapter 1). The detailed analysis of the decay along the population time in each point of the 2D map allows identifying the contributions coming from different species or states, and particularly to follow energy transfer, as in multi-chromophoric systems, and relaxation processes. For example, we report in Figure 3.6 an evidence of relaxation dynamics in MONO BDP sample, detected through the simple analysis of the evolution of the 2D maps along the population time.

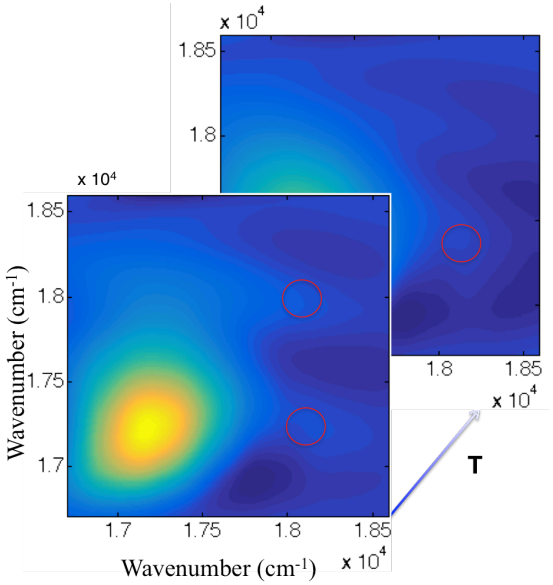

Figure 3.6 Evidence of a relaxation dynamic along T in MONO-BDP sample in THF. The red markers indicate the energy shift from the upper to the lower diagonal portion of the 2D maps. The decrease of the diagonal upper signal together with the increase of the off-diagonal one, can be clearly observed at increasing values of T. This evidence denotes a relaxation process from the initially excited upper state to the lower one indicated by the y-coordinate of the off-diagonal peak.

Among the many different methods reported in literature to make a global analysis of 2D maps [98], [99], our routine to characterize coherences is described in the following discussion. A multi-frequency oscillatory character affects the decay of the signal at each point of the map. Our aim is to extract the oscillations from the overall dynamics, since they are associated to the coherences in which we are interested, and the best way is to remove first the non-oscillating components of the signal. The most convenient method proposed by Van Stokkum is to perform a global fit of the decay of the whole map, by means of a suitable kinetic model [100], [101]. Instead of fitting the decay at each point of the map independently, considering the overall dynamics is most convenient since the same time constants relative to the evolution along T are obtained for the whole map. The subtraction of the fitting function from the overall signal leads to the 3D matrix of oscillating residuals on which the whole analysis aiming at the characterization of coherences is based. The global fit procedure can be applied on the complex, real or absolute data, and the respective 3D matrix of residues can be analysed independently. As we have already introduced, the analysis in this work is manly focused on the absolute part of the signal in order to avoid artifacts deriving from the phasing of the real data. The kinetic models we usually apply consists in multi-exponential functions, such as *geeec*, *geec*, *eeec* (with *g* a Gaussian function, *e* an exponential function and *c* a constant in the investigated window). The Gaussian function is introduced to take into account the effect of pulses superposition at very early times.

Once this procedure is applied, it is possible to visualize the result of the fit performed with the global kinetic model on each point of the map. Figure 3.7 illustrates an example of this type of analysis: the right upper panel (c) reports the overall decay dynamic extracted at the specified coordinates of the 2D map and the applied fitting model. The upper central panel (b) shows the oscillating residuals obtained subtracting the resulted fit from the experimental data.

The frequencies of the multi-oscillating components characterizing each point of the 2D map can be easily obtained by means of a *Fourier Transform* (FT) of the extracted residuals along T (Figure 3.7 d). The conventional Fourier Transform presents however a low frequency resolution when applied to oscillating highly damped signals, due to the limits provided by the time spacing and the signal duration. Therefore, we also perform the analogue *Linear Prediction Z-transform* (indicating as *LPZ* in Figure 3.7 d), which allows improving resolution through an estimation of non-recorded future points (in the time spacing) of a data series as a linear function of the experimental ones [102].

However, the Fourier analysis is able to extract from the oscillating signal only information about its frequency component, which can be view as averaged over the entire time domain. It is evidently not able to characterize signal components which last for very short times and whose frequencies are quickly changing [103]. On the other hand, information only about frequency of the beatings is not sufficient to identify the nature of the different components of the multi-oscillatory behaviour of the signal. The time resolution represents therefore an indispensable tool to interpret the main beating component and in studying their dynamics.

Time-frequency transforms (TFT), a recently analysis developed in our group, allows achieving this goal because they are able to spread the signal information along both the time and frequency domain simultaneously [103]. However, we must take into account the limits imposed by the time-frequency uncertainty principle in achieving an ideal independent resolution along both dimensions. For this reason, the performance of the time-frequency transform is particularly subjected to the risk of artifacts. TFT maps, i.e. 2D plots of the signal in the time-frequency domain, are obtained also in this case acting on the 3D matrix of residues. We use in particular a special combination of TFTs deriving from the product of the *Short-time Fourier Transform* and the *Smoothed-pseudo-Wigner-Ville* distribution (SPWV), which resulted to be particularly convenient [103]. The real and absolute components of this transform, the Abs-SPWV-STFT and Real-SPWV-STFT, are illustrated in Figure 3.7 e) and f) respectively. The absolute maps carry information about the intensity of the oscillations detected in the maps and their damping times, while the real maps allow identifying the relative phases between the different components.

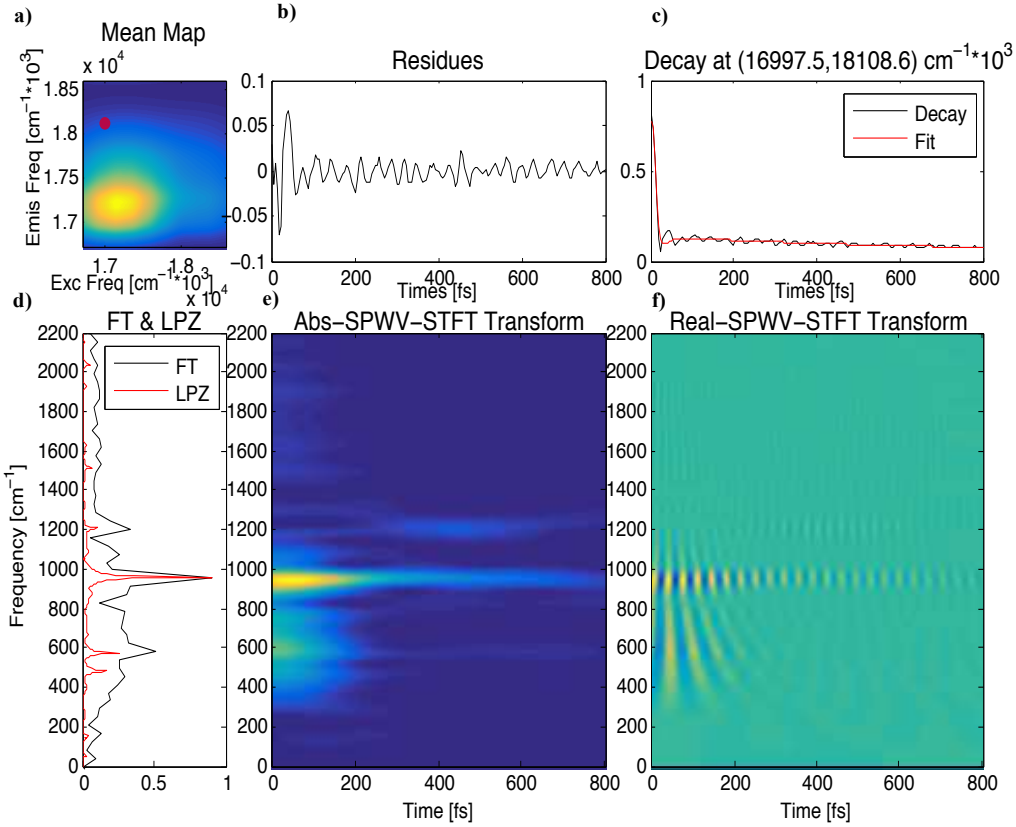

Figure 3.7 Example of the analysis performed on the multi-oscillatory behaviour of a single point of the 2D map. a) Coordinates of the decay trace extracted. c) Multi-exponential fit performed on the decay trace. b) Oscillating residuals are obtained subtracting the fitting function from the experimental trace. d) Fourier Transform and LPZ performed on the oscillating residuals. e) Absolute TFT map underlying the intensity of oscillations. f) Real TFT map also giving information about the phase of the oscillations.

In order to obtain information about the main frequencies contributing to the overall beating pattern, an integration along both the ω_τ and ω_t direction, followed by a Fourier Transform along the population time, is performed. The resulting amplitude is plotted as function of ω_T in what we refer as the *Fourier spectrum of coherences* (Figure 3.8).

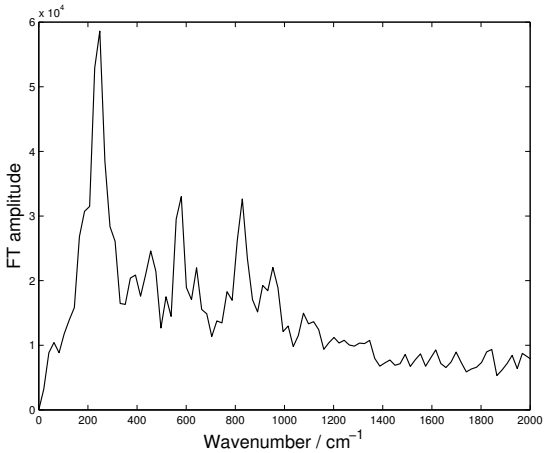

Figure 3.8 Example of Fourier spectrum of coherences.

In addition to this analysis, an extensively used method to reveal at which positions of the 2D map the main frequencies associated to coherences contribute more, is represented by the 'Fourier maps' [104]. This is a very important information to identify the nature of the states involved in the coherent dynamics. Starting from the 3D matrix of residues, we perform a Fourier Transform along T in each point of the 2D map [105] obtaining a 3D matrix consisting of 2D spectra (ω_τ; ω_t) stacked along ω_T. The Fourier map at a specific frequency, matching the energy gap of the states that are coherently coupled and therefore oscillate at this frequency, can be obtained taking a 2D slice of the matrix at the corresponding value of ω_T [35], [106]. Frequency maps with meaningful signals can be obtained only for relevant contributions to the overall oscillating trend, thus for these frequencies highlighted by the Fourier spectrum of coherences.

Fourier maps are 2D spectra in which the amplitude and phase distribution of the main frequencies contributing to the beating along T are plotted as function of ω_τ and ω_t similarly to the 2D maps. They provide a more direct visualization of the states that are coherently coupled at a specific frequency with respect to 2D maps. In agreement with the response theory, the positions of the signals appearing in a single 2D frequency map are informative about the nature of the coherence beating at the selected value of ω_T [34]. Figure 3.9 reports an example of Fourier map at a selected frequency. Dashed lines indicate all points on the map at a distance ω_T and 2 ω_T from the diagonal where signals predicted by the response theory should appear (see Figures 1.10 and 1.11).

We must take into account that artifacts due to the laser shape of the signal, which is correlated to the signal intensity, often affect Fourier maps. Therefore in this work we mainly refer to the analysis on selected single point of the 2D map to study the multi-oscillating behaviour associated to coherences.

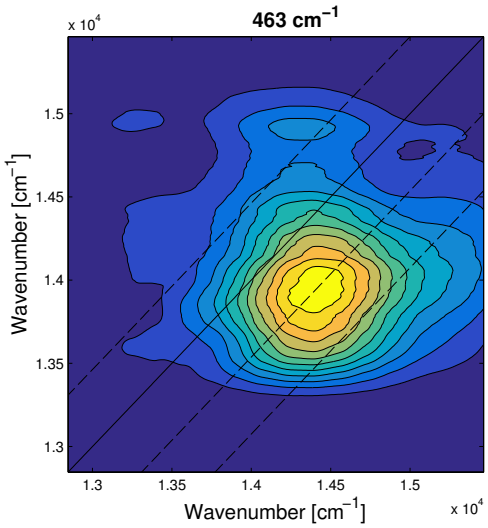

Figure 3.9 Example of experimental Fourier map.

Chapter 4

2DPE Characterization of BODIPYs

4.1 The goal

In the context of the current interests of this thesis, the attention in the following analyses is focused on the 2D Photon Echo ability to detect the influence of solvent and substituents introduced in the molecular structure on the relaxation dynamics of the investigated samples. The goal is to study how the interaction between the sample molecules and the solvation sphere is involved in the coupling between the vibrational modes and the electronic transition, in addition to the effects deriving by the introduction of substituents in chromophores as BODIPYs, whose photophysical properties are particularly sensitive to functionalizations.

For these purposes, the 2D-measurements have been performed on solutions of two different solvents compatible with the nature of the selected samples: tetrahydrofuran (THF) and methanol (MeOH). Among the large variety of BODIPY structures characterized by the conventional techniques as seen in Chapter 2, mono and distyryl-substituted BODIPYs have been chosen because their absorption fall in available spectral regions to be excited by the laser pulse.

In this way, the effects of two types of functionalization have been studied. The comparison between Mono- and Biariliden BODIPY, whose structures are shown in Figure 4.1 a) and b), has highlighted how the different degree of both branching and conjugation can affect the 2D response of these chromophores. In addition, the introduction of the nitro group in an apparently irrelevant position of the BODIPY structure has been investigated (Figure 4.1 c)). The role of the substituents in ortho position has been discussed in literature for long time, in particular to understand if they may or may not contribute to the conjugation of the BODIPY core [67].

An additional aim of the 2D characterization has been the exploration of different regions of the sample absorption spectrum, achieved through tuning of the exciting laser source, in order to compare the different types of information deriving. Our interest is particularly focused on the coherences evolving during the population time in the 2D detection, and on their ultrafast dynamics. Since we are dealing with isolate chromophores in solution, not involved in any type of energy transfer process, the focus of all the performed analyses has been the research of which vibrational states are coherently coupled with the electronic transition from the ground to the first excited state, and how this coupling affects the dynamics of this transition. For this reason, we expect to detect vibrational coherences representing superpositions of vibrational states within the ground or the excited electronic state.

The laser band has been initially tuned so to excite the vibronic band of the sample (Figure 4.2) in order to capture the relaxation dynamics involving higher vibrational levels in the excited state. Then, we proceeded centring the laser band on the red portion of the absorption spectrum in order to mainly characterize the vibrational coherences of the ground state.

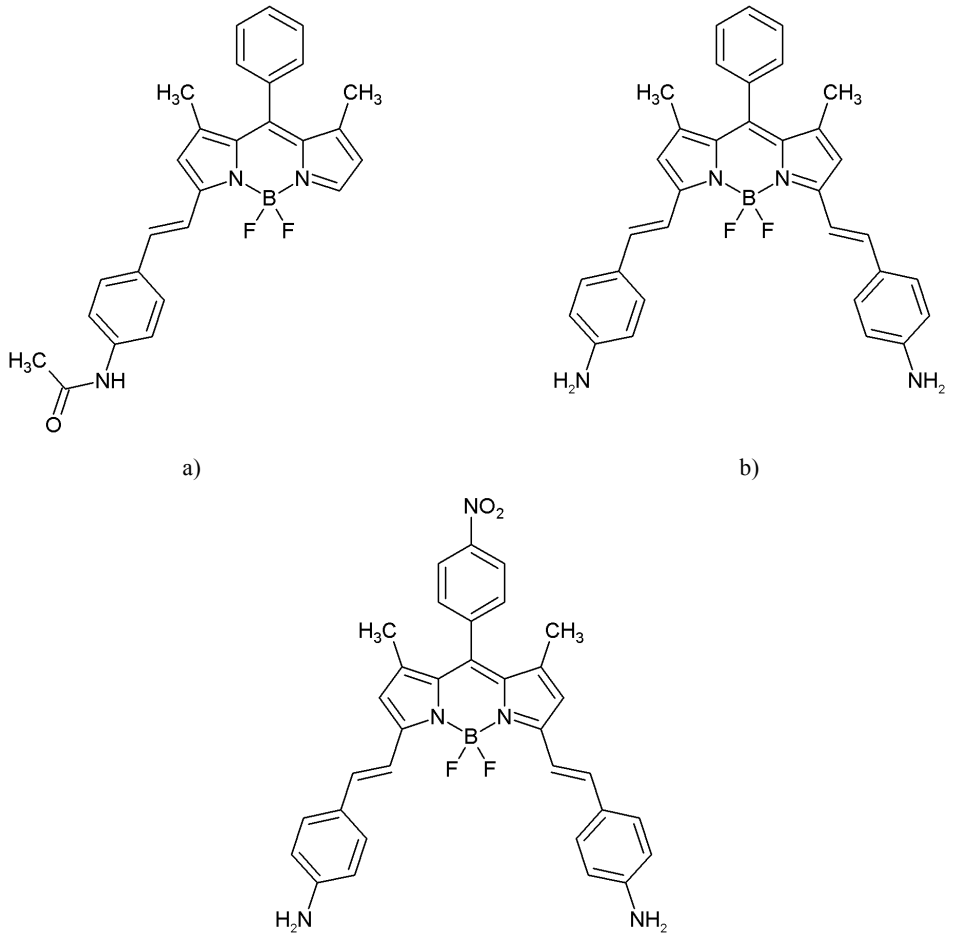

Figure 4.1 Styryl-substituted BODIPYs under investigation. Monoariliden BODIPY (MONO BDP) (a). Biariliden BODIPY (BIS BDP) (b). NO_2-Biariliden BODIPY (NO_2-BIS BDP) (c).

4.2 Mono- and Biariliden BODIPY: Vibronic band analysis

Let's start with the comparison between the BODIPY dyes mono- and di-substituted with styryl units shown in Figure 4.1 a) and b). In order to focus the attention on the effects of the different functionalization, the sets of measurements for each sample are performed in the same solvent. As we can notice, for synthetic reasons the two molecules also differ in the substituent at the end of the styryl moiety, but according to the results provided by the vibrational characterization in Chapter 2 we do not expect any relevant influence due to this further modification. In these sets of measurements we focused on the relaxation dynamics characterizing the vibronic band, which are usually too fast to be detected by the conventional spectroscopic techniques.

4.2.1 Experimental conditions

For each sample, three independent sets of measurements have been acquired in THF solution at 22°C, with the exciting laser pulses centred on the vibronic band of the absorption spectrum of each sample as shown in Figure 4.2.

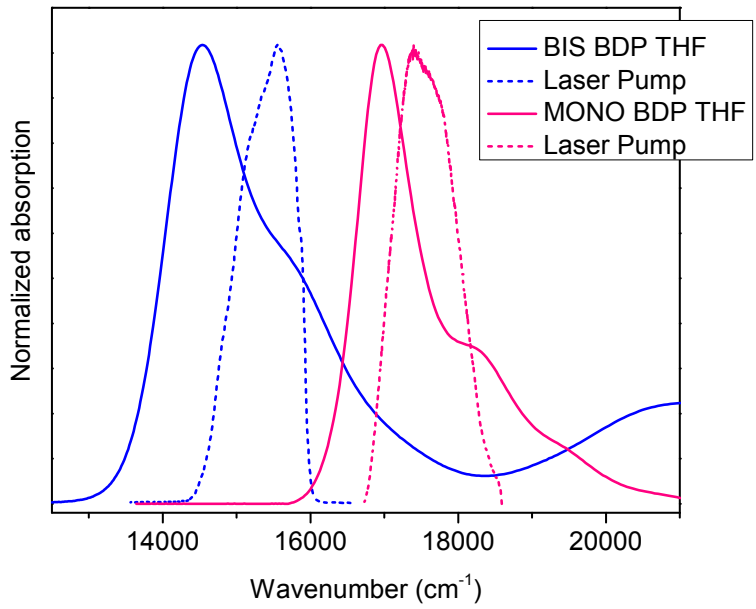

Figure 4.2 Normalized absorption spectra of MONO and BIS BDP in THF compared with the laser pump for each set of measures.

It is evident that the two sets of measurements have been performed under different experimental conditions with the laser pulse covering two distinct spectral regions, because of the different degree of conjugation of the two samples. In addition, we must consider that the laser beam profile changes as function of the exciting spectral region. For this reason the comparison we are going to make should be considered only from the qualitative point of view.

The experimental parameters set up for the three acquisitions for each sample are reported below.

BIS BDP THF	MONO BDP THF
• T scan from 0 to 590 in 5 fs time steps	• T scan from 0 to 800 in 5 fs time steps
• τ scan from -5 to 75 in 0.32 fs time steps	• τ scan from 0 to 40 in 0.4 fs time steps
• Power on sample: 7 nJ	• Power on sample: 7 nJ
• Laser pulse duration: 30 fs	• Laser pulse duration: 15 fs

Only rephasing experiments have been carried on. The analysis has been made on the final 3D-matrix obtained by the average of the three sets of independent measurements. The experimental error affecting the frequencies of the detected signals in the whole 2D-analysis has been estimated as ±60 cm^{-1}. The exciting spectral bandwidth is about 1500 cm^{-1} therefore in the analysis of signal oscillations we will be able to capture beating frequencies <1500 cm^{-1}.

4.2.2 Decay evolution along the population time

As already outlined in Chapter 1, the evolution of the recorded signal as function of the population time provides information about the dynamic processes involving coherences and populations, which are the focus of our study.

We have outlined in Chapters 1 and 3 the difficulty in extracting the real part from the complex data, and the possible artifacts that can derive. Aware of this, as regards the real part of the collected data we will show only the evolution of the 2D maps along T, in order to get a qualitative idea of the main features characterizing the dynamics. It is worthy to remember that the sign of the signals, not possible in the analysis of the always positive absolute data, drives the attribution of the features observed to the Feynman paths contributing to the 2D response (Figure 1.9). Figure 4.3 a) and b) illustrates the real 2D-maps relative to MONO and BIS BDP respectively, representing slices of the averaged 3D-matrix at specified values of T.

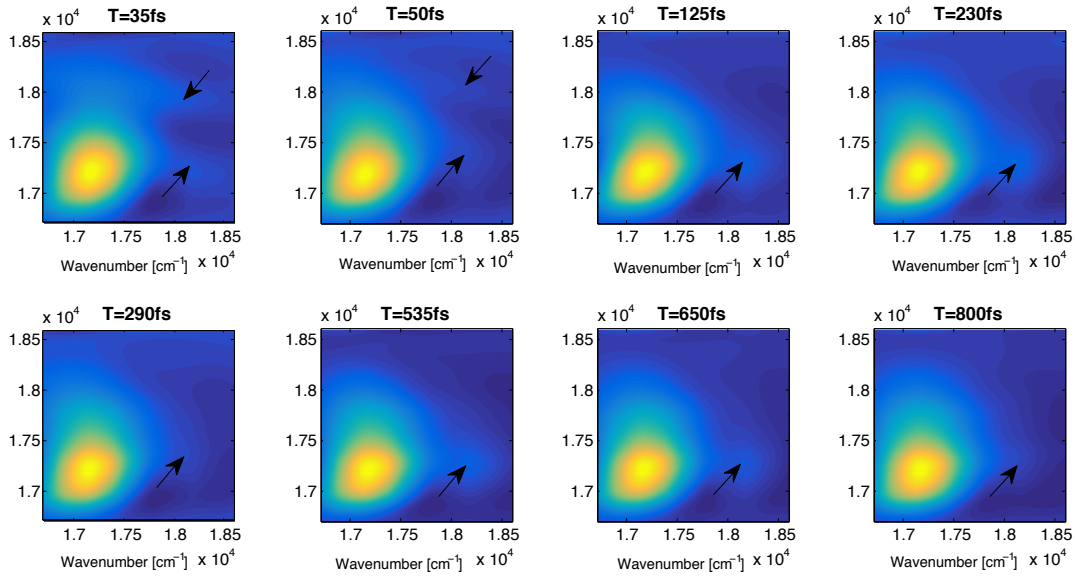

a)

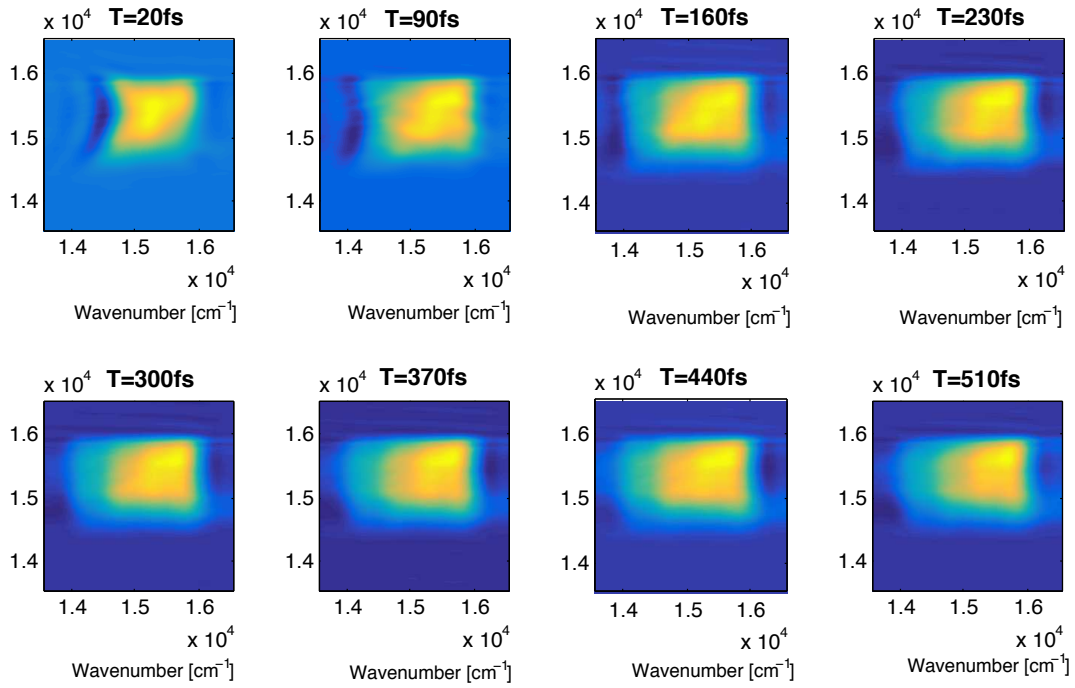

b)

Figure 4.3 2D real maps evolution along T for MONO BDP (a) and BIS BDP (b) in THF. Both x- and y-axes are reported in wavenumber (cm^{-1}).

It can be observed that the 2D maps at selected values of T are very different in the two cases. This is due to the different spectral regions investigated, as well as to the different relaxation dynamics characterizing the two chromophores.

As for MONO BDP, the most interesting feature is the evident presence of an ultrafast relaxation dynamics, represented by the energy shift from the upper to the lower portions of the map after the first 50 fs, and highlighted by arrows pointing the distinctive features. In more detail, at T = 35 fs a diagonal signal in the upper part of the map appears, denoting the

population of an excited vibrational state. In the first 50 fs it rapidly decays to a lower vibrational level indicated by the cross peak highlighted by the arrow. A strongly beating behaviour characterizes the entire evolution, denoting the presence of a coherent dynamics between the underlined states.

The shape of the 2D signal in the real maps of BIS BDP is completely different from the previous case. A very interesting dynamics develops in the first hundred fs: the lower diagonal peak clearly evident at T=20fs disappears almost immediately, leading to the enhancement of the intensity of the upper diagonal region, which persists for the total window investigated. The broadened shape of the signal also includes the cross peaks generated by coherences between vibrational states that we are going to analyse in the following sections. The corresponding absolute maps for MONO and BIS BDP show similar trends, thus are not reported.

In order to better understand the observed behaviour, the molecular states whose energy falls in the available spectral window have to be identified. As explained in detail in Chapter 1, the final signal captured in the 2D maps can be expressed as a convolution between the exciting field and the molecular properties such as the transition dipole moment, which are represented by the absorption spectrum. Therefore, a convenient way to visualize that is represented by the product between the laser beam profile and the absorption spectrum, as shown in Figure 4.4.

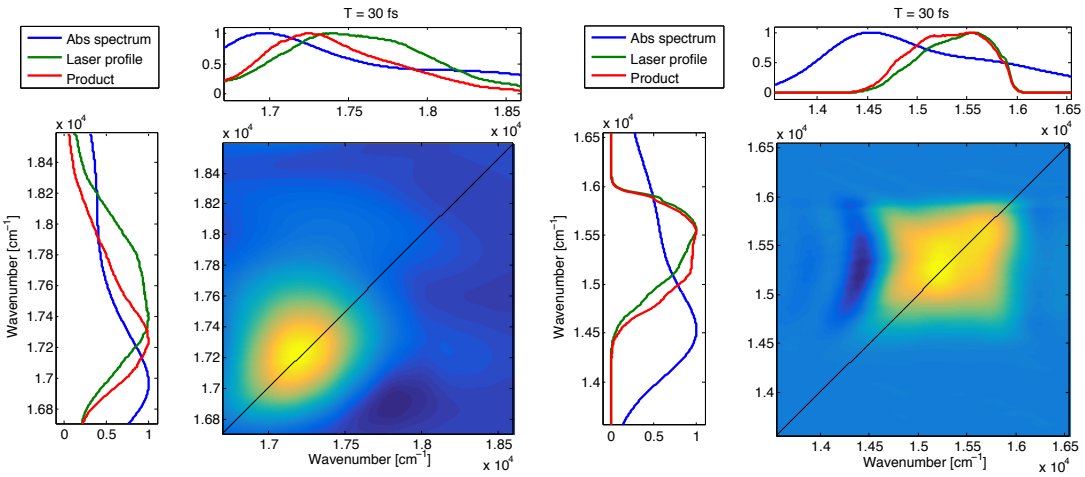

Figure 4.4 Comparison between the collected 2D signal at T=30 fs and the available spectral window for MONO (a) and BIS BDP (b) in THF.

What this picture means is that the energy values detected in the 2D maps for the states involved in the relaxation dynamics under investigation, are strictly correlated to the available spectral window represented by the spectrum obtained as product between the absorption and the laser profile. Particularly, we can detect the ground vibrational level of the first excited electronic state, here also indicated as 1-0, with the maximum of the product

(red spectrum in Figure 4.4). Note that in the case of BIS BDP the upper diagonal peak that shows a higher intensity at increasing values of the delay time T corresponds to the position where the maximum of the red spectrum falls.

We also recall that the features observed in the 2D maps, which correspond to the populations and the coherences we are interested in, are usually affected by the homogeneous and inhomogeneous broadening, as illustrated in Chapter 1. Consequently, we must take into account these phenomena in the assignment of the energy values to the detected signals.

A first indication of the vibrational levels which are directly involved in the exciting spectral region is the vibronic progression provided by the multi-Voigt fit of the absorption spectrum compared with the laser beam profile, shown in Figure 4.5 for both samples. It represents a very useful tool when the laser pump is tuned to cover the higher energy region with respect to the transition from the ground to the 1-0 state in the absorption spectrum. The multi-Voigt fits performed have been driven by the vibrational modes characterized by means of Raman spectroscopy. The Raman spectra recorded for both MONO and BIS BDP and the assignment of the main signals appearing are reported in detail in Chapter 2. Furthermore, these spectra are shown in Section 4.2.4 and quickly discussed for comparison purposes. As we can notice, in the measures performed on MONO BDP the exciting laser pulse overlaps with the two Voigts associated to the vibrational states 580 and 980 cm^{-1} higher in energy with respect to the 1-0, covering also part of that centred at 16980 and 18400 cm^{-1}. In the case of BIS BDP, the laser profile is centred on the Voigt corresponding to the vibrational state at about 930 cm^{-1} from the 1-0.

On the base of the information provided by the multi-Voigt fit, we can build a model level diagram of the main electronic and vibrational states involved in the 2D response of MONO and BIS BDP. We base our models on the reasonable assumption that the molecular structure does not change under excitation, thus the same vibrational modes are active in the ground and excited states.

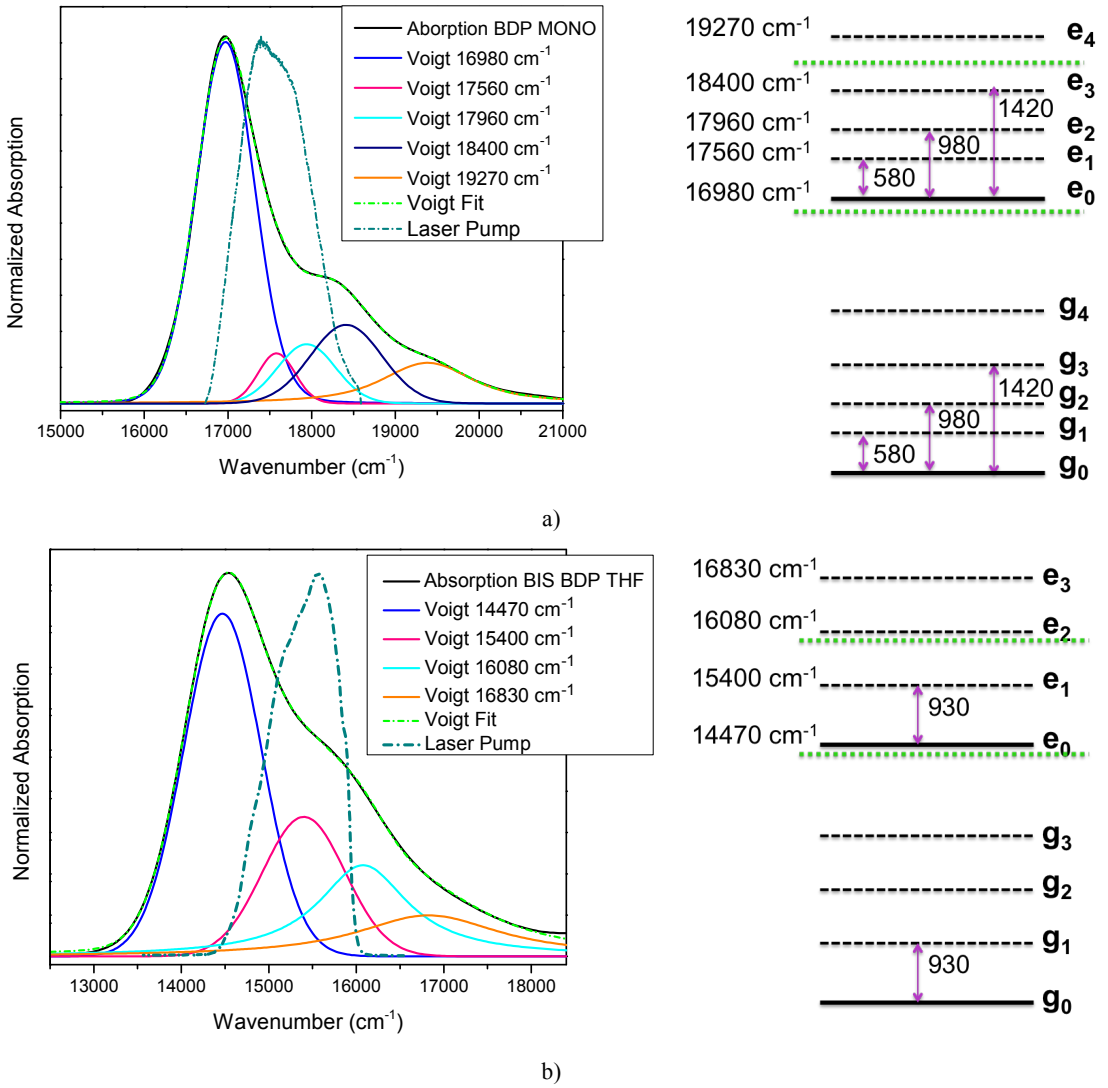

Figure 4.5 Absorption spectra and multi-Voigt fits compared with the laser beam profile (left panel) and model level diagram (right panel) for MONO BDP (a) and BIS BDP (b).

From now on we will refer to the labels used in the model diagrams of Figure 4.5 to indicate all the vibrational levels in the ground and excited states for both chromophores. For example, the 1-0 state will be denoted as $\boldsymbol{e_0}$, and so on for the others.

In the light of this, we can interpret the decay dynamics observed from the evolution of the 2D maps along T in Figure 4.3. As for MONO BDP, we may identify the states e_0 and e_1 with the region where the signal shows its highest intensity. The ultrafast relaxation dynamics characterizing the first 50 fs involves firstly the state e_2, corresponding to the upper diagonal signal, which relaxes to e_1 associated with the lower cross peak. This last manifests a strongly oscillatory character for the whole investigated window. On the base of this consideration, we may expect to find a coherent superposition between e_2 and e_1, and a strongly oscillation at the frequency matching the energy gap between the two states, about 400 cm^{-1}.

In the case of BIS BDP, in the region where the signal has the highest intensity we can identify the diagonal states e_0, e_1 and e_2 and the cross peaks associated to coherences between them.

We are going to verify all the supposed correlations in the following sections.

4.2.3 Beats analysis: kinetics on single points and Fourier maps

In order to study the coherent dynamics that characterizes the investigated samples, we are interested to the beating behaviour of the signal amplitude along the population time, which affects each point of the 2D map. For this reason, a global fit method has been applied to subtract the decay contribution from the overall dynamics, as outlined in Chapter 3. This procedure provides the 3D-matrix of residues on which the following analyses are performed. In order to avoid the artifacts deriving from the global phasing procedure of the complex signal, only the absolute contribution is considered. The global fit applied to the decay dynamics of MONO and BIS BDP has required two different kinetic models: a *geec* model in the first case, composed by a Gaussian function, two exponentials and a constant in the investigated temporal window, and a *geeec* kinetic in the second case.

Owing to the limits of this procedure, frequency values below 200 cm^{-1} are affected by artifacts due to the fit and are not considered as available signals in our analysis.

We are going to discuss the results provided by two procedures, the kinetic and Fourier map analyses, which allow detecting the frequencies associated to the main oscillating components and the positions in the 2D maps where they contribute more, in order to identify the vibrational states involved in the coherent dynamics.

The kinetic analysis has been performed on selected points chosen on the base of what deduced from the previous analysis and according to the positions predicted by the response theory for vibrational coherences (see Chapter 1). Only the most significant results of the total analysis performed are shown.

We start with an example of the kinetic analyses performed on MONO BDP at the position of the lower cross peak between the e_0 and e_1 state in Figure 4.6**.** The residuals reported in the upper central panel and relative to the relaxation dynamics extracted at the specified coordinates, show a multi-frequency oscillatory behaviour. The Fourier Transform along T of the extracted oscillating residuals (lower left panel) gives information about their frequency contributions, whose dynamics is characterized by the time-frequency transform in the lower central and right panels.

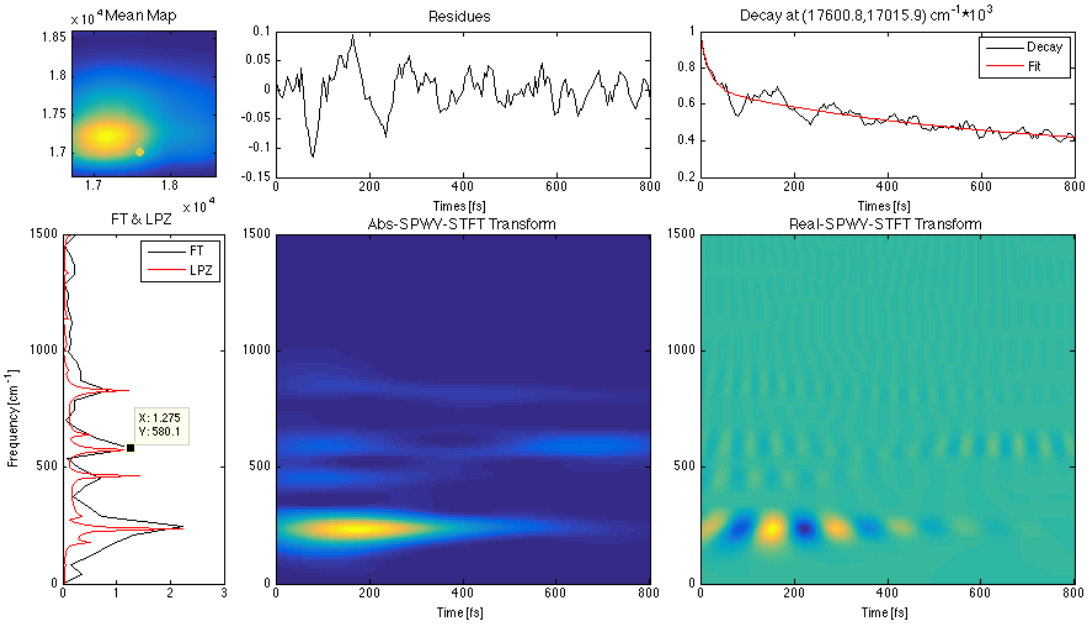

Figure 4.6 Kinetic analysis in the region of the cross peak at (17560,16980)cm^{-1} along T for MONO BDP in THF.

Firstly, an intense signal at 250 cm^{-1} damped in about 400 fs, which also affects many other positions of the map, appears. Furthermore, another relevant contribution at 580 cm^{-1} can be identified, which exactly matches the energy difference between the two investigated states. According to what observed from the decay evolution along T and the results provided by the multi-fit Voigt, it corresponds to a vibrational coherence between e_0 and e_1 and between g_0 and g_1.

The same analysis has been performed on the diagonal region corresponding to the position of the e_1 state, as shown in Figure 4.7.

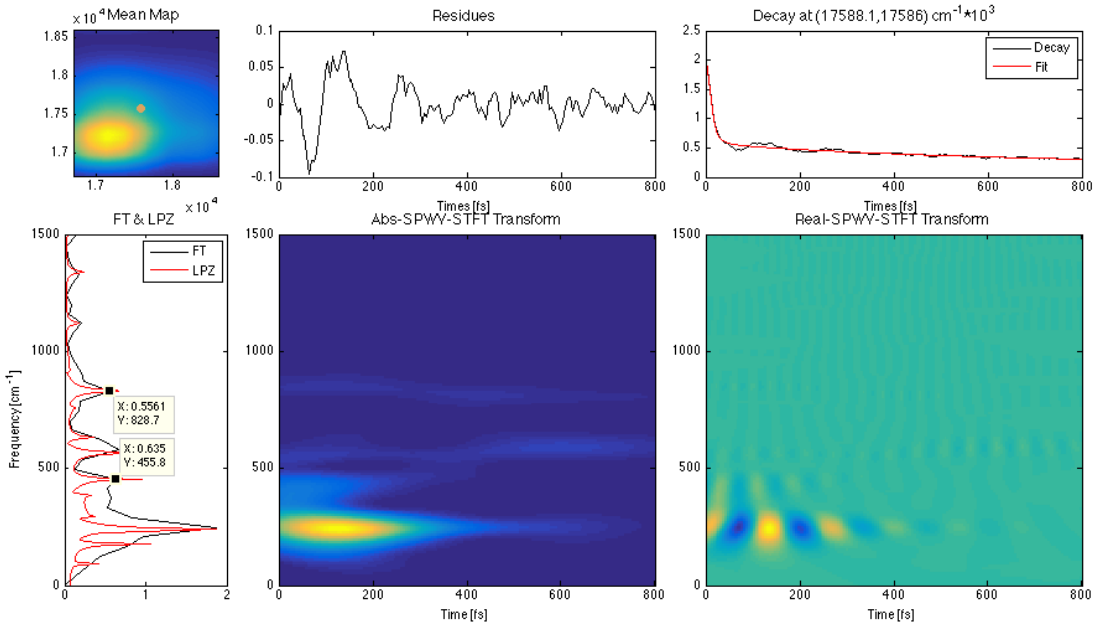

Figure 4.7 Kinetic analysis at the diagonal position (17560,17560)cm^{-1} along T for MONO BDP in THF.

In addition to the already detected 250 and 580 cm^{-1} components, two other main frequencies can be identified: 450 and 830 cm^{-1}. These two frequencies do not correspond to any vibrational mode previously identified. From a look to the multi-Voigt fit, the first contribution is close in energy to the gap between the e_1 and e_2 states, while the second practically corresponds to the energy difference between e_1 and e_3. In order to verify the presence of a correlation between these pairs of states, we report in Figure 4.8 and 4.9 two examples of the kinetic analysis made in these regions.

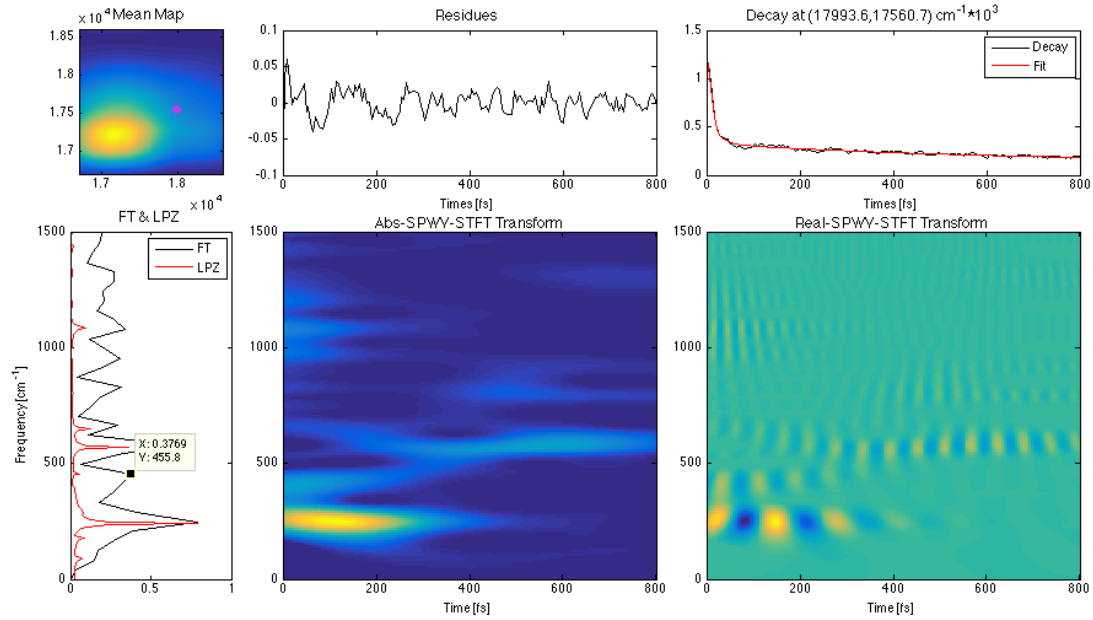

Figure 4.8 Kinetic analysis at the off-diagonal position (17960,17560)cm^{-1} along T for MONO BDP in THF.

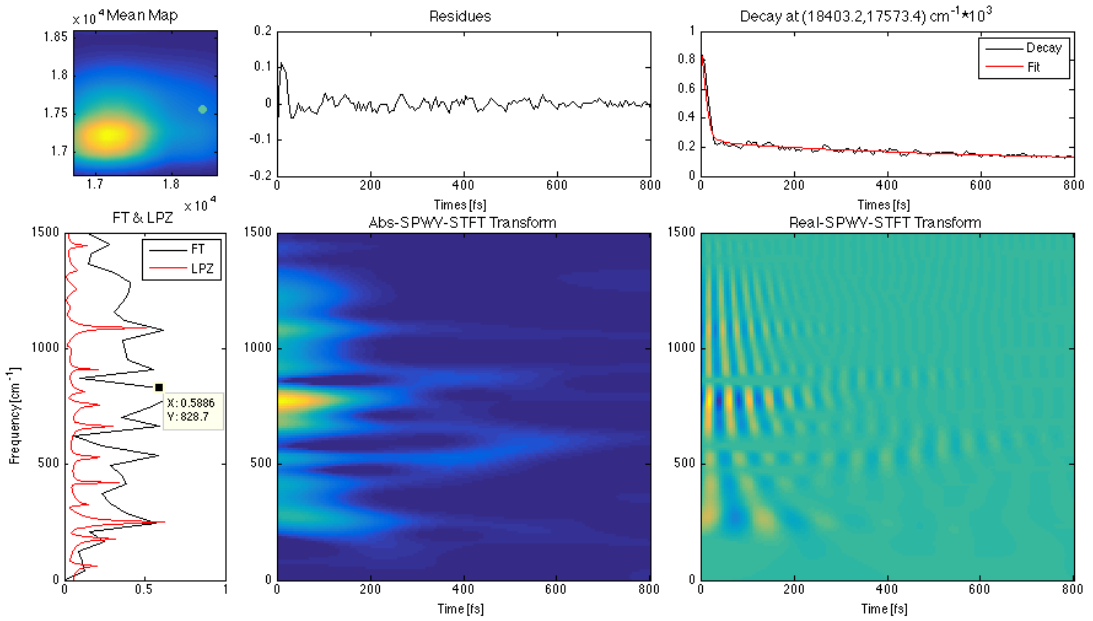

Figure 4.9 Kinetic analysis at the off-diagonal position (18400,17560)cm^{-1} along T for MONO BDP in THF.

The analysis extended to others selected points of the map has confirmed that the positions where these frequencies contribute more correspond exactly to the cross peaks between the states e_1 and e_2 and e_1 and e_3 respectively. Therefore, the presence of a coherence between these pairs of vibronic states can be reasonably deduced.

It is important to stress out that these coherences are different from the ones between e_0 and a higher vibrational level of the excited electronic state. Although there is not an unequivocal way of referring to the different types of coherences in literature, in this work we follow the convention adopted by Mancal in distinguishing firstly the coherences observed in the excited-state manifold from the ones originating in the ground state [107]. In this way, we assign the term 'vibrational' coherences strictly to the ground state contribution, while we refer to the excited state coherences deriving from the strong coupling of vibrational modes with the electronic transition as 'vibronic' coherences. Furthermore, in our case two different types of coherences arising from the excited states are detected for MONO BDP. Therefore, we denote with vibronic coherences of type Ⅰ the ones involving the e_0 state and a higher vibrational level, whereas the coherent superpositions of vibrational excited states are referred as vibronic coherences of type II.

The two types of vibronic coherences are also characterized by different dynamics: we expect to find a shorter-living character for that of type II owing to the nature of the states involved. In addition, the positions of the 2D map where they contribute are different, thus the deriving patterns predicted by the response theory can be distinguished in the two cases. It has been verified that vibronic coherences of type II give rise to symmetric signals above and below the diagonal, as the ones characterizing electronic coherences. On the other hand, vibronic coherences of type I generate signals contributing to the *chair-like symmetry* (see Chapter 1).

The kinetic analysis on the upper diagonal region, where we can expect mainly to find oscillations arising from the excited state manifold, has provided an interesting result. A very intense oscillation at about 950 cm^{-1} predominates at the cross peak position between e_0 and e_2, as shown in the kinetic analysis at the corresponding coordinates illustrated in Figure 4.10.

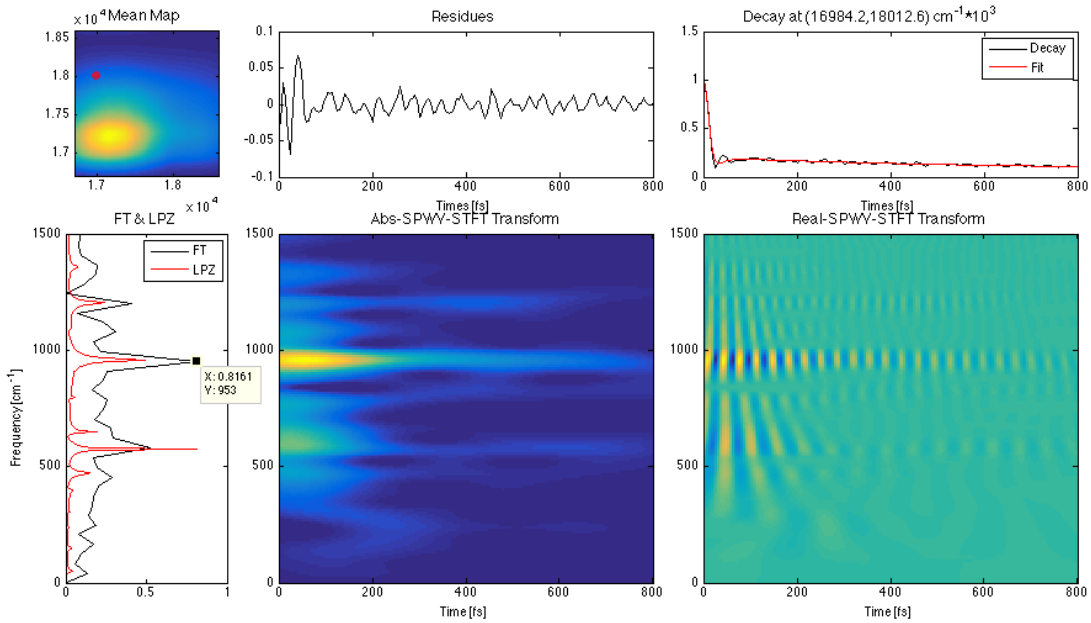

Figure 4.10 Kinetic analysis in the region of the cross peak position (16980,17960)cm^{-1} along T for MONO BDP in THF.

A first look to the residues in the central upper panel reveals a strong oscillating character. In addition, the SPWV-STFT plots suggest a long-lasting nature since the signal persists for the whole spectral window investigated. We can identify this component with a vibronic coherence of type I oscillating at the frequency corresponding to the energy gap between the involved states e_0 and e_2, and with the corresponding ground state vibrational coherence between g_0 and g_2.

A more direct visualization of the coherences between vibrational, vibronic or electronic states of a certain system is provided by the *Fourier maps* at the specified frequencies, described in detail in Chapter 3. The signals detected in these 2D frequency maps indeed oscillate at the frequency which gives rise to the coherent coupling of the corresponding states. For example, the Fourier map relative to the 950 cm^{-1} component in Figure 4.11 shows a diagonal signal corresponding in the available spectral region to the energy of the e_0 state, and two symmetric cross peaks on the dashed lines indicating all points of the map at a distance from the diagonal equal to the selected frequency. We know from the response theory that the diagonal position corresponding to the population of the higher vibrational state involved in the coherent superposition does not beat and cannot be detected [35]. The features observed in the Fourier map below correspond to a 'half' *chair symmetry* because only a portion of the pattern typical of vibrational coherences is detected. The two additional signals expected at lower energies cannot be measured because they fall outside the bandwidth limits [34]. A very interesting feature emerges from the relative intensity of the three signals: the upper cross peak is more enhanced compared to the others in spite of its

excited state nature. This result is in agreement with what observed from the kinetic analysis performed in the upper diagonal region. On the contrary, we would expect a higher intensity on the lower diagonal portion of the map, where the longer-lasting ground state vibrations should contribute more.

The unexpected behaviour of this component suggests the possible presence of more than one mechanism contributing. The comparison with data obtained for different dyes on the same solvent [108] suggests the possible involvement of a solvent mode at 950 cm^{-1}, resonant with a vibrational mode of the molecule. The role of the solvent will be further investigated in sections 4.3 and 4.4.

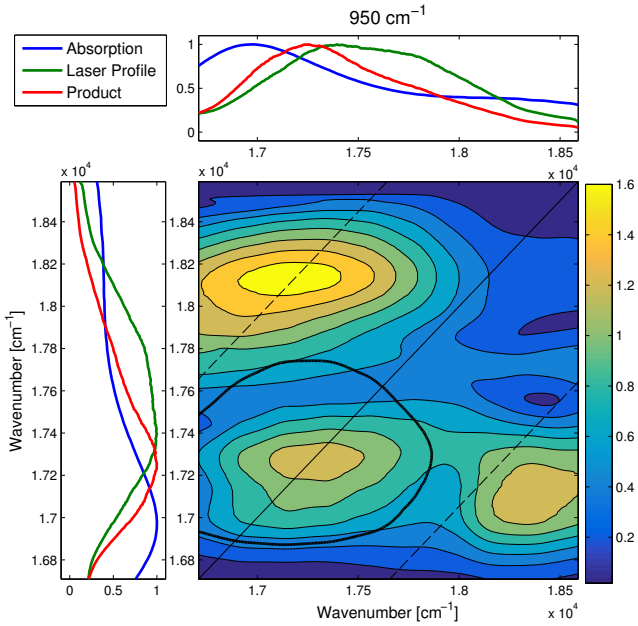

Figure 4.11 Fourier map of MONO BDP in THF at 950 cm^{-1}.

The most significant result of the kinetic analysis performed on selected points in the case of BIS BDP is represented by the presence of the same 950 cm^{-1} mode, which in this case predominates in the lower diagonal region, as shown in Figure 4.12. Particularly, the position at which it contributes more is compatible with that of the lower cross peak between the e_0 state identified by the maximum of the product between the laser pump and the absorption spectrum, and the excited vibrational level 950 cm^{-1} higher in energy. Therefore, this oscillation is identified again with a vibrational coherence between g_0 and g_1 and the corresponding vibronic coherence of type I between e_0 and e_1. In this case it is more difficult to distinguish the symmetric contribution in the upper diagonal region owing to the presence of spurious signals arising at the bandwidth limits.

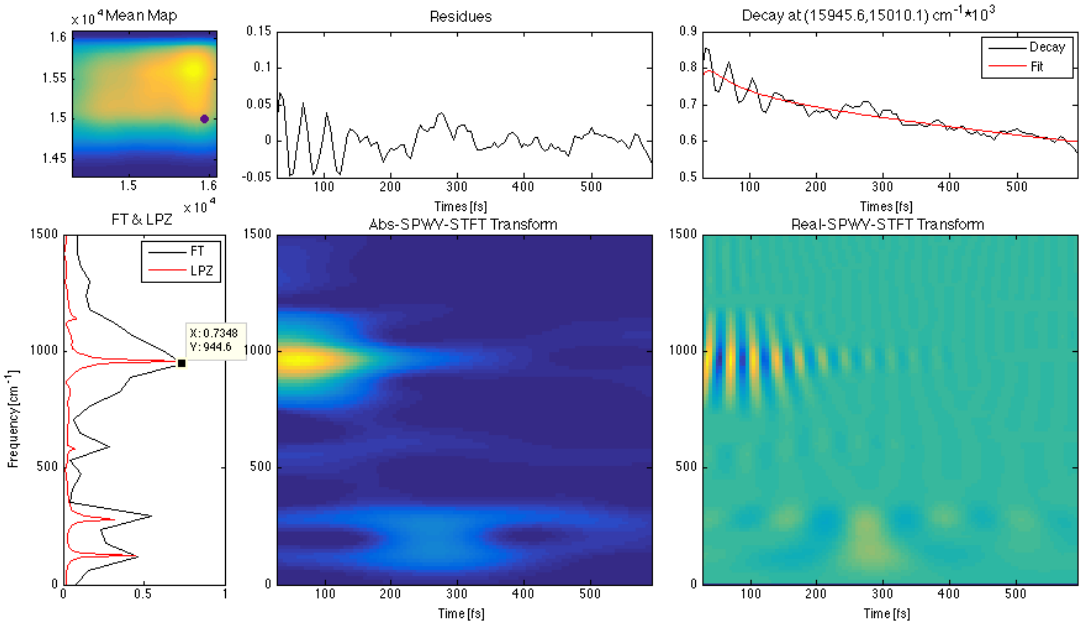

Figure 4.12 Kinetic analysis of 950 cm^{-1} beating component in BIS BDP. The investigated point has been selected in the available spectral region provided by the product between the absorption spectrum and the laser pump.

The TFT analysis in Figure 4.12 shows a very different dynamics compared to that of the same oscillation in MONO BDP, since in this case the 950 cm^{-1} mode is damped in about 100 fs. The relative Fourier map shown in Figure 4.13 presents two symmetrical signals on the dashed lines at a distance of 950 cm^{-1} from the diagonal, with the lower cross-peak characterized by higher intensity in agreement with the kinetic analysis. The signal outside the bandwidth limits represents a spurious signal and is not considered. The feature in the upper diagonal part can be associated to the higher cross peak between the e_0 and the e_1 state. Also in this case the observed pattern can be identified with the half *chair symmetry*, except for the only partially detected diagonal signal.

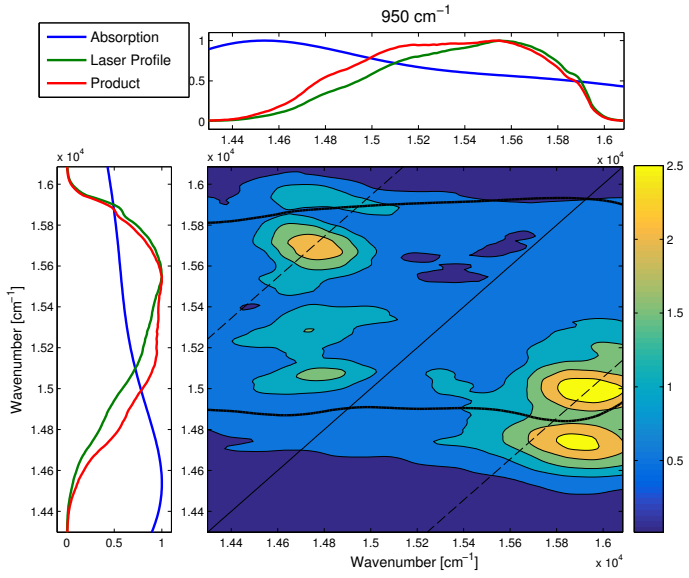

Figure 4.13 Fourier map at 950 cm^{-1} for BIS BDP.

Fourier maps relative to other relevant frequencies are affected by artifacts arising from the overlap of signals due to the limited frequency resolution. They do not provide additional information and are not shown.

4.2.4 Overall beats analysis: Fourier spectrum of coherences

The Fourier spectra of coherences (FSC), obtained from the 2D data relative to MONO and BIS BDP, are compared in Figure 4.14 a). They provide information about the frequencies contributing to the overall beating pattern, obtained by the integration along the excitation and emission coordinates. The comparison with non-resonant Raman spectra is also reported in Figure 4.14 b).

While the non-resonant Raman spectrum carries information on the frequencies of the ground state vibrational modes, the FSC potentially provide a great quantity of additional information:

I. The relative intensities of the FSC signals tell about the strength of the coupling with the electronic transition.
II. The bandwidth carries information about the dynamics, i.e. if we are dealing with short-living or long-lasting coherences.
III. Signals that do not correspond to the vibrational modes characterizing the Raman can be identified as vibrations that only contribute in the excited state.
IV. In the case of multi-chromophoric systems, frequency deriving from the superposition of electronic states can also be detected.

On the base of the nature of the studied samples, we are only interested to the first three types of information.

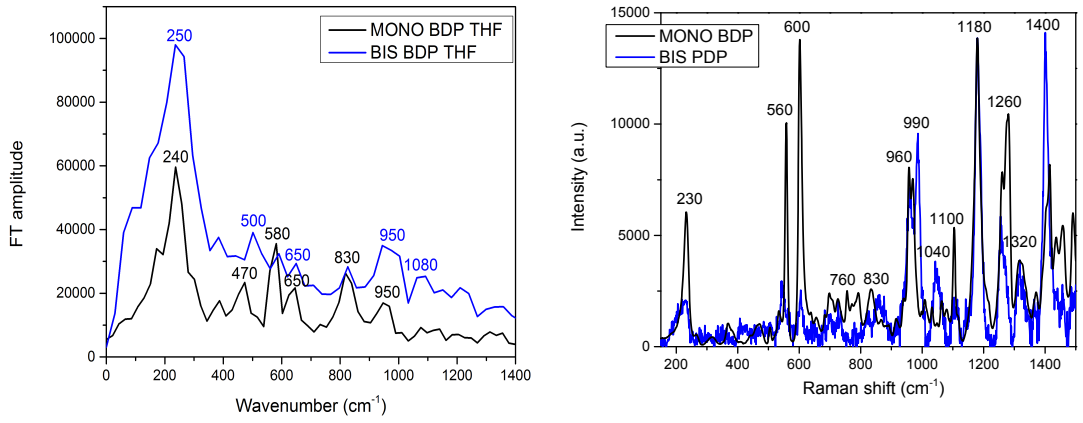

a) b)

Figure 4.14 Overlap between the FSC relative to MONO and BIS BDP in THF (a) and their Raman spectra (b).

A detailed comparison between the main components of the FSC spectra and their corresponding Raman modes is reported in Table 4.1. For a meaningful comparison it should be kept in mind that the frequency resolution attainable in our 2D setup is 60 cm^{-1}.

Table 4.1 Comparison between the main signals of FSC with the Raman modes for BIS and MONO BDP in THF. Data reported in cm^{-1}.

MONO BDP THF		BIS BDP THF	
FCS (±60cm^{-1})	Raman	FCS (±60cm^{-1})	Raman
240	230	250	230
470			
580	560	500	540
650	600	650	600
830	830	830	860
950	960	950	960

The frequencies highlighted correspond to the detected vibrational and vibronic coherences of type I (green) and to the vibronic coherences of type II (cyan).

The 250 cm^{-1} mode appears the more intense in both the FSC spectra, indicating that it is the predominant component of the 2D-map. This result matches that found from the detailed kinetic analyses performed on several points of the 2D map.

In the case of BIS BDP, the main components of the FSC spectrum are in good agreement with the ground state modes characterized by the Raman, while there are some interesting discrepancies for the mono-substituted sample:

(I) The weak signal at 470 cm^{-1} in the FSC is also totally absent in the Raman, meaning that it is relevant only at short times, as confirmed by TFT analysis in Figure 4.8. This confirms that it may correspond to a superposition between the e_1 and e_2 states.

(II) The intense signal at 830 cm^{-1} in the FSC may correspond to the weak mode at 830 cm^{-1} in the Raman, but also to the coherent superposition of the vibronic states e_1 and e_3. The two contributions are very close in energy and are not distinguishable in our experimental resolution. The resultant 2D signal is a mixture of them and gives rise to very complex pattern in the corresponding Fourier map (not shown).

(III) The intense 580 cm^{-1} component in the FSC of MONO BDP can be identified with the intense vibrational mode at 560 cm^{-1} in the Raman and thus corresponds to the vibronic coherence of type I between the e_0 and e_1 states and to the vibrational coherence between g_0 and g_1.

The signals at 950 cm^{-1} in the FSC spectra of both samples, which correspond to the 960cm^{-1} vibrational mode in the Raman spectra of both species, are identified with the vibronic

coherence of type I previously discussed between the e_0 and e_2 states or with the vibrational coherence between g_0 and g_2. Particularly, we can notice that the relative band in the FSC spectrum of BIS BDP covers a larger interval of frequencies than the corresponding in MONO BDP. This result is in accordance with what observed about their different dynamics since, according to the indetermination principle, frequencies characterized by very short damping time are affected by big uncertainty in the frequency domain.

A closer look to Figure 4.14 highlights the presence of additional modes at 990 and 1040 cm^{-1} in the Raman of BIS BDP not present in the Raman of MONO BDP. These modes are not fully recognizable in the FSC spectrum since they are probably included in the bandwidth of the band centred at 950 cm^{-1} and of its weaker shoulder at 1080 cm^{-1}.

The comparison between the Raman modes and the 2D signals is not extended to frequencies higher than 1200 cm^{-1} since they are at the limits of the frequency resolution in the 2D spectra.

4.2.5 Concluding remarks

The results obtained from the previous analyses are schematically summarized in the model level diagrams for MONO and BIS BDP reported in Figure 4.15.

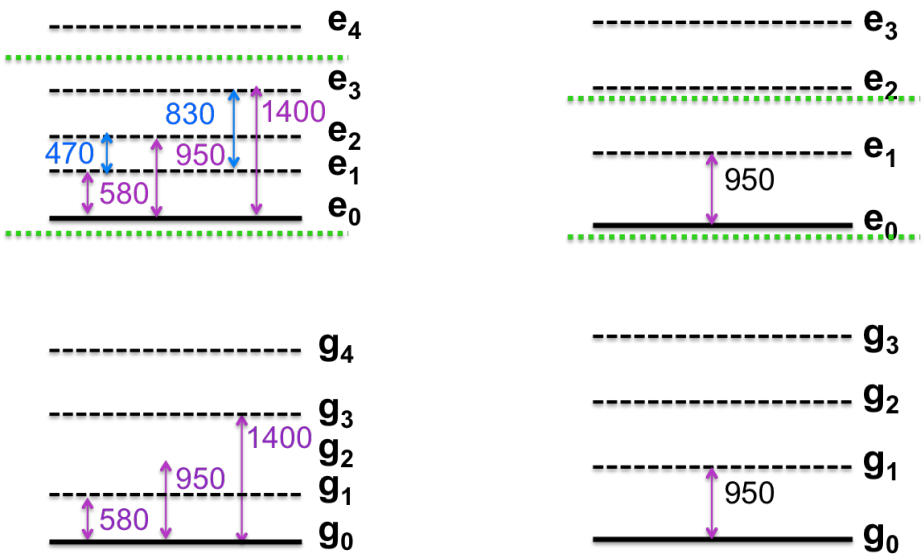

Figure 4.15 Model level diagram for MONO (a) and BIS BDP (b) in THF reflecting the results obtained from the 2D response and the Raman. All energies reported are in cm^{-1}. Vibrational and vibronic coherences of type I are marked in magenta; vibronic coherences of type II in blue. The green lines enclose the states addressed by the laser pulse.

The comparison between the MONO and BIS BDP has led to the evidence that the dynamics of these samples is modulated through the coupling with two common vibrational

frequencies, 250 cm^{-1} and 950 cm^{-1}. While the former affects mostly the whole beating pattern of both chromophores, the latter predominates in different positions of the 2D maps of the two samples. In the case of MONO BDP this higher frequency shows an intense beating behaviour in the upper diagonal region, where only excited state contributes. Here it also appears as a long-lasting vibrational coherence that persists in the whole investigated window. For this reason, we take under consideration the hypothesis that THF contributes with its 960 cm^{-1} vibrational mode to enhance the same frequency characterizing the vibrational structure of the sample, through some kind of coupling. The understanding of the nature of this effect, which may be a trivial sum or something of more interesting, is the aim of the following section.

The analysis on the vibronic band of MONO BDP has also provided the evidence of another vibrational coherence of type I at 580 cm^{-1}, and of two vibronic coherences of type II at 470 and 830 cm^{-1} corresponding to the superpositions between the vibronic excited states matching these energy gaps.

Two evidences emerged from the comparison of the two samples and could be associated to the different degree of conjugation and/or branching. The first regards the relative intensity of the signals detected in the respective FSC spectra: the spectrum of MONO BDP is characterized by a more equal distribution of intensities than that of the di-substituted dye, in which the component at 250 cm^{-1} clearly predominates over the others. This trend can be connected to the different degree of ramification of the two chromophores, in the sense that the two styryl moieties in BIS BDP may be involved in some kind of coordinated motion which hinds the contribution of the higher frequencies in the modulation of the dynamic of this chromophore. For the same reason, the oscillation at 950 cm^{-1} may be damped in a relative short time of about 100 fs, differently from the same frequency in MONO BDP, which persists for the entire spectral window although contributing more in the excited state.

This behaviour is in full agreement with the results already obtained in Raman analysis (Section 2.4), showing that in the BIS BDP the low frequency modes in the range 400-800 cm^{-1} were suppressed. Here, thanks to higher content of information of 2D spectroscopy both in frequency and in time domain, it has been possible also to propose a possible interpretation.

We have seen that the exploration of the vibronic band of the absorption spectrum can lead to a very complex data analysis because in this spectral region vibrational and vibronic contributions in the ground and excited states may both contribute and overlap. In order to simplify the study of the vibrational coherences in the ground and the vibronic coherences of

type I in the first excited state, we focused in the following sets of measurements on the lower energy side of the absorption spectrum.

4.3 Biariliden Bodipy: 0-0 band analysis. The solvent effect

With the aim of investigating the solvent role on the relaxation dynamics mainly involving the ground state, the following measures have been acquired with the exciting laser pulse tuned so to overlap with the red hand side of the 0-0 band of the absorption spectrum of BIS BDP (Figure 4.1 b)) in two different solvents. The selection of the di-substituted dye has been made in order to obtain a more complete view not emerging from the previous analysis. The analyses on the two solutions have been performed working under the same experimental conditions, particularly keeping constant the laser beam profile, in order to facilitate the comparison.

4.3.1 Experimental conditions

The following analyses have been performed on two different solutions: BIS BDP in THF and in MeOH. Three sets of measures have been acquired for each solution at 22°C, with the laser pump covering the lower energy portion of their absorption spectra, as shown in Figure 4.16.

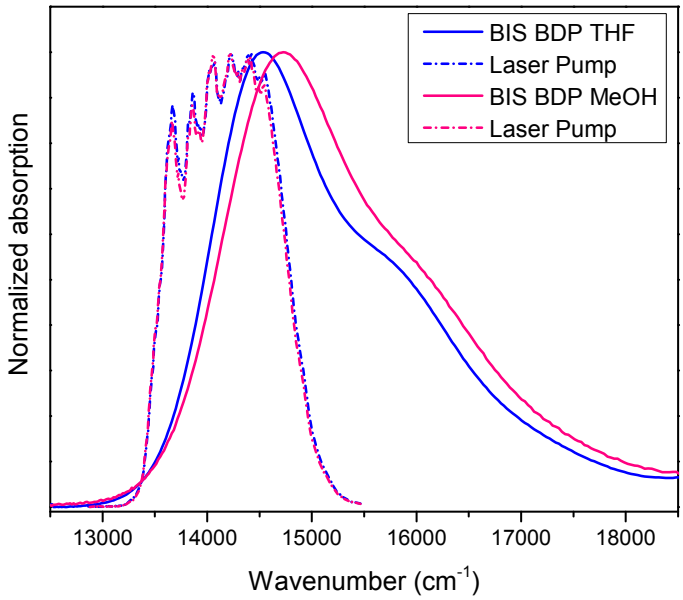

Figure 4.16 Overlap of the absorption spectra of BIS BDP in THF and MeOH compared with the laser pump for each set of measures.

The experimental parameters are:

BIS BDP THF

- T scan from 0 to 800 in 5 fs time steps
- τ scan from 0 to 50 in 0.4 fs time steps
- Power on sample: 10 nJ
- Laser pulse duration: 15 fs

BIS BDP MeOH

- T scan from 0 to 800 in 5 fs time steps
- τ scan from 0 to 50 in 0.4 fs time steps
- Power on sample: 10 nJ
- Laser pulse duration: 15 fs

The data analysis has been conducted on the final 3D-matrix calculated for each case as the average of the three sets of measurements. Only the rephasing contribution has been considered.

4.3.2 Decay evolution along the population time

Figure 4.17 shows the comparison of the 2D real map relative to BIS BDP in THF at 30fs and the spectral range of the recorded signal calculated as product between the exciting beam profile and the absorption spectrum.

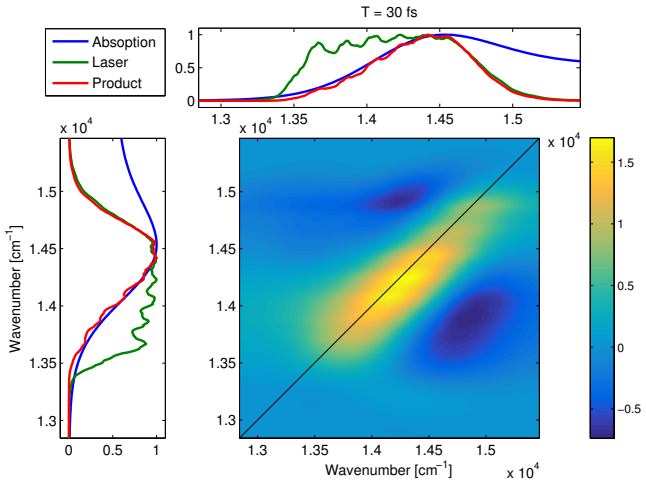

Figure 4.17 2D real map at T=30 fs for BIS BDP in THF compared with the available spectral window.

A diagonally elongated central signal, compatible with the position of the maximum of the product between the absorption and the laser spectra, is what firstly appears. In addition, two very pronounced negative signals in the symmetric upper and lower diagonal regions are detected. According to the nonlinear response theory discussed in Chapter 1, they are clear evidences of excited state absorption (ESA) towards higher energy states in the UV.

Figure 4.18 shows the evolution of the real maps of BIS BDP in THF at the specified values of the population times between 0 and 800 fs.

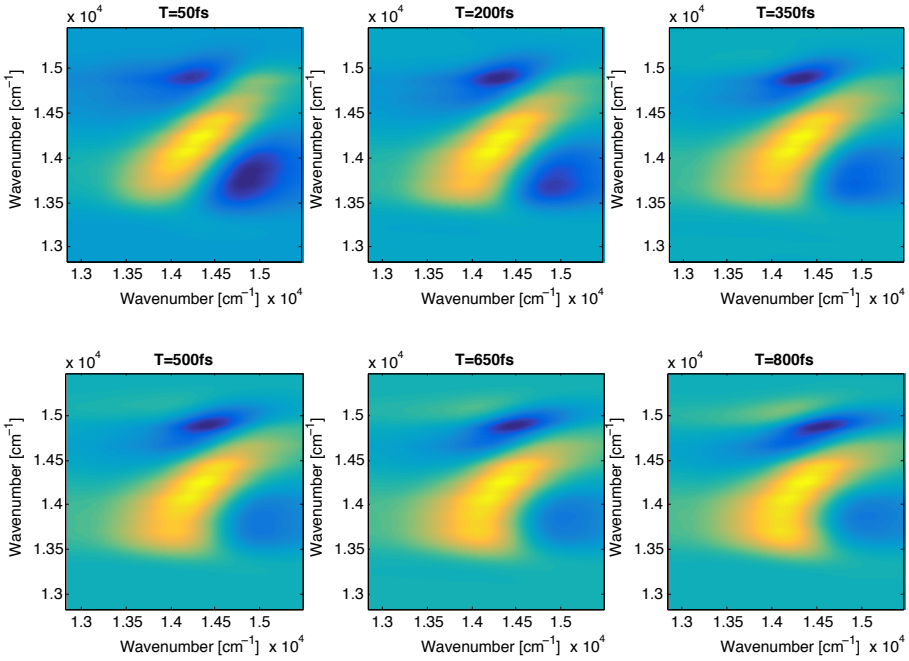

Figure 4.18 2D real maps evolution along T between 0 and 800 fs for BIS BDP in THF.

The most interesting feature in this evolution is that the negative peak below diagonal progressively looses intensity at increasing values of the delay time T. This is mainly due to the growing of a positive cross peak in the same spectral region, which compensates the negative ESA signal. This behaviour can be associated with an energy relaxation dynamics from the upper to the lower region of the map [34].

The decay dynamics of the absolute part of the signal recorded for BIS BDP in THF is illustrated by the 2D maps reported in Figure 4.19.

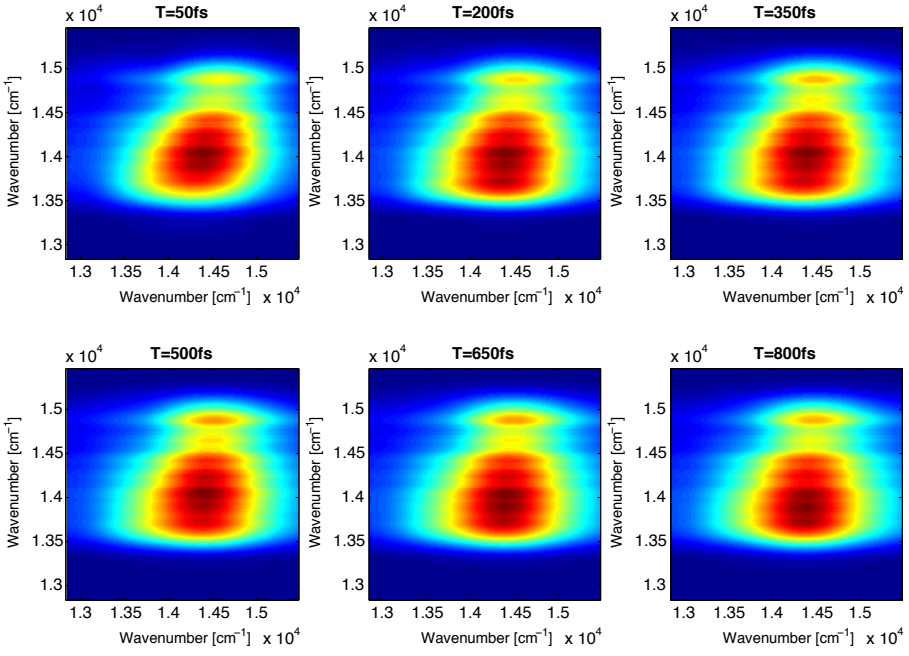

Figure 4.19 2D absolute maps evolution along T between 0 and 800 fs for BIS BDP in THF.

In order to highlight the strong beating behaviour in the lower region of the recorded signal a different colour scale has been used. A small oscillating feature also appears in the upper portion of the map. Note that the signal modulation along the y axis is affected by the particular profile of the laser pump in the investigated spectral region shown in Figure 4.17.

The dynamic evolution of real and absolute 2D response of the same molecule in solution of MeOH does not show any significant differences from that in THF illustrated above, indicating that the solvent does not affect the decay dynamics, at least in the investigated time window.

4.3.3 Beats analysis: kinetic on single points

The same kinetic analysis outlined in Section 4.2.3 has been applied also to these data.

In exploring the 0-0 band we are particularly interested in the lower diagonal part of the map, where the vibrational coherences of the ground state should be clearly characterized. The analysis of this particular spectral region, where the responses are simplified, allowed a better understanding of the solvent influence on the coherent relaxation dynamics of the chromophores.

Figure 4.20 shows the comparison between the results in the two solvents, obtained analysing the dynamics at a specifically selected point in the lower region of the map.

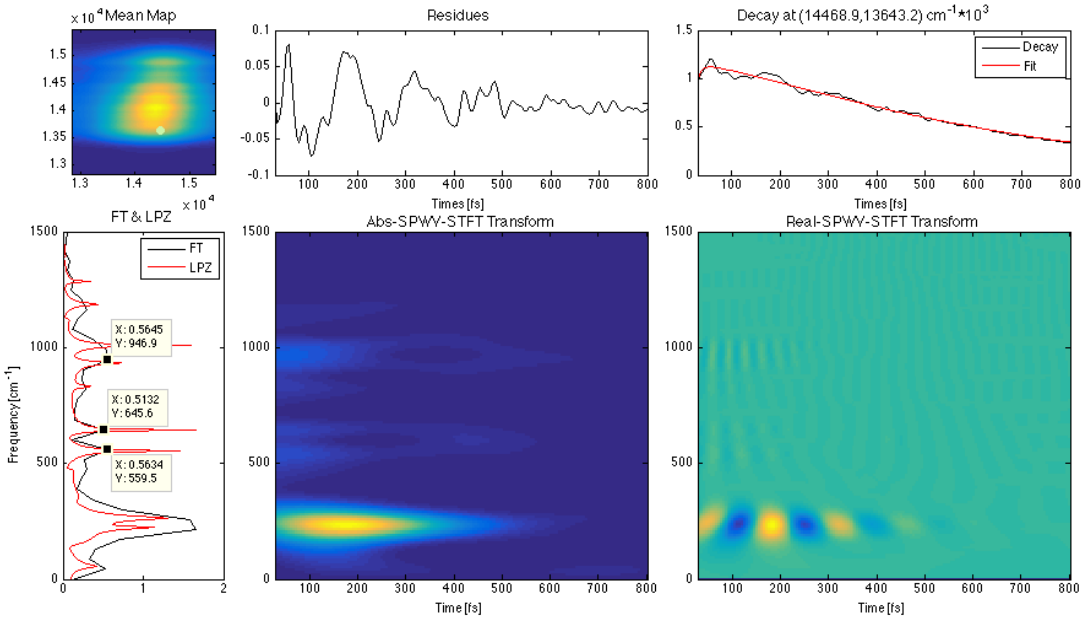

a)

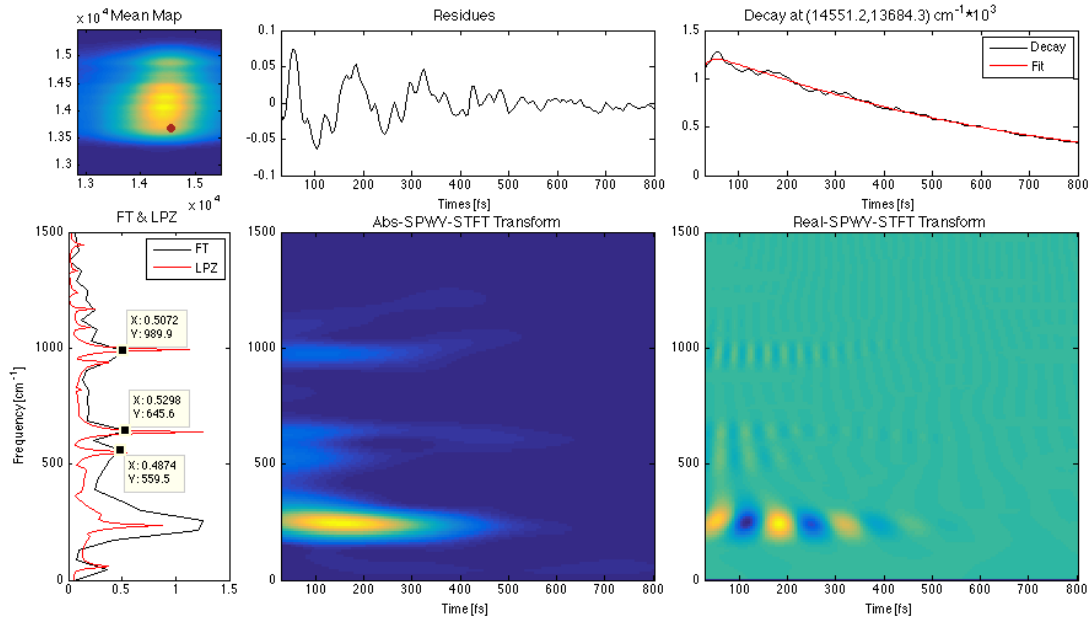

b)

Figure 4.20 Kinetic analysis on the lower diagonal region of the map for the THF (a) and MeOH (b) solutions.

The Fourier transform and the TFT plots highlight in both the solutions an intense oscillation at around 230 cm^{-1}, which mostly affects the whole map, and other three higher frequency components at about 560, 650 and 950 cm^{-1}. At a first look, the vibrational modes at 560 and 650 cm^{-1} have practically the same behaviour in the two solutions. On the other hand, a small but distinguishable energy shift of about 60 cm^{-1} characterizes the signals in the range between 900 and 1000 cm^{-1}: in THF solution we record a maximum at 950 cm^{-1} whereas in MeOH solutions at about 990 cm^{-1}. This is the same region where the previous set of data suggested the possible presence of solvent contribution.

A close look to the dynamics of the four main detected vibrations reveals a very unexpected feature: as we can see from the time-frequency transform, they are all damped in the first hundred fs in both solutions. However, we can expect that, as modes mainly arising from the ground state, they would appear as long-lasting coherences, which persists for the whole window investigated with lifetimes of a few picoseconds [25]. This behaviour can be explained invoking the probable presence of couplings with other degrees of freedom (solvent, for example) that damp these modes quickly.

One of the main advantages of ultrafast spectroscopy is the possibility of determining the damping time of vibrational coherences, which cannot be provided by conventional techniques. We have already seen that the time-frequency transforms set up in our group provide a first idea of the dynamics of the detected beating components. However, it is possible to obtain a more accurate estimate of the damping time performing a fit with a damped exponential function. We are particularly interested in studying the dynamics of the frequencies in the lower portion of the map, where ground state contributes more. In our case this procedure can be applied to estimate the damping time of the lower frequency at about 230 cm^{-1}, which is the main contribution to the residuals reported in the central panels of Figure 4.20. The fitting of the oscillating residuals shown in Figure 4.20 has been performed with an exponentially damped cosine function. The resulted damping time for both the solutions is of 360 fs, confirming the evidence that solvent does not affect the dynamic of the detected vibrational coherences. The result of the fit with the analytical expression of the model used is reported in Figure 4.21.

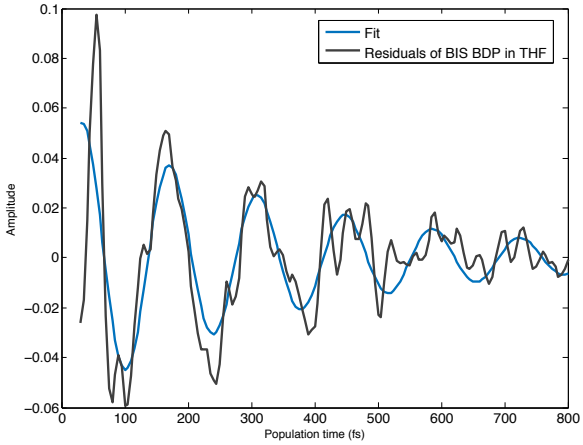

Fit Model

$$y(t) = \cos(2\pi\omega t + \phi) * A * \exp\left(-\frac{t}{t_{damp}}\right)$$

Figure 4.21 Damping time determination for the 230 cm^{-1} component.

4.3.4 Overall beats analysis: Fourier spectrum of coherences

Now we are going to analyse the oscillating components deriving from the Fourier transform of the signal integrated along the excitation and the emission coordinates. The overlap between the FSC spectra relative to the two solutions is shown in Figure 4.22 a) and compared with the experimental non-resonant Raman spectrum of BIS BDP again reported in Figure 4.22 b). Table 4.2 provides a schematic view of the comparison.

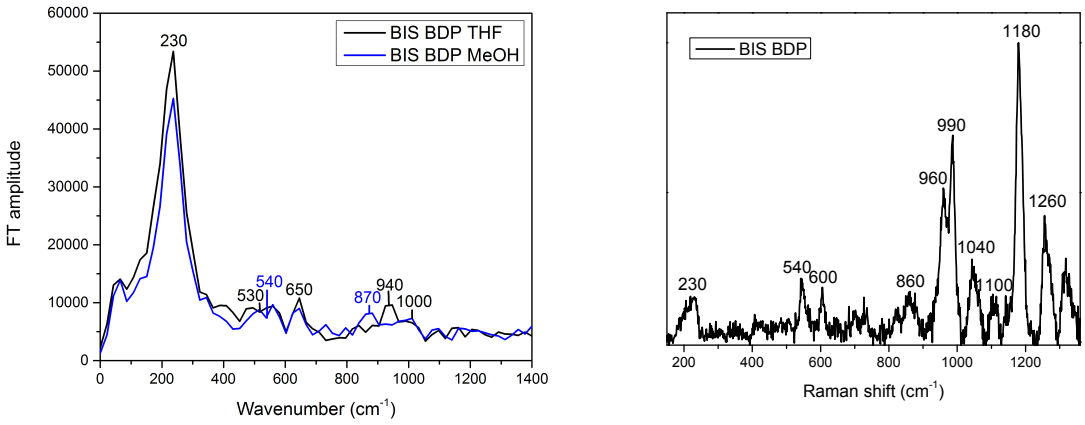

a) b)

Figure 4.22 Overlap between the FSC spectra relative to BIS BDP in the THF and MeOH solutions (a). Raman spectrum of BIS BDP (b).

Table 4.2 Comparison between the main signals of the FSC spectra relative to the THF and MeOH solutions and the Raman modes.

FSC BIS BDP THF (±60cm^{-1})	FSC BIS BDP MeOH (±60cm^{-1})	Raman BIS BDP
230 cm^{-1}	230 cm^{-1}	230 cm^{-1}
530 cm^{-1}	540 cm^{-1}	540 cm^{-1}
650 cm^{-1}	650 cm^{-1}	600 cm^{-1}
	870 cm^{-1}	860 cm^{-1}
940 cm^{-1}		960 cm^{-1}
	1000 cm^{-1}	990 cm^{-1}

There is an overall good agreement between the FSC spectra and the experimental Raman. Therefore, all the main signals appearing in the FSC can be associated to the ground state vibrational modes characterizing the Raman. There is also a perfect correspondence with the frequencies identified in the single points kinetic analysis.

4.3.5 Beats analysis: Fourier Maps

The absolute Fourier maps for the THF solution relative to selected relevant frequencies detected in the FSC are reported below.

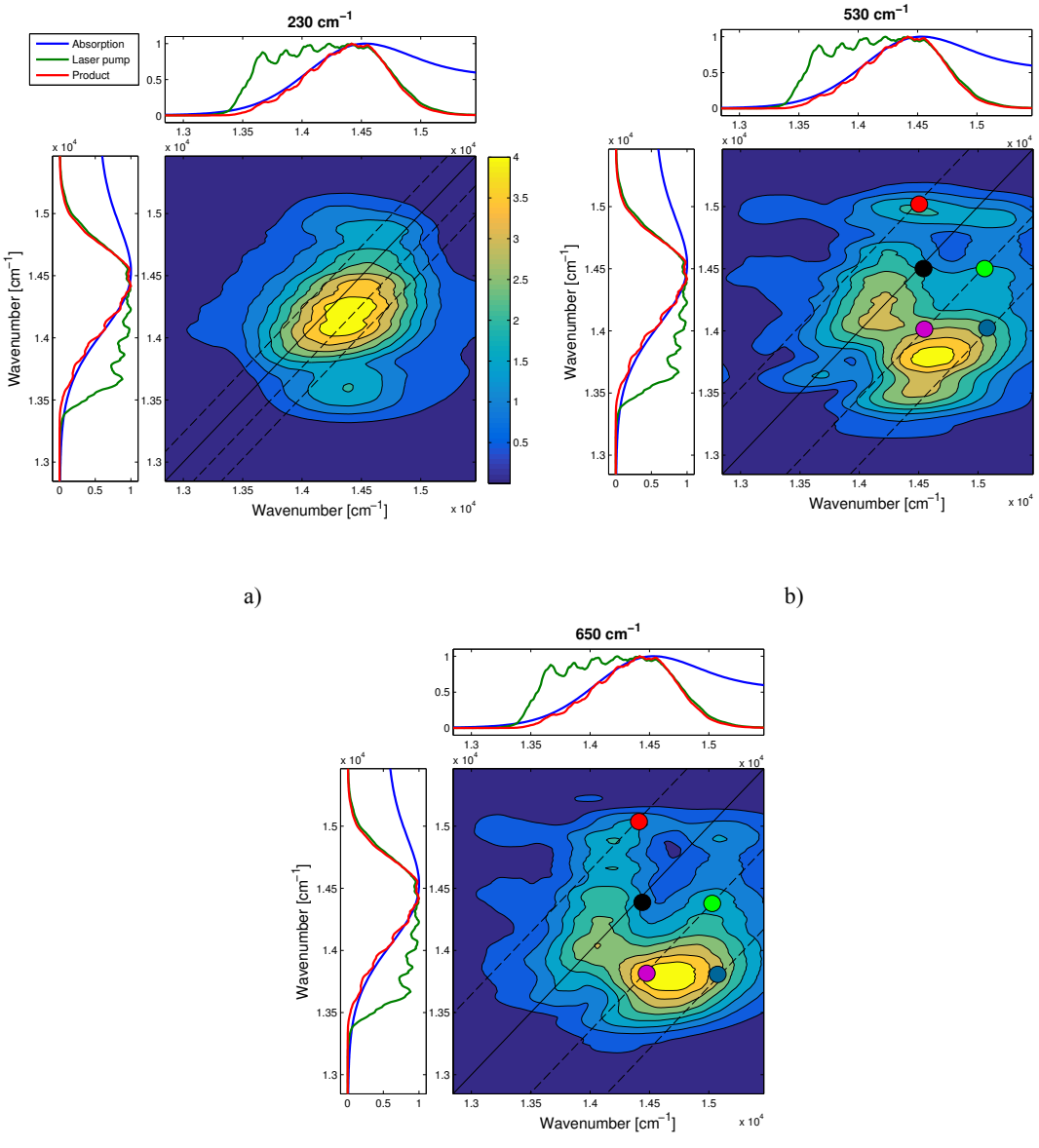

Figure 4.23 Fourier maps for selected frequencies 230 cm^{-1} (a), 530 cm^{-1} (b) and 650 cm^{-1} (c) in THF. The correspondent maps obtained in MeOH solutions present exactly the same patterns and thus they are not shown.

In all the reported Fourier maps the features corresponding to the positions predicted by the response theory are marked with the colours adopted in Chapter 1, in order to distinguish the different contributions. The inhomogeneous broadening is taken into account in the identification of the relevant positions.

In the Fourier map relative to the 230 cm^{-1} component the 2D signal appears as an overall central feature in which all the signals building the *chair symmetry* are included. As for the

530 and 650 cm^{-1} components, all the features in the significant positions can be distinguished, with the signal intensity mainly concentrated in the lower part of the pattern, where only beats due to the ground state vibrations are expected.

The corresponding Fourier maps in the MeOH solution are characterized by the same patterns and are not shown.

We know from the previous analyses that the region between 900 and 1000 cm^{-1} may be affected by solvent contributions. In order to detect the vibrational modes responsible of this interaction, we analyse the Fourier spectrum of coherences deriving by the 2D response of the pure THF and MeOH recorded in the same experimental conditions used for the dye solutions. It resulted indeed that the main signals due to pure solvents are included in the same critical region, as is shown in Figure 4.24.

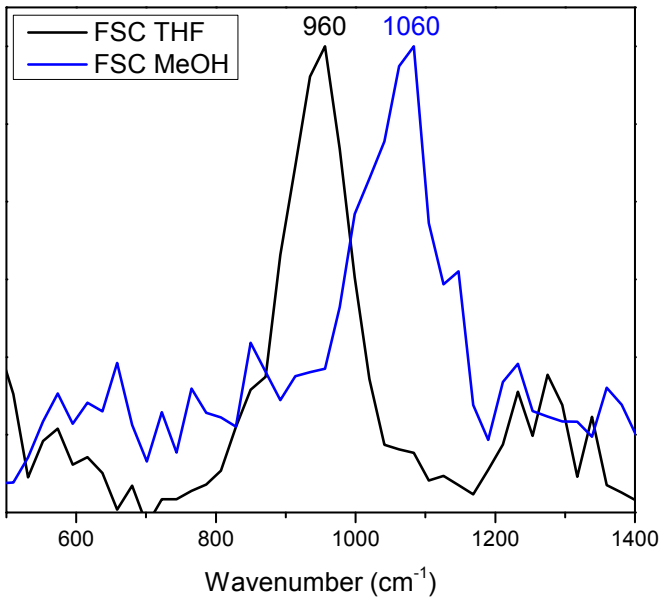

Figure 4.24 Overlap between the normalized FSC spectra of the pure THF and MeOH in the investigated region.

The component at 960 cm^{-1} in the FSC of THF is very close in energy to the mode of the dye at 940 cm^{-1}. On the other hand, the only band appearing in the FSC of MeOH is centred at 1060 cm^{-1}, closer to the bands of the dye at 990 and 1040 cm^{-1}. This behaviour is particularly clear comparing the experimental Raman spectra of BIS BDP and that of the two solvents, reported in Figure 4.25. We can notice that there is a perfect overlap between the 960 cm^{-1} vibrational mode of BIS BDP and of THF. In addition, the band at 1030 cm^{-1} characterizing the vibrational structure of MeOH is closer to the modes at 990 and 1040 cm^{-1} in the sample.

In the light of these evidences two scenarios are possible: (i) the solvent response can simply be added to the dye response or (ii) the main Raman active mode of each solvent interacts with the corresponding mode of the dye closer in frequency. In this latter hypothesis the

solvent molecules more closely associated with the dye molecules in the first solvation sphere would actively contribute to the relaxation dynamics of the dye.

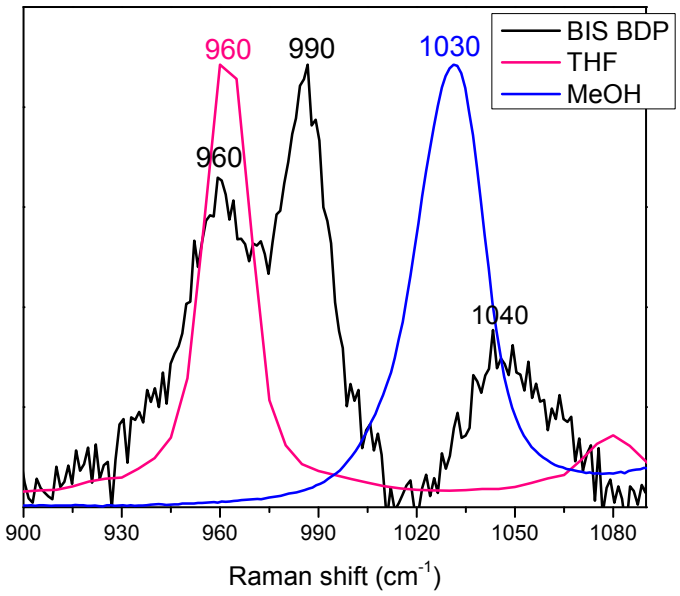

Figure 4.25 Comparison of the normalized Raman spectra of BID BDP, pure THF and pure MeOH in the 900-1000 cm^{-1} region.

In this context, in Figure 4.26 we compare the Fourier maps at 940 and 1000 cm^{-1} obtained for the THF and MeOH solutions, with the corresponding ones measured on the pure solvents.

In the Fourier maps relative to the dye solutions the signal intensity is maximum on the cross peak below the diagonal, where only ground state modes of the dye contribute. In the upper diagonal portion of the map a weak signal, more intense in the case of the methanol solution, appears. The corresponding Fourier maps relative to the pure solvents show a very intense signal exactly in the upper off-diagonal position. Therefore, it can be reasonably deduced that the upper feature in the frequency maps relative to both solutions is due to an additive contribution of solvent, as it is possible to evaluate from the relative intensity of the signals appearing in each pair of maps in comparison.

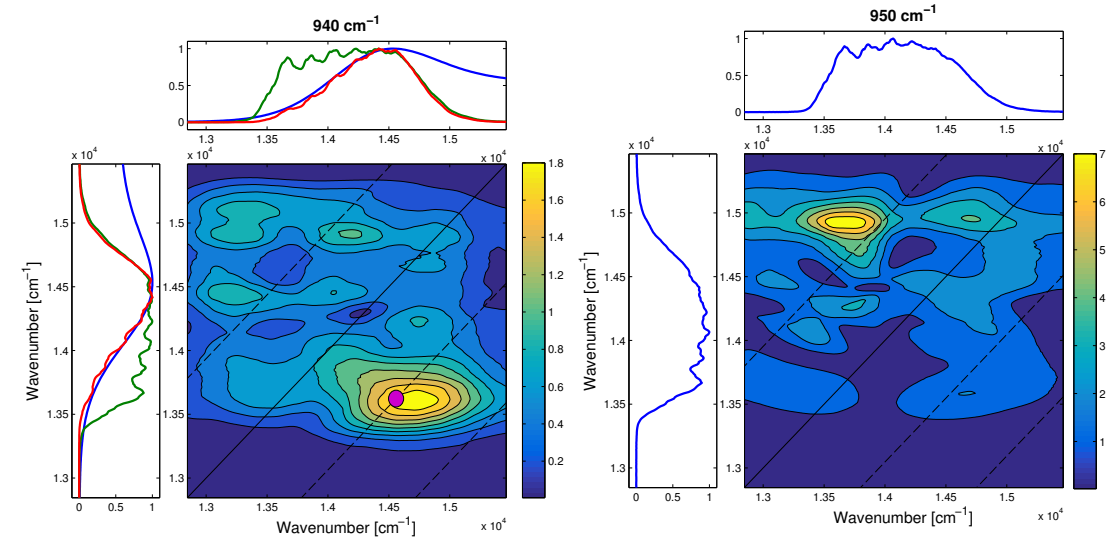

a)

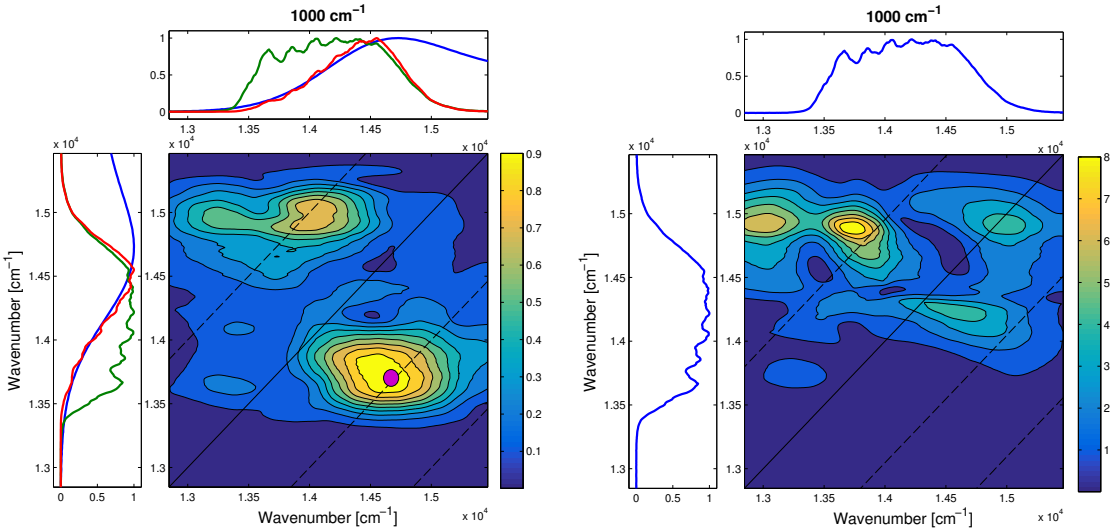

b)

Figure 4.26 Comparison between the Fourier maps relative to the THF (a) and MeOH (b) solutions (left) and the corresponding pure solvent (right) for the 940 cm^{-1} and 1000 cm^{-1} components, respectively.

4.3.6 Concluding remarks

We have seen that the solvent nature only influences the energy of the vibrational modes in the range between 900 and 1000 cm^{-1}, without any relevant effect on their dynamics. If the Raman spectrum of the sample (Figure 4.25) highlights two vibrational modes at 960 and 990 cm^{-1}, in the 2D response of each solution only that closer in energy to the mode of the corresponding solvent is enhanced. This behaviour can be tentatively interpreted as a sum of dye and solvent beating components at the same frequency, as deduced by the Fourier maps analysis. Indeed, from the comparison of the amplitudes and positions of the signals relative to each solution and to the corresponding solvent, it results that the vibrational modes of the solvent provide only an additive contribution to the oscillations. Further analyses will be carried out to confirm this attribution.

Another interesting result is the dynamics of the vibrations detected in the lower diagonal region position, where the ground state contributes more. It was expected that these were long-lasting vibrational coherences, instead they appear as short-living components with respect to the spectral window investigated, meaning that they are damped in relatively short times by some kind of relaxation pathway in which they are involved.

The main frequencies contributing to the overall beating pattern resulting by the excitation on the 0-0 band of BIS BDP in THF are in good agreement with that obtained in the previous set of measures with excitation on the vibronic band. The comparison is reported in Table 4.3.

Table 4.3 Comparison between the main FSC components relative to the two sets of measurements on the 0-0 and vibronic bands made on BIS BDP in THF.

BIS BDP THF	
FSC 0-0 band (±60cm^{-1})	FSC vibronic band (±60cm^{-1})
230 cm^{-1}	250 cm^{-1}
530 cm^{-1}	500 cm^{-1}
650 cm^{-1}	650 cm^{-1}
	830 cm^{-1}
940 cm^{-1}	950 cm^{-1}

At this point, a model level diagram with the main electronic and vibrational levels involved in the 2D response is built for both solutions and shown in Figure 4.27.

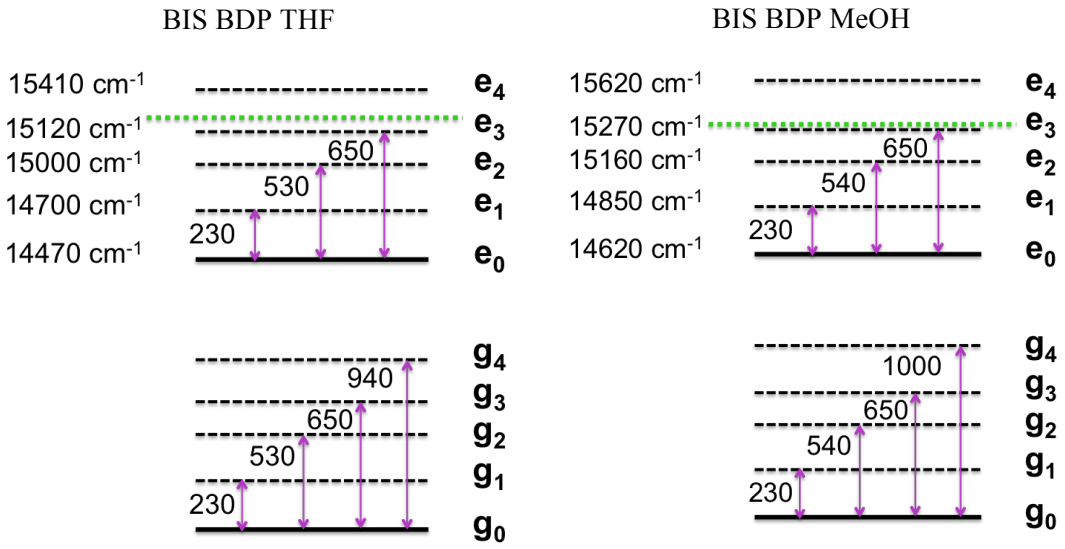

Figure 4.27 Model level diagram for BIS BDP in THF (left) and in MeOH (right). All energies reported are in cm^{-1}.

4.4 NO_2-Biariliden Bodipy: 0-0 band analysis. The substituent effect

We now extend the discussion to the effect of the nitro substituent at the orthogonal position of BIS BDP on its rephasing dynamics. In order to further study the solvent influence, three sets of measurements have been acquired both in THF and MeOH solutions. Also in this case the laser was tuned to cover the 0-0 band of the absorption spectrum of the two solutions of NO_2-BIS BDP (Figure 4.1 c)) in order to allow mainly the characterization of the vibrational coherences in the ground state.

4.4.1 Experimental conditions

Figure 4.28 shows the absorption spectra of the two solutions compared with the laser beam profile kept constant in the two sets of three acquisitions.

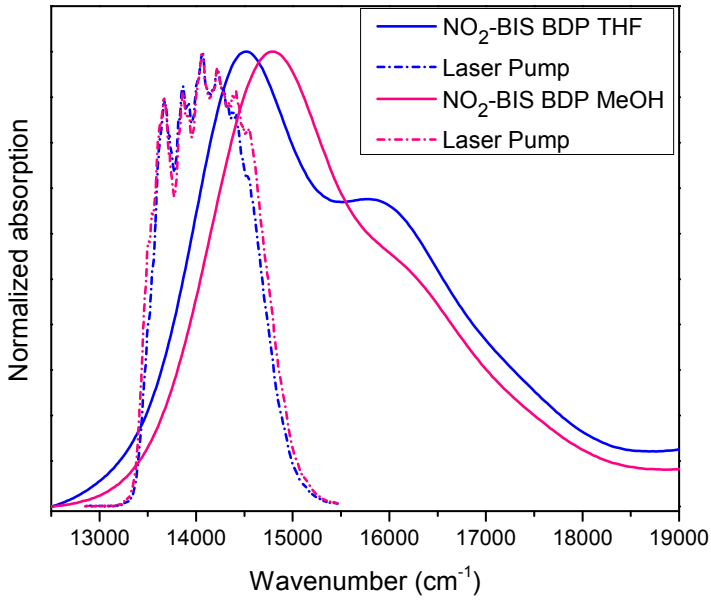

Figure 4.28 Overlap of the absorption spectra of NO_2-BIS BDP in THF and MeOH compared with the laser pump for each set of measures.

The exciting laser beam is characterized by the typical profile assumed in the red spectral region also in this case. The experimental parameters are the same used in the previous set of measures and reported in Section 4.3.1.

4.4.2 Decay evolution along the population time

As in the previous set of measures, the solvent nature does not relevantly affect the decay dynamics along the population time. Figure 4.29 illustrates the evolution along T of the real 2D maps of the THF solution at selected values of T. Figure 4.30 shows one of the 2D maps compared to the available spectral range provided by the product between the absorption spectrum and the laser pump.

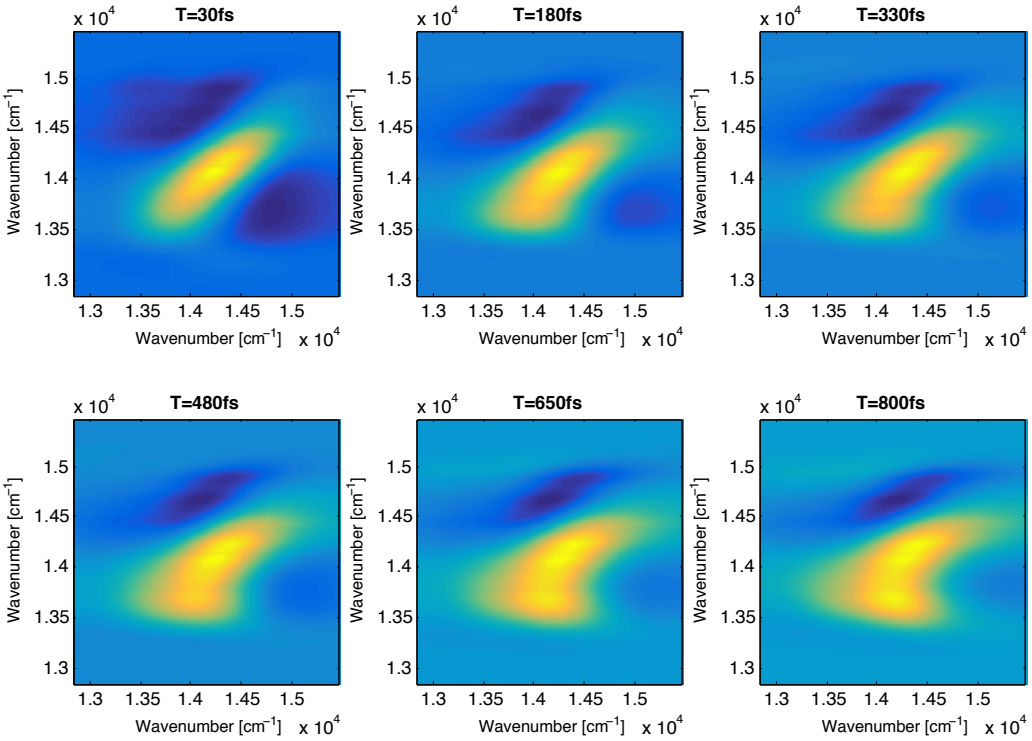

Figure 4.29 2D real maps evolution along T between 0 and 800 fs for NO_2-BIS BDP in THF.

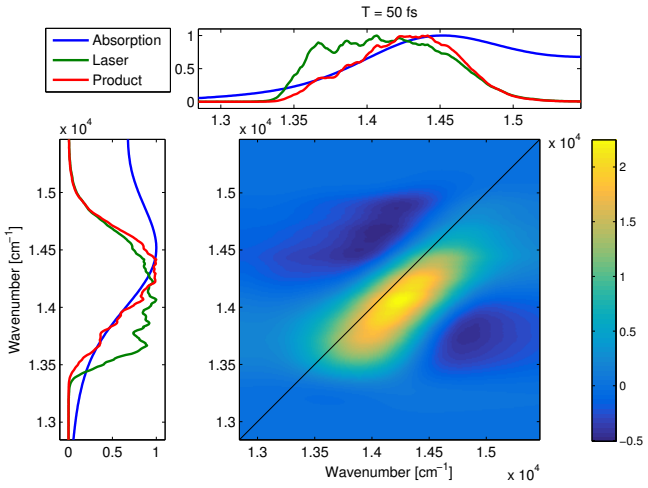

Figure 4.30 2D real map at T=50 fs compared with the available spectral window for NO_2-BIS BDP in THF.

At early times a diagonally elongated central peak and two symmetric negative signals in the upper and lower regions are the main features. The overall dynamics closely resembles the one measured for analogous solutions of the BIS BDP (see Figure 4.18).

The evolution of the corresponding absolute maps illustrated in Figure 4.31 shows a strong beating behaviour in the lower part of the central signal and an increasing intensity in the upper region as the population time increases.

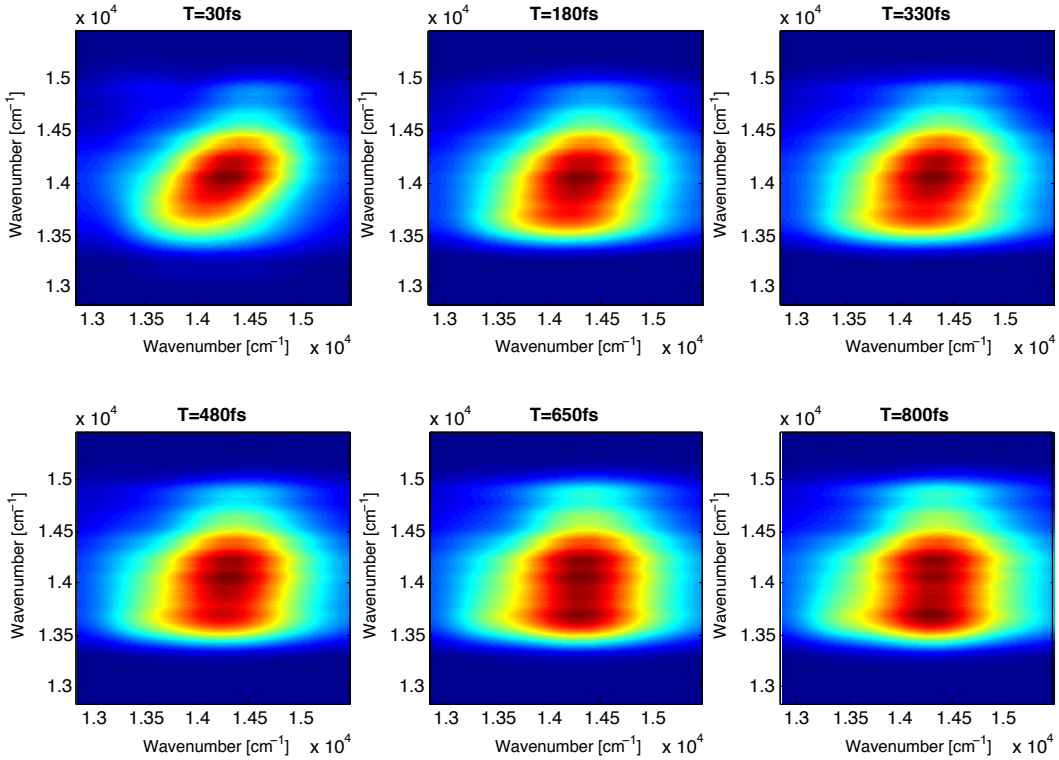

Figure 4.31 2D absolute maps evolution along T between 0 and 800 fs for NO_2-BIS BDP in THF.

4.4.3 Beats analysis: Kinetic on single points

In the following discussion the attention is focused on the effect of the introduction of the nitro group. We show below an example of the analysis performed on single points selected in the lower diagonal region of the maps, which is the most informative for our purposes. Figure 4.32 shows the result of the kinetic analysis applied to the THF solution.

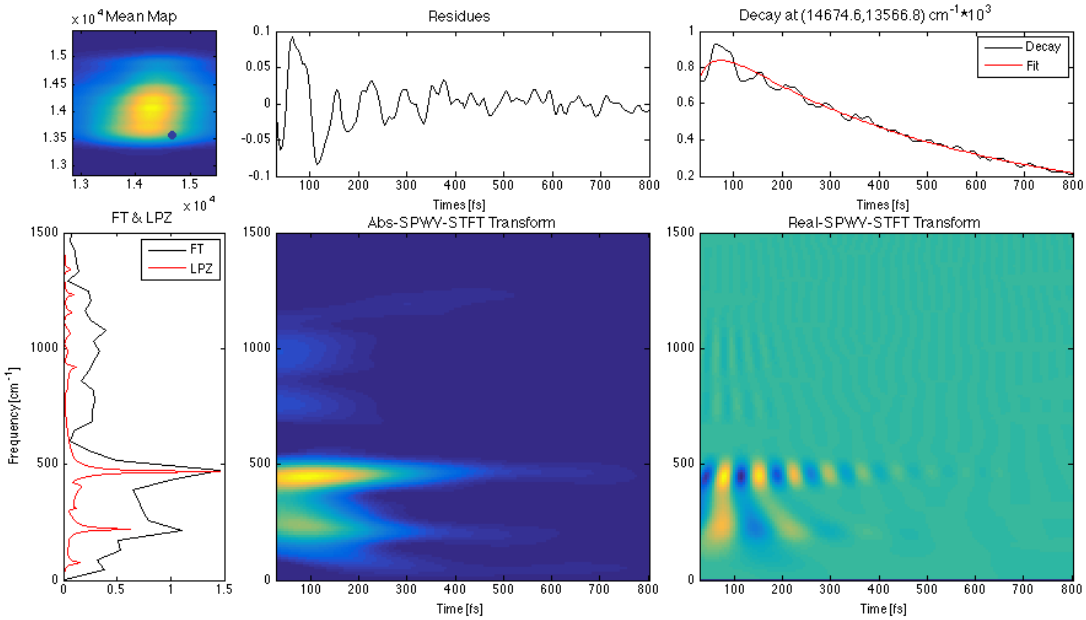

Figure 4.32 Kinetic analysis on the lower diagonal region of the map for NO_2-BIS BDP in THF.

As we can see, a very intense 460 cm^{-1} oscillation, not detected in the previous analysis on the unsubstituted chromophore, appears in the FT and TFT panels. A close look to its dynamics reveals a longer-lasting nature compared to the 200 cm^{-1} mode and the higher frequency components spanning a large interval between 800 and 1200 cm^{-1}. These last, according to the indetermination principle, are indeed characterized by short damping times, which is again an unusual feature for ground state coherences. The overall oscillatory behaviour observed here differs from that found in the unsubstituted BIS BDP, where all the detected ground state signals show mostly the same lifetimes. The comparison between the different dynamics characterizing the two chromophores is shown by the absolute TFT plots reported in Figure 4.33

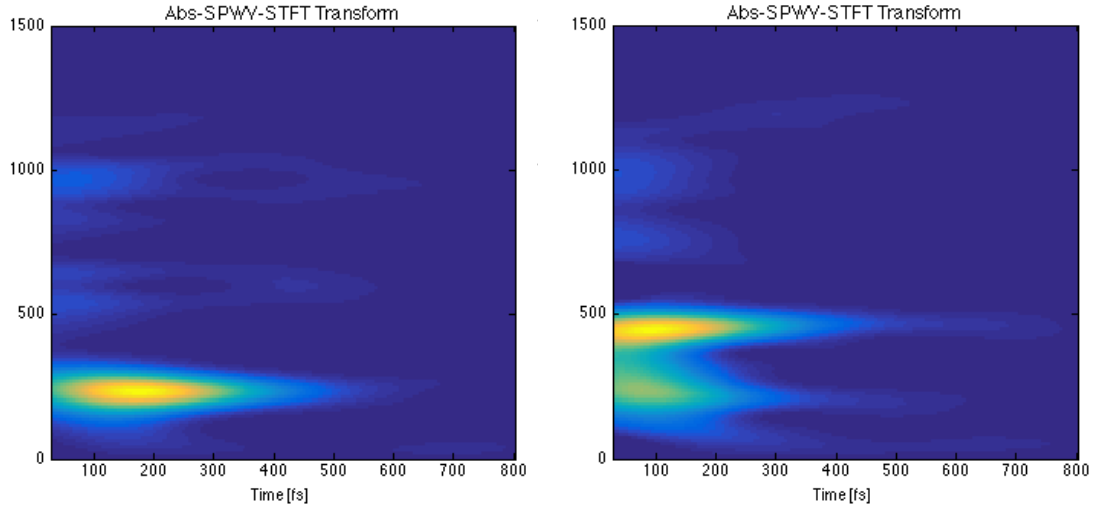

a) b)

Figure 4.33 Comparison between the time-frequency transforms relative to BIS BDP (a) and NO_2-BIS BDP (b).

The damping time of the most intense 460 cm^{-1} has been determined with better accuracy performing a fit of the oscillating residuals with the use of an exponentially damped cosine function. However, the dynamic regarding the short-living signals appearing in Figure 4.32 can only be estimated by the time-frequency analysis since these components are partially hindered by the main mode. The result of the performed fit, which provides a damping time of 190 fs, is shown in Figure 4.34.

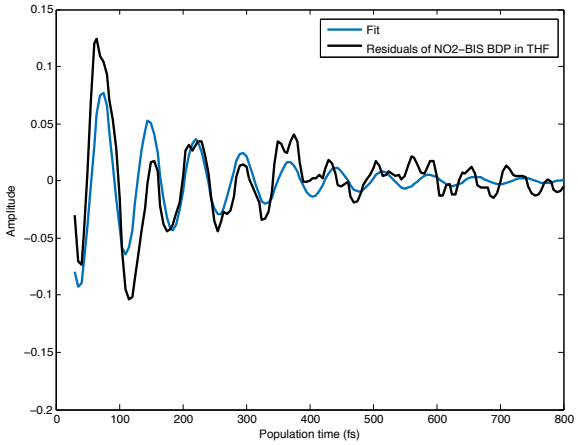

Fit Model

$$y(t) = \cos(2\pi\omega t + \phi) * A * \exp\left(-\frac{t}{t_{damp}}\right)$$

Figure 4.34 Damping time determination for the 460 cm^{-1} component in NO_2-BIS BDP.

The obtained damping time is shorter compared to that of 360 fs relative to the main beating component resulted from the analysis of the unsubstituted dye (Figure 4.21). The same trend characterizes the weaker signals detected at higher frequencies in the two chromophores, as shown in Figure 4.33: in the presence of the nitro substituent they result shorter-living.

Overall, the introduction of the nitro group at the orthogonal position of BIS BDP has a very strong influence on the dynamic of its vibrational coherences in the ground state.

As we can expect, the situation does not change going from the THF to the methanol solution, confirming that solvent does not affect the beats dynamics. Figure 4.35 reports an example of the kinetic analysis performed on the interesting lower region of the 2D map relative to the NO_2-BIS BDP in MeOH.

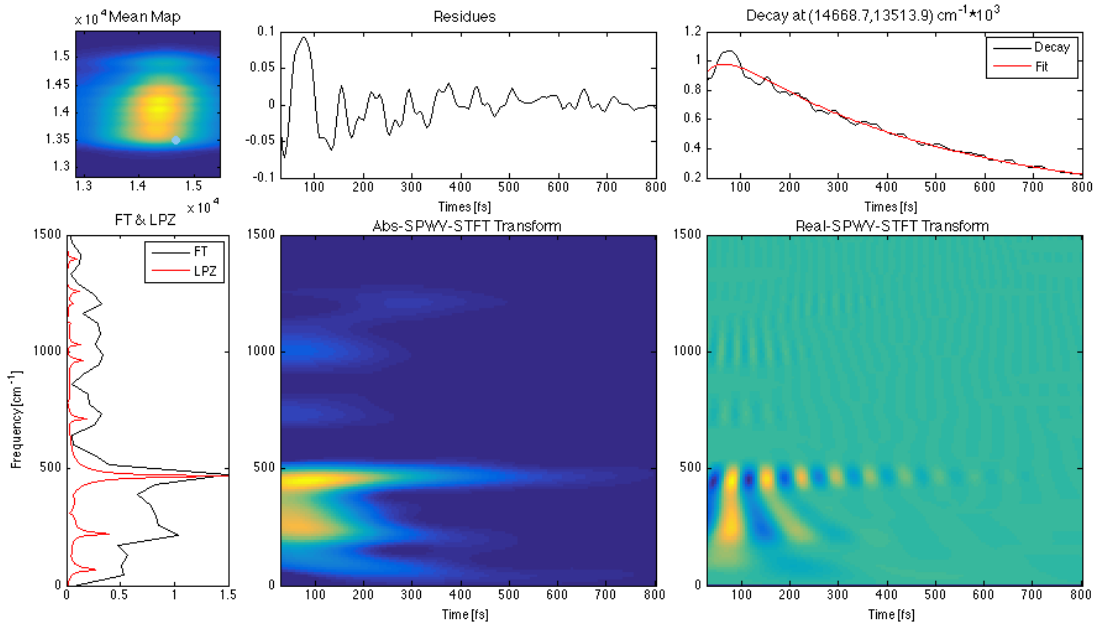

Figure 4.35 Kinetic analysis on the lower diagonal region of the map for NO_2-BIS BDP in MeOH.

The lower frequency components 230 and 460 cm^{-1} are the predominant contributions in the 2D spectra of BIS BDP and of the nitro-substituted dye respectively. Therefore, we can expect that the dynamics of the two dyes is modulated through the coupling with these main vibrational modes. A closer look to the main components of the relaxation processes characterizing the two chromophores has been obtained as follows: a vertical slice of the 2D map of each sample has been selected in the region where the signal is maximum, and the signal along the slice has been plotted as function of the population time. Figure 4.36 a) and b) show the selected vertical slice in the left panel and the relative decay dynamics along T on the right hand side, for BIS BDP and NO_2-BIS BDP, respectively.

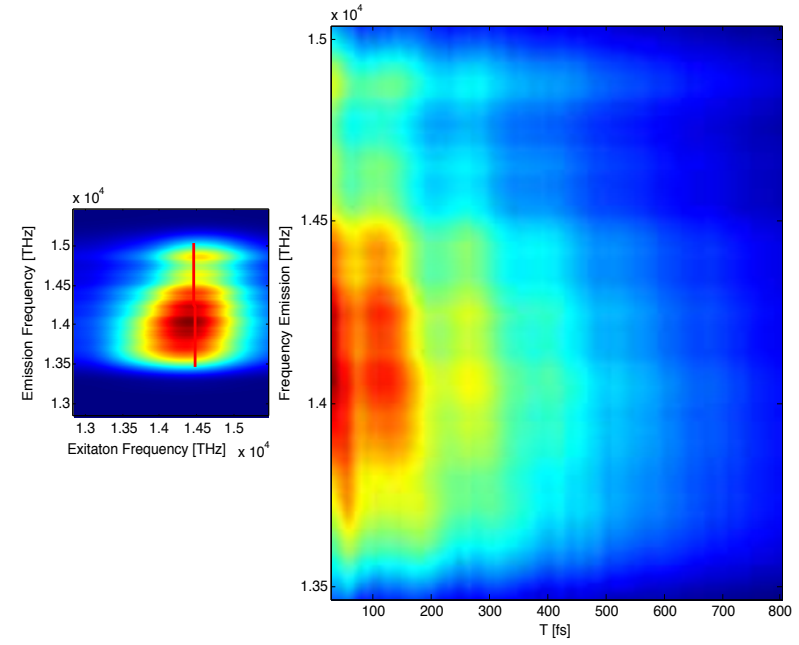

a)

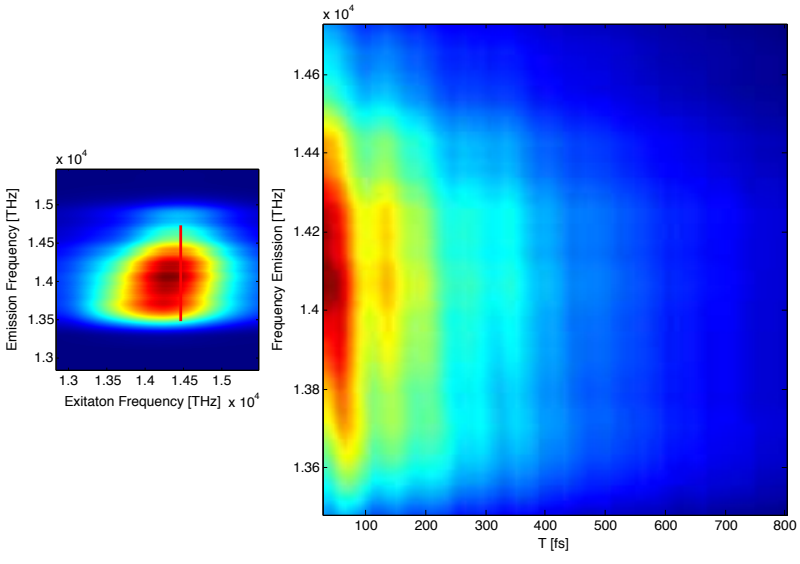

b)

Figure 4.36 Comparison between the main components of the relaxation dynamic along T for BIS BDP (a) and NO_2-BIS BDP (b).

A relaxation process, indicated by the shift of the signal intensity from the higher to the lower energies, is revealed in the first hundred fs of each plot. Two main oscillations of different period modulate the signal amplitude of the two slices: we can identify the 230 cm^{-1} in the case of BIS BDP and the 460 cm^{-1} in that of the nitro-substituted dye, in agreement with the previous results.

4.4.4 Overall beats analysis: Fourier spectrum of coherences

The comparison between the Fourier spectra of coherences relative to the nitro-substituted dye in both solutions is reported in Figure 4.37 a). The resonant Raman spectrum relative to NO_2-BIS BDP is also shown in Figure 4.37 b) in order to identify the vibrational modes of ground state in the signals appearing in the FSC spectra.

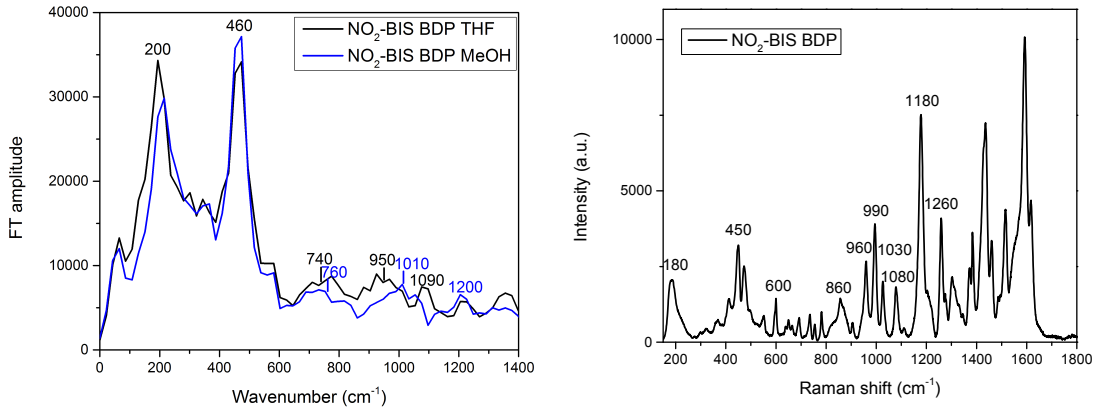

a) b)

Figure 4.37 Overlap between the FSC spectra relative to NO_2-BIS BDP in the THF and MeOH solutions (a). Resonant Raman spectrum of NO_2-BIS BDP (b).

The most intense signals appearing at 200 and 460 cm^{-1} are in agreement with the main contributions observed in the previous analysis. The two broadened bands spanning large intervals between 600-850 cm^{-1} and 850-1100 cm^{-1}, correspond to that resulted from the Fourier Transform of the oscillating residuals along T (Figure 4.32 and Figure 4.35) and are characterized by very short damping times. The detailed attribution of the 2D spectra signals to the ground state vibrational modes is reported in Table 4.4.

Table 4.4 Comparison between the main signals of the FSC spectra relative to the THF and MeOH solutions and the Raman modes.

FSC NO_2-BIS BDP THF ($\pm 60 cm^{-1}$)	FSC NO_2-BIS BDP MeOH ($\pm 60 cm^{-1}$)	Raman NO_2-BIS BDP
200 cm^{-1}	200 cm^{-1}	180 cm^{-1}
460 cm^{-1}	460 cm^{-1}	450 cm^{-1}
740 cm^{-1}	760 cm^{-1}	740 cm^{-1} (weak signal)
950 cm^{-1}		960 cm^{-1}
	1010 cm^{-1}	990 cm^{-1}
1090 cm^{-1}		1080 cm^{-1}
1200 cm^{-1}	1200 cm^{-1}	1180 cm^{-1}

The intense mode at 200 cm^{-1} is identified with the weak signal at 180 cm^{-1} in the Raman spectrum, while the 460 cm^{-1}corresponds to the 450 cm^{-1} component in the Raman. The bands at around 750 cm^{-1} found in the FSC spectra can be associated to the very weak signal at around 740 cm^{-1} in the Raman, thus showing particular relevance at shorter times. The Raman modes at 600 and 860 cm^{-1} are not clearly distinguishable in the FSC but they may be included in the large intervals covered by the previously discussed bands.

The solvent influence in the region around 900-1100 cm^{-1} appears evident also in this case. The vibrational mode with an averaged value around 950 cm^{-1} is enhanced in the THF solution, while the higher 1010 cm^{-1} frequency characterizes the 2D response of the methanol solution in the critical region. Both signals correspond to the ground state vibrational modes highlighted by Raman at 960 and 990 cm^{-1} respectively, in spite of their short-living nature.

It is interesting to compare the coherences resulted from the analyses of the Fourier spectra relative to the BIS BDP and the nitro-substituted dye, as shown in Table 4.5.

Table 4.5 Substituent effect. Data reported in cm^{-1}.

FSC THF solutions		FSC MeOH solutions		Raman	
BIS BDP	NO_2 BIS BDP	BIS BDP	NO_2 BIS BDP	BIS BDP	NO_2 BIS BDP
230	200	230	200	230	180
	460		460		450
530		540		540	
650		650		600	600
	740		760		740
		870		860	860
940	950			960	960
		1000	1010	990	990
	1090				1080
	1200		1200	1180	1180

The region with the more relevant energy differences between the two chromophores is highlighted in cyan. The region where the solvent effect acts is highlighted in green.

Overall, we can note that the introduction of the nitro substituent provides the modulation of the frequencies mainly in the interval between 400 and 800 cm^{-1}, in both 2D and Raman spectra. This effect is particularly evident in the case of the 460 cm^{-1} mode, totally absent in the unsubstituted dye, but becoming the main component of the relaxation dynamics in the presence of the nitro group.

4.4.5 Beats analysis: Fourier Maps

Figure 4.38 shows the Fourier maps observed in THF solution relative to the selected frequencies. Solution in MeOH shows a completely analogous behaviour.

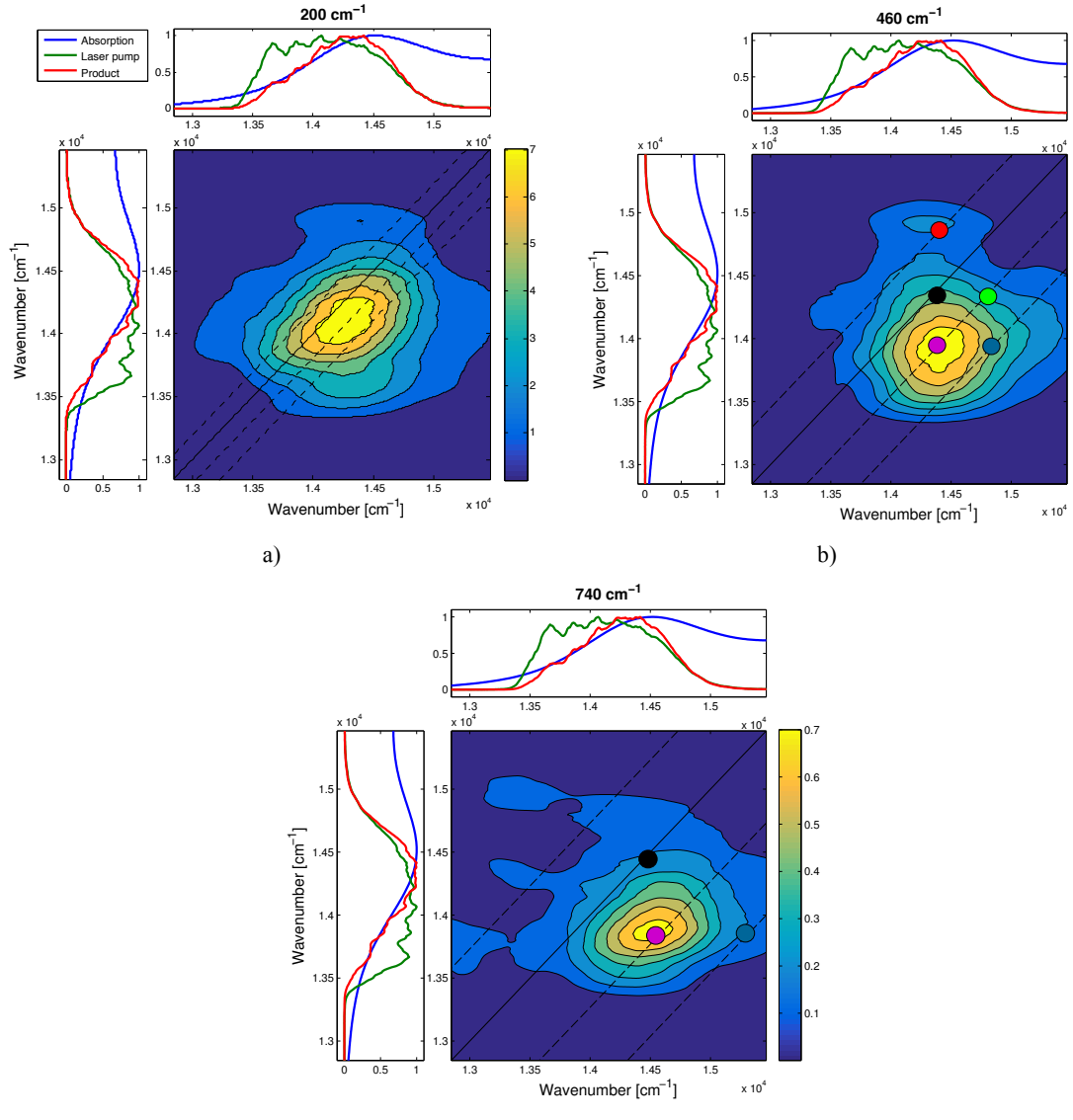

Figure 4.38 Fourier maps for selected frequencies 200 cm^{-1} (a), 460 cm^{-1} (b) and 740 cm^{-1} (c) for THF solution. Similar maps have been obtained for MeOH solution.

For the 200 and 460 cm^{-1} components the whole *chair symmetry* typical of vibrational coherences can be detected. For the 740 cm^{-1} mode the recorded signal is mainly concentrated on the position of the lower cross peak arising from the ground state. The Fourier maps relative to the frequencies enhanced by the interaction with the corresponding solvent mode are reported in Figure 4.39. The analogous maps of the pure solvents are also shown for comparison.

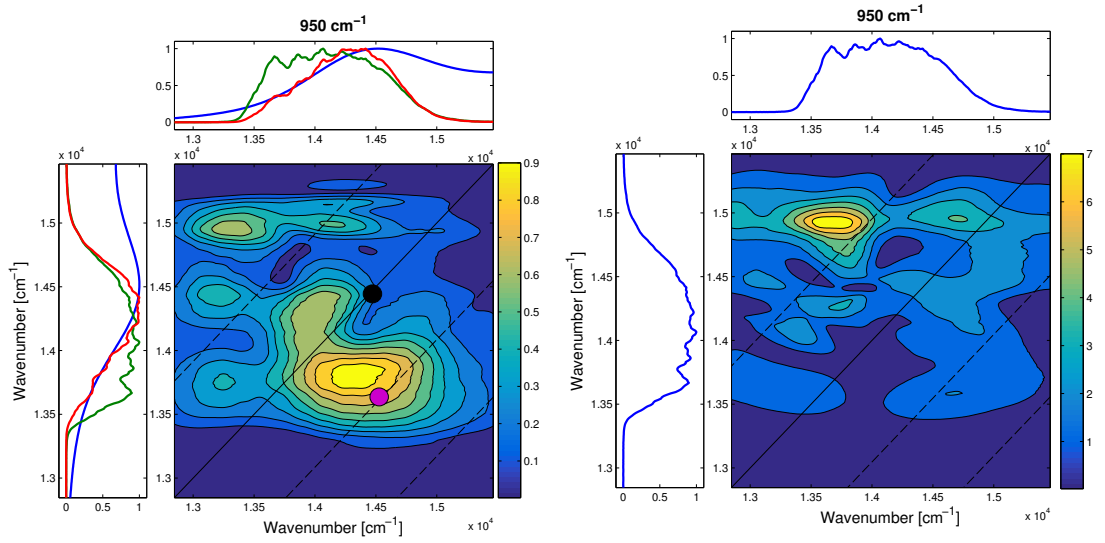

a)

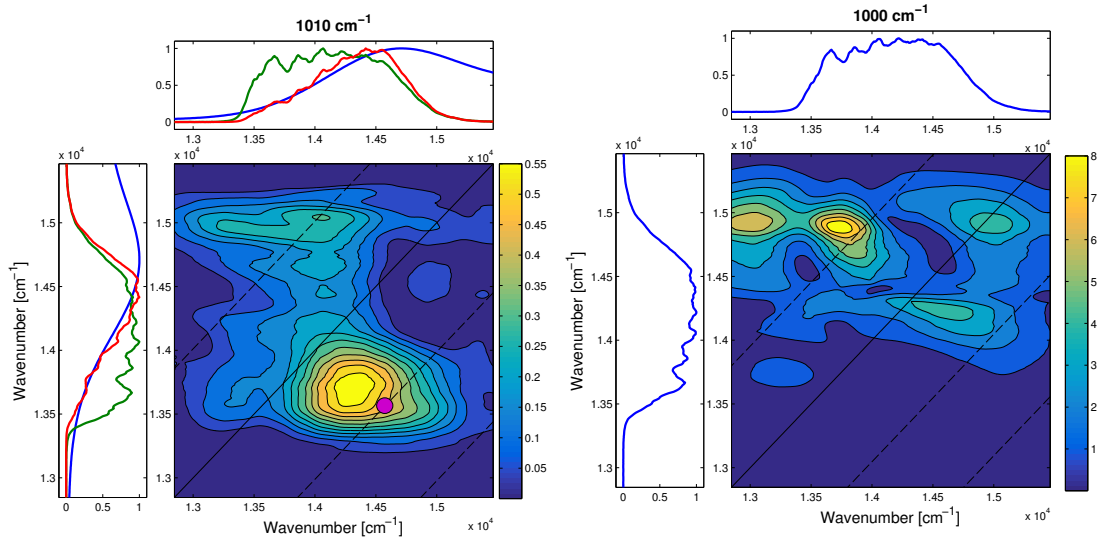

b)

Figure 4.39 Comparison between the Fourier maps relative to the THF (a) and MeOH (b) solutions and the corresponding solvent for the 950 cm^{-1} and 1010 cm^{-1} components, respectively.

Again, the Fourier maps relative to the 950 and 1010 cm^{-1} modes for the THF and MeOH solutions respectively, result from the mixture of two different contributions: the weak signal in the portion of the map above the diagonal can be associated to the pure solvent, while the lower diagonal cross peak arises from the ground state of the BODIPY molecule. Also in this case the interaction with solvent is manifested as an additive contribution.

4.4.6 Concluding remarks

The introduction of the nitro group on the orthogonal position to the BODIPY core provides an interesting modulation of the vibrational modes characterizing the structure of Biariliden BODIPY. The most relevant case regards the 460 cm^{-1} component, totally absent in the unsubstituted dye, which represents the main contribution modulating the relaxation

dynamics of the NO_2-BIS BDP. The most interesting effect is manifested on the dynamics of the vibrational coherences, which in the presence of the nitro substituent are damped in much shorter times. In addition, the weaker signals spanning large intervals of frequencies have very different dynamics from that of the main 460 cm^{-1} component, which persists for a longer time. This behaviour completely differs from that found in the unsubstituted dye where the detected coherences show mostly equal damping times.

The analysis of the Fourier spectra of coherences has provided the same vibrational modes characterized by the Raman, except for the 740/760 cm^{-1} component in the THF and MeOH solutions respectively, which appears as a very weak signal in the Raman thus results relevant only at shorter times. The additive contribution of solvent to the modes at around 950/1010 cm^{-1} is clearly detected also in this case.

The model level diagram highlighting the main vibrational modes involved in the 2D response is built for both solutions and shown below (Figure 4.40).

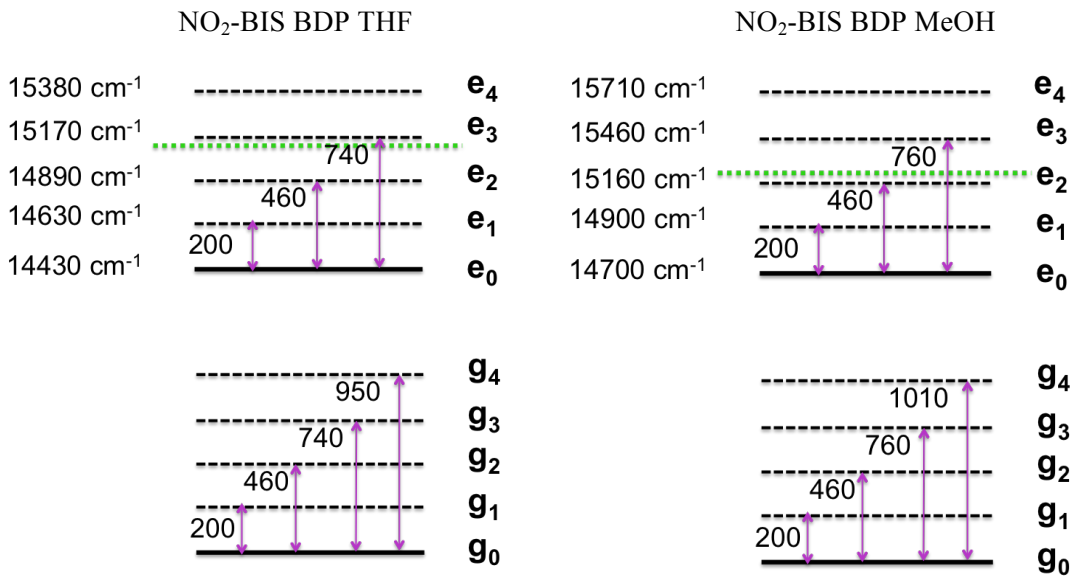

Figure 4.40 Model level diagram for NO_2-BIS BDP in THF (left) and in MeOH (right). All energies reported are in cm^{-1}.

4.5 Discussion: an overview on the 2DPE results

Different sets of 2DPE measurements have been acquired on differently substituted BODIPY dyes, varying the experimental conditions in terms of solvent nature and exciting laser band. The performed analyses have allowed a thorough study of the effects of several structural and environmental factors on the 2D response of the chromophores under investigation.

We started from the comparison between the MONO and BIS BDP (Figure 4.1 a) and b)) in order to analyse the effect of the different degree of conjugation and branching provided by the introduction of styryl units on the core of the chromophore. The first main evidence emerging from this comparison is the different relative intensity of the signals in the FSC of the two chromophores. In particular, the frequencies in the range 400-800 cm^{-1} appear much more intense in the MONO than in the BIS, as found in the preliminary Raman analysis. Also in the light of dynamical information, we tentatively explain this behaviour through the hypothesis of a coordinated motion of the two styryl branches in BIS BDP, which would hinder the contributions of the higher vibrational modes with respect to the 250 cm^{-1}. A similar behaviour has been theoretically proposed for dimers of chromophores; in ref. [35] the authors indeed demonstrate as vibrational frequencies get suppressed upon dimer formation.

A second evidence is the different dynamics of the common 950 cm^{-1} vibrational coherence, which also manifests its main contribution in opposite regions of the 2D maps of the two dyes. Although the presence of coordinated motion of the two styryl branches may be again invoked to justify the quicker damping of the 950 cm^{-1} component, a possible contribution of the solvent must also be taken into account. We expect that the solvent contributes in different positions and with different mechanisms in the two different spectral ranges investigated, therefore leading to the different signals recorded in the two samples. Therefore a direct quantitative comparison is not fully possible.

The analysis has been further complicated by the choice of performing the measures with a laser band centred on the vibronic band, in order to characterize the relaxation dynamics within the first excited state. We verified that, in these conditions, vibronic and vibrational coherences close in frequency can overlap giving rise to very complex Fourier maps. Therefore, in the following analyses we have chosen to change the exciting conditions, in order to characterize mainly the vibrational coherences arising from the ground state. To this aim, the laser pulse has been tuned so to cover much lower energies than in the previous case.

The recorded data have suggested the possible presence of solvent contributions in the Fourier map of the 950 cm^{-1} mode, owing that THF is characterized by a strong Raman active mode at the same frequency. With the aim of studying the nature of this possible contribution and verify the presence of specific interactions with the first solvation sphere, two sets of measurements in two different solvents, THF and MeOH, have been performed on both BIS BDP and NO_2-BIS BDP. The resulting Fourier spectra of coherences and Fourier maps relative to the two solutions are evidently affected by the vibrational solvent contribution in the region between 900 and 1000 cm^{-1}. The starting point for this analysis is well illustrated in Figure 4.41 by the overlap of the Raman spectra of samples and solvents used.

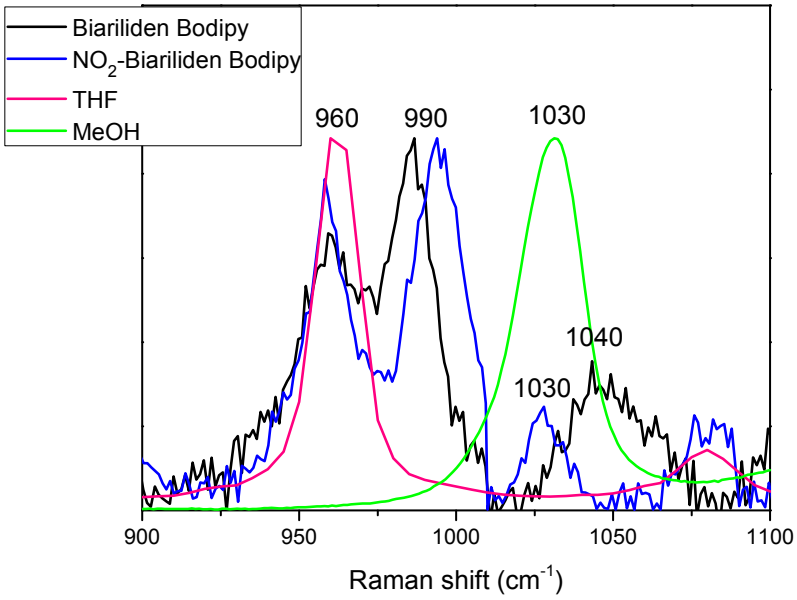

Figure 4.41 Overlap of the Raman spectra relative to BIS BDP, NO_2-BIS BDP, THF and MeOH.

As we can see, the vibrational mode of THF at 960 cm^{-1} falls exactly at the same frequency of the lower energy modes of both samples in the selected region. We thus expect that THF contribution is more relevant in the Fourier map relative to the vibrational mode of the samples at 960 cm^{-1} whereas MeOH should contribute more in the 990 cm^{-1} region. This is indeed what was found in the FCS obtained from 2D spectra.

The analysis of the corresponding Fourier maps has allowed identifying the contribution of the solvent as an additive interaction. In the Fourier maps at these frequencies we could indeed verify the presence of a signal above diagonal fully attributable to solvent contribution. Moreover, the results suggest that the solvent nature does not affect the relaxation dynamics of the vibrational coherences characterizing the sample, supporting the hypothesis that there are no specific coupling interactions between solvent and dye molecules. It is worthy to stress out that this behaviour is strictly valid in the particular

spectral region investigated, since, as already stated before, solvent may have different response at different wavelengths. The role of solvent has always been neglected in 2D literature since typically we are interested in the optical properties of the solvated dyes. However, in this thesis we demonstrated that solvent may lead to non-negligible contributions to the overall 2D response and if not conveniently taken into account, it can lead to mistakes and misinterpretations.

On the other hand, the introduction of an acceptor substituent as the nitro group in the orthogonal position of the BODIPY core causes not only a relative shift of the beating frequencies in the range between 400 and 800 cm^{-1} with respect to the unsubstituted dye, but there is also an overall effect on the dynamics of the oscillations detected. They appear indeed as shorter-living components than in the case of BIS BDP, in spite of their similar ground state nature.

We have found that the relaxation dynamics of BIS BDP is mainly modulated by the 250 cm^{-1}, which may be associated to a soft mode involved in the first redistribution of nuclear coordinates following the electronic transition. The introduction of the nitro group leads to the appearance of a new 460 cm^{-1} mode, totally absent in the dynamics characterizing the unsubstituted dye, which becomes the predominant contribution in the 2D spectra. Moreover, while in the BIS BDP all the beating frequencies are characterized by the same damping time, in NO_2-BIS BDP not only the damping times are in general shorter, but also different frequencies present different lifetimes. This clearly implies a completely different relaxation dynamics among the mainly ground state vibrational states. The explanation of these evidences from the molecular point of view is still under investigation.

All the performed analyses have allowed us to confirm the power of 2DPE in studying the dynamics of coherent superpositions of states and in identifying the nature of the couplings between the electronic transitions and the vibrational modes. In addition, the sensitivity of this technique to the multitude of effects deriving from multi-branching, solvent role and chemical substitutions, has been efficiently tested. It is important to stress out that the same information cannot be provided by other conventional spectroscopic techniques.

Conclusions

The research work presented in this thesis has concerned the study of the ultrafast relaxation dynamics in BODIPY dyes, organic chromophores structurally similar to porphyrins, which are the artificial light-harvesters analogue to chlorophylls. Special attention has been devoted to the characterization of the quantum coherences active during the relaxation dynamics observed trough 2D spectroscopy and manifested as oscillations of the signal amplitude. The origin and the nature of these quantum phenomena are indeed one of the hottest fields of research in optical spectroscopy, since the observation that long-lasting coherences may improve the efficiency and the speed of energy transfer in natural photosynthetic complexes [109]. Although many claims in the recent years have proposed the coupling between electronic transitions and quasi-resonant vibrational modes as the origin of quantum correlations in energy transport [15]–[17], many are the questions still open about the nature of this mechanism and the role of environment in the observed behaviour. The better way to understand the intimate correlation between the molecular structure and the main vibrational degrees of freedom that are directly involved in the coherent dynamics, is to focus first on single dyes instead of complex multi-chromophoric systems, where the identification of the nature of quantum features is complicated by the presence of both pure vibrational and electronic coherences. To this aim, the relaxation dynamics in the first picosecond after excitation in BODIPY dyes has been characterized by means of 2DPE, paying particular attention on the role played by solvent. Recent results obtained in our group suggest indeed the involvement of vibrational modes of solvent itself in the coherent oscillations [108]. This is a crucial preliminary step for the characterization of electronic coherences driving energy transfer processes in dimers or multichromophoric assemblies of BODIPYs, planned in the near future.

Firstly, a systematic study on the photophysical properties and fluorescent dynamics in the ns regime of BODIPY dyes differently substituted in significant positions was performed by means of linear techniques (absorption and fluorescence spectroscopies). The experimental data obtained for different dyes have been compared and interpreted on the base of what suggested in literature about the chemistry of these successful chromophores. The more interesting samples to be studied with 2D electronic spectroscopy were selected and further characterized trough Raman spectroscopy to provide a first insight in the vibrational modes active in the ground state manifold. The Raman analysis provided a very helpful support for the 2D characterization of the vibrations more strongly coupled with the electronic transition and contributing to the coherent relaxation dynamics.

Taking advantage of one of the few available setup for 2DPE, available in our lab, different sets of measurements were performed on mono- and distyryl substituted BODIPY dyes, with and without the functionalization with a nitro group in the orthogonal position of the BODIPY core.

In the first comparison between Mono and Biariliden BODIPYs performed exciting the samples on the vibronic band of their absorption spectra, we had the aim to reveal the effect of the different degree of branching and conjugation on the relaxation dynamics captured in both ground and first excited states. The results obtained suggested that some kind of coordinated motion of the two styryl branches in Biariliden BODIPY contributes to hide the higher frequency vibrational modes (400-800 cm^{-1}) with respect to a lower frequency component (250 cm^{-1}), corresponding to a soft mode involved in the first redistribution of nuclear coordinates following the electronic transition. This behaviour seems to be in accordance with that theoretically proposed for dimers of chromophores [107]. In the specific case of MONO BDP, unexpected oscillating superpositions between hot vibrational states was observed in addition to pure vibrational couplings in both the ground and the excited states. This represented one of the first observations of this kind of 'hot states' coherent superpositions. Moreover, the detection of a strong long-lived oscillation at 950 cm^{-1}, a frequency close to a vibrational mode of the THF solvent, suggested a possible role of solvent itself in the enhancement of the quantum beats observed at this frequency. To shed light on this aspect, measurements were performed in two different solvents to deduce by comparison the influence of the solvation sphere on the relaxation dynamics of the chromophore. To simplify the analysis of the coherences mainly arising from the ground state, these further analyses were carried out by exciting the red portion of the absorption spectra of the samples.

The sets of measurements performed on Biariliden BODIPY in THF and MeOH clarified the role of solvent. Starting from the comparison between the Raman spectra of the sample and of the two solvents, we observed that the contributions at about 950 and 1000 cm^{-1} in THF and MeOH, respectively, exactly overlap with a mode at the same frequency in the corresponding solution. From the Fourier map analysis relatively to those frequencies, the contribution of solvent to the oscillation associated to the molecule in each solution was sharply distinguishable as an additive effect. Further analysis will be carried out to confirm this attribution and to deeply study this very interesting behaviour. These data represent one of the first evidence of how solvent can actively contributes to the overall beating behaviour of 2D maps and represent therefore a noticeable warning in the interpretation of past and future 2D data.

As further investigation, we verified how the introduction of a nitro group in the so-called orthogonal position of the BODIPY core could affect the dynamics of the dye. The obtained results confirmed the presence of a new oscillation at about 450 cm^{-1}, totally absent in the 2D response of the unsubstituted dye, appeared as the main contribution to the overall oscillating pattern. Furthermore, the introduction of the nitro group lead to relevant changes in the dephasing dynamics of the coherent oscillations. The origin of this effect from the molecular point of view goes beyond the scope of this thesis and is still an open question. Further analyses are required to deepen the study of this effect, and we plan them for the near future.

In conclusion, this dissertation has provided for the first time in the literature an example of a complete analysis of the influence of specific substituents, structural changes and solvent on the ultrafast dynamics of a chromophore.

On one hand, we argue that this kind of systematic preliminary analysis of the behaviour of single chromophores is a crucial step for the characterization of more complex multi-chromophoric systems. It allows indeed to identify source of possible misinterpretation, such as the role of solvent, until now neglected in the literature data, but here demonstrated to be absolutely non negligible.

On the other hand, we believe that this analysis is a first step towards the proposal of guidelines for the design of molecular systems with tailored properties, for example bio-inspired artificial light-harvesting complexes, able to reproduce or even increase the energy transfer yield of the natural systems.

References

[1] E. Collini, "Spectroscopic signatures of quantum-coherent energy transfer.," *Chem. Soc. Rev.*, vol. 42, pp. 4932–47, 2013.

[2] E. Schrödinger (trans. John. D. Trimmer), "The Present Situation in Quantum Mechanics: A Translation of Schrödinger's 'Cat Paradox Paper' (translation of Schrödinger, 1935)," *Proc. Am. Philos. Soc.*, vol. 124, no. 5, pp. 323–338, 1980.

[3] P. Jordan, "Die Physikunddas Geheimnisdesorganischen Lebens", Friedrich Vieweg & Sohn, Braunschweig, 1943.

[4] Masoud Mohseni-Masoud Mohseni, Yasser Omar, Gregory S. Engel, Martin B. Plenio, "Quantum Effects in Biology", Cambridge, 1974.

[5] S. F. Huelga and M. B. Plenio, "Vibrations, Quanta and Biology," *Contemp. Phys.*, vol. 54, no. 4, pp. 181–207, 2013.

[6] Leonas Valkunas, Darius Abramacivius, Tomas Mancal, "Molecular Excitation Dynamics and Relaxation: Quantum Theory and Spectroscopy", While, 2013.

[7] a. W. Chin, S. F. Huelga, and M. B. Plenio, "Coherence and decoherence in biological systems: principles of noise-assisted transport and the origin of long-lived coherences," *Philos. Trans. R. Soc. A*, vol. 370, no1972, pp. 3638–3657, 2012.

[8] D. M. Jonas, "TWO-DIMENSIONAL FEMTOSECOND SPECTROSCOPY", *Annu. Rev. Phys. Chem.*, vol. 54, no. 1, pp. 425–463, 2003.

[9] G. D. Scholes, "Quantum-coherent electronic energy transfer: Did nature think of it first?," *J. Phys. Chem. Lett.*, vol. 1, no. 1, pp. 2–8, 2010.

[10] E. Collini, C. Y. Wong, K. E. Wilk, P. M. G. Curmi, P. Brumer, and G. D. Scholes, "Coherently wired light-harvesting in photosynthetic marine algae at ambient temperature," *Nature*, vol. 463, pp. 644–647, 2010.

[11] M. Mohseni, P. Rebentrost, S. Lloyd, and A. Aspuru-Guzik, "Environment-assisted quantum walks in photosynthetic energy transfer," *J. Chem. Phys.*, vol. 129, 2008.

[12] M. B. Plenio and S. F. Huelga, "Dephasing-assisted transport: Quantum networks and biomolecules," *New J. Phys.*, vol. 10, 2008.

[13] G. S. Engel, T. R. Calhoun, E. L. Read, T.-K. Ahn, T. Mancal, Y.-C. Cheng, R. E. Blankenship and G. R. Fleming, "Evidence for wavelike energy transfer through quantum coherence in photosynthetic systems.," *Nature*, vol. 446, pp. 782–786, 2007.

[14] G. Panitchayangkoon, D. Hayes, K. A. Fransted, J. R. Caram, E. Harel, J. Wen, R. E. Blankenship, and G. S. Engel, "Long-lived quantum coherence in photosynthetic complexes at physiological temperature.," *Proc. Natl. Acad. Sci. U. S. A.*, vol. 107, no. 29, pp. 12766–12770, 2010.

[15] M. B. Plenio, J. Almeida, and S. F. Huelga, "Origin of long-lived oscillations in 2D-spectra of a quantum vibronic model: Electronic versus vibrational coherence," *J. Chem. Phys.*, vol. 139, no. 23, 2013.

[16] V. Tiwari, W. K. Peters, and D. M. Jonas, “Electronic resonance with anticorrelated pigment vibrations drives photosynthetic energy transfer outside the adiabatic framework.,” *Proc. Natl. Acad. Sci. U. S. A.*, vol. 110, no. 4, pp. 1203–1208, 2013.

[17] a. W. Chin, J. Prior, R. Rosenbach, F. Caycedo-Soler, S. F. Huelga, and M. B. Plenio, “The role of non-equilibrium vibrational structures in electronic coherence and recoherence in pigment–protein complexes,” *Nat. Phys.*, vol. 9, no. 2, pp. 113–118, 2013.

[18] T. Azumi and K. Matsuzaki , “What does the term “vibronic coupling’ mean?”, *Photochem. Photobiol.*, vol. 25, no 4, pp. 315–326, 1977.

[19] G. D. Scholes, G. R. Fleming, A. Olaya-Castro, and R. van Grondelle, “Lessons from nature about solar light harvesting” *Nat. Chem.*, vol. 3, no. 10, pp. 763–774, 2011.

[20] P. Hamm, “Principles of Nonlinear Optical Spectroscopy : A Practical Approach or: Mukamel for Dummies,” 2005.

[21] A. Tokmakoff, “Time-Dependent Quantum Mechanics and Spectroscopy”, 2014.

[22] P. Drude, “Zur Elektronentheorie der Metalle,” *Ann. Phys.*, vol. 306, no. 3, pp. 566–613, 1900.

[23] L. Jeanne McHale “Molecular Spectroscopy”, Prentice Hall College Div, 1998.

[24] E. Schrödinger, “An undulatory theory of the mechanics of atoms and molecules,” *Phys. Rev.*, vol. 28, no. 6, pp. 1049–1070, 1926.

[25] S. Mukamel “Principles of nonlinear optical spectroscopy” Oxford, 1996 (pdf).

[26] W. W. Parson, “Modern Optical Spectroscopy: With Examples from Biophysics”, 2009.

[27] A. Halpin, “Two dimensional spectroscopy of molecular excitons in a model dimmer system”, PhD Thesis, 2014.

[28] R. Kubo, “A STOCHASTIC THEORY OF LINE SHAPE,” *Advances in Chemical Physics,* vol. XV, no. 1, 1969.

[29] M. Blume, “Stochastic theory of Line Shape: Generalization of the Kubo-Anderson Model”, *Physical Rewiev*, vol. 174, no. 2, pp 351-358, 1968.

[30] R. W. Boyd, “Nonlinear Optics”, 2007.

[31] R. Dinshaw, “Spectroscopic Investigations of the Photophysics of Cryptophyte Light-Harvesting”, PhD Thesis, 2012.

[32] C. Y. Wong, “Spectroscopic Studies of CdSe Nanocrystal Fine Structure and Electronic Coherences in Cryptophyte Algae”, PhD Thesis, 2011.

[33] J. D. Hybl, A. A. Ferro, D. M. Jonas, “Two-dimensional Fourier transform electronic spectroscopy”, *J. Chem. Phys.,* vol. 115, no. 14, pp 6606-6622, 2001.

[34] D. B. Turner, R. Dinshaw, K.-K. Lee, M. S. Belsley, K. E. Wilk, P. M. G. Curmi, and G. D. Scholes, “Quantitative investigations of quantum coherence for a light-harvesting protein at conditions simulating photosynthesis,” *Phys. Chem. Chem. Phys.*, vol. 14, no. 14, pp 4857-4874, 2012.

[35] V. Butkus, D. Zigmantas, L. Valkunas, and D. Abramavicius, “Vibrational vs.

electronic coherences in 2D spectrum of molecular systems," *Chem. Phys. Lett.*, vol. 545, pp. 40–43, 2012.

[36] D. B. Turner, K. E. Wilk, P. M. G. Curmi, and G. D. Scholes, "Comparison of Electronic and Vibrational Coherence Measured by Two-Dimensional Electronic Spectroscopy," *J. Phys. Chem. Lett.*, vol. 2, no. 15, pp. 1904–1911, 2011.

[37] M. Del Rey, A. W. Chin, S. F. Huelga, and M. B. Plenio, "Exploiting structured environments for efficient energy transfer: The phonon antenna mechanism," *J. Phys. Chem. Lett.*, vol. 4, no. 6, pp. 903–907, 2013.

[38] Epictetus and N. P. White, "The Handbook." 1983.

[39] G. Ulrich, R. Ziessel, and A. Harriman, "The chemistry of fluorescent bodipy dyes: Versatility unsurpassed," *Angew. Chemie - Int. Ed.*, vol. 47, no. 7, pp. 1184–1201, 2008.

[40] H. Lu, J. Mack, Y. Yang, and Z. Shen, "Structural modification strategies for the rational design of red/NIR region BODIPYs," *Chem. Soc. Rev.*, vol. 43, no. 13, pp. 4778–4823, 2014.

[41] R. Ziessel, G. Ulrich, and A. Harriman, "The chemistry of Bodipy: A new *El Dorado* for fluorescence tools," *New J. Chem.*, vol. 31, no. 4, pp. 496–501, 2007.

[42] N. Boens, V. Leen, and W. Dehaen, "Fluorescent indicators based on BODIPY," *Chem. Soc. Rev.*, vol. 41, no. 3, pp. 1130–1172, 2012.

[43] A. Treibs and F.-H. Kreuzer, "Difluorboryl-Komplexe von Di- und Tripyrrylmethenen," *Justus Liebigs Ann. Chem.*, vol. 718, no. 1, pp. 208–223, 1968.

[44] H. Falk, O. Hofer, and H. Lehner, "Beitrage zur Chemie der Pyrrolpigmente, 1. Mitt.: Der induzierte Circulardichroismus einiger Pyrromethenderivate in cholesterischer Mesophase," *Monatshefte fur Chemie*, vol. 105, no. 1, pp. 169–178, 1974.

[45] E. Vos de Wael, J. A. Pardoen, J. A. van Koeveringe and J. Lugtenurg, "Pyrromethene-BF, complexes (4,4'-difluoro-4-bora-3a,4adiaza-s-indacenes). Synthesis and luminescence properties", *Journal of the Royal Netherlands Chemical Society,* vol. 96, no. 12, pp. 306–309, 1977.

[46] H. J. Wories, J. H. Koek, G. Lodder and J. Lugtenburg, "A nover water-soluble fluorescent probe: Synthesis, luminescence and biological properties of the 4-sulfonato-3,3',5,5'-tetramethyl-2,2'-pyrromethen,1,1'-BF_2 complex" *Recueil des Travaux Chimiques des Pays-Bas,* vol.104, pp. 288–291, 1985.

[47] O. Publications, "United States Patent [191," pp. 2–6, 1978.

[48] F. J. Monsma, a C. Barton, H. C. Kang, D. L. Brassard, R. P. Haugland, and D. R. Sibley, "Characterization of novel fluorescent ligands with high affinity for D_1 and D_2 dopaminergic receptors.," *J. Neurochem.*, vol. 52, no. 5, pp. 1641–1644, 1989.

[49] A. C. Benniston and G. Copley, "Lighting the way ahead with boron dipyrromethene (Bodipy) dyes.," *Phys. Chem. Chem. Phys.*, vol. 11, no. 21, pp. 4124–4131, 2009.

[50] A. Loudet and K. Burgess, "BODIPY Dyes and Their Derivatives: Syntheses and Spectroscopic Properties," *Chem. Rev.*, vol. 107, no. 11, pp. 4891–4932, 2007.

[51] K. Rurack, M. Kollmannsberger, and J. Daub, "A highly efficient sensor molecule

emitting in the near infrared (NIR): 3,5-distyryl-8-(*p*-dimethylaminophenyl)difluoroboradiaza-s-indacene," *New J. Chem.*, vol. 25, no. 2, pp. 289–292, 2001.

[52] M. J. Ortiz, I. Garcia-Moreno, A. R. Agarrabeitia, G. Duran-Sampedro, A. Costela, R. Sastre, F. Lopez Arbeloa, J. Banuelos Prieto, and I. Lopez Arbeloa, "Red-edge-wavelength finely-tunable laser action from new BODIPY dyes," *Phys. Chem. Chem. Phys.*, vol. 12, no. 28, pp. 7804–7811, 2010.

[53] Y. Gabe, Y. Urano, K. Kikuchi, H. Kojima, and T. Nagano, "Highly sensitive fluorescence probes for nitric oxide based on boron dipyrromethene chromophore-rational design of potentially useful bioimaging fluorescence probe.," *J. Am. Chem. Soc.*, vol. 126, no. 10, pp. 3357–3367, 2004.

[54] T. Chen, J. H. Boyer, and M. L. Trudell, "Synthesis of 2,6-diethyl-3-methacroyloxymethyl-1,5,7,8-tetramethylpyrromethene-BF_2 for the preparation of new solid-state laser dyes," *Heteroat. Chem.*, vol. 8, no. 1, pp. 51–54, 1997.

[55] C. McCusker, J. B. Carroll, and V. M. Rotello, "Cationic polyhedral oligomeric silsesquioxane (POSS) units as carriers for drug delivery processes.," *Chem. Commun. (Camb).*, vol. 1, no. 8, pp. 996–998, 2005.

[56] R. K. Lammi, A. Ambroise, T. Balasubramanian, R. W. Wagner, D. F. Bocian, D. Holten, and J. S. Lindsey, "Structural control of photoinduced energy transfer between adjacent and distant sites in multiporphyrin arrays," *J. Am. Chem. Soc.*, vol. 122, no. 31, pp. 7579–7591, 2000.

[57] R. Y. Lai and A. J. Bard, "Electrogenerated chemiluminescent properties of selected dipyrromethene - BF_2 dyes," *J. Phys. Chem B.*, vol. 107, pp. 5036–5042, 2003.

[58] S. Hattori, K. Ohkubo, Y. Urano, H. Sunahara, T. Nagano, Y. Wada, N. V. Tkachenko, H. Lemmetyinen, and S. Fukuzumi, "Charge separation in a nonfluorescent donor-acceptor dyad derived from boron dipyrromethene dye, leading to photocurrent generation," *J. Phys. Chem. B*, vol. 109, no. 32, pp. 15368–15375, 2005.

[59] M. E. El-Khouly, S. Fukuzumi, and F. D'Souza, "Photosynthetic antenna-reaction center mimicry by using boron dipyrromethene sensitizers," *ChemPhysChem*, vol. 15, no. 1, pp. 30–47, 2014.

[60] A. Burghart, L. H. Thoresen, J. Chen, K. Burgess, F. Bergstrom, and L. B.-A. Johansson, "Energy transfer cassettes based on BODIPY dyes," *Chem. Commun.*, no. 22, pp. 2203–2204, 2000.

[61] T. Yogo, Y. Urano, Y. Ishitsuka, F. Maniwa, and T. Nagano, "Highly efficient and photostable photosensitizer based on BODIPY chromophore," *J. Am. Chem. Soc.*, vol. 127, no. 35, pp. 12162–12163, 2005.

[62] A. Schmitt, B. Hinkeldey, M. Wild, and G. Jung, "Synthesis of the core compound of the BODIPY dye class: 4,4'-difluoro-4-bora-(3a,4a)-diaza-*s*-indacene," *J. Fluoresc.*, vol. 19, no. 4, pp. 755–758, 2009.

[63] Y. Ni and J. Wu, "Far-red and near infrared BODIPY dyes: synthesis and applications for fluorescent pH probes and bio-imaging.," *Org. Biomol. Chem.*, vol. 12, no. 23, pp. 3774–91, 2014.

[64] F. López Arbeloa, J. Bañuelos, V. Martínez, T. Arbeloa, and I. López Arbeloa, "Structural, photophysical and lasing properties of pyrromethene dyes," *Int. Rev. Phys. Chem.*, vol. 24, no. 2, pp. 339–374, 2005.

[65] T. Chaudhuri, S. Mula, S. Chattopadhyay, and M. Banerjee, "Photophysical properties of the 8-phenyl analogue of PM567: A theoretical rationalization," *Spectrochim. Acta - Part A Mol. Biomol. Spectrosc.*, vol. 75, no. 2, pp. 739–744, 2010.

[66] F. López Arbeloa, J. Bañuelos Prieto, V. Martínez Martínez, T. Arbeloa López, and I. López Arbeloa, "Intramolecular charge transfer in pyrromethene laser dyes: Photophysical behaviour of PM650," *ChemPhysChem*, vol. 5, no. 11, pp. 1762–1771, 2004.

[67] J. Bañuelos Prieto, F. López Arbeloa, V. Martínez Martínez, T. Arbeloa López, F. Amat-Guerri, M. Liras, and I. López Arbeloa, "Photophysical properties of a new 8-phenyl analogue of the laser dye PM567 in different solvents: Internal conversion mechanisms," *Chem. Phys. Lett.*, vol. 385, no. 1–2, pp. 29–35, 2004.

[68] T. L. Arbeloa, F. L. Arbeloa, I. L. Arbeloa, I. García-Moreno, A. Costela, R. Sastre, and F. Amat-Guerri, "Correlations between photophysics and lasing properties of dipyrromethene–BF_2 dyes in solution," *Chem. Phys. Lett.*, vol. 299, no. 3–4, pp. 315–321, 1999.

[69] F. Bergstrom, I. Mikhalyov, P. Hagglof, R. Wortmann, T. Ny, and L. B.A Johansson, "Dimers of dipyrrometheneboron difluoride (BODIPY) with light spectroscopic applications in chemistry and biology," *J. Am. Chem. Soc.*, vol. 124, no. 2, pp. 196–204, 2002.

[70] J. Bañuelos Prieto, F. López Arbeloa, V. Martínez Martínez, and I. López Arbeloa, "Theoretical study of the ground and excited electronic states of pyrromethene 546 laser dye and related compounds," *Chem. Phys.*, vol. 296, no. 1, pp. 13–22, 2004.

[71] P. Acebal, S. Blaya, and L. Carretero, "Ab initio study of absorption and emission spectra of PM567," *Chem. Phys. Lett.*, vol. 374, pp. 206–214, 2003.

[72] F. López Arbeloa, T. López Arbeloa, I. López Arbeloa, I. García-Moreno, A. Costela, R. Sastre, and F. Amat-Guerri, "Photophysical and lasing properties of pyrromethene 567 dye in liquid solution.: Environment effects," *Chem. Phys.*, vol. 236, no. 1–3, pp. 331–341, 1998.

[73] Z.-H. Pan, G.-G. Luo, J.-W. Zhou, J.-X. Xia, K. Fang, and R.-B. Wu, "A simple BODIPY-aniline-based fluorescent chemosensor as multiple logic operations for the detection of pH and CO_2 gas.," *Dalton Trans.*, vol. 43, no. 22, pp. 8499–507, 2014.

[74] K. Rurack, M. Kollmannsberger, and U. Resch-genger, "A Selective and Sensitive Fluoroionophore for Hg II , Ag I , and Cu II with Virtually Decoupled Fluorophore and Receptor Units," *Mater. Res.*, vol. 2, no. 13, pp. 968–969, 2000.

[75] F. Li, S. I. Yang, Y. Ciringh, J. Seth, C. H. Martin, D. L. Singh, D. Kim, R. R. Birge, D. F. Bocian, D. Holten, and J. S. Lindsey, "Design, synthesis, and photodynamics of light-harvesting arrays comprised of a porphyrin and one, two, or eight boron-dipyrrin accessory pigments," *J. Am. Chem. Soc.*, vol. 120, no. 39, pp. 10001–10017, 1998.

[76] J. Chen, A. Burghart, A. Derecskei-Kovacs, and K. Burgess, “4,4-Difluoro-4-bora-3a,4a-diaza-s-indacene (BODIPY) dyes modified for extended conjugation and restricted bond rotations,” *J. Org. Chem.*, vol. 65, no. 10, pp. 2900–2906, 2000.

[77] M. Kollmannsberger, K. Rurack, and U. Resch-genger, “Ultrafast Charge Transfer in Amino-Substituted Boron Dipyrromethene Dyes and Its Inhibition by Cation Complexation : A New Design Concept for Highly Sensitive Fluorescent Probes,” pp. 10211–10220, 1998.

[78] L. Li, J. Han, B. Nguyen, and K. Burgess, “Syntheses and spectral properties of functionalized, water-soluble BODIPY derivatives,” *J. Org. Chem.*, vol. 73, no. 5, pp. 1963–1970, 2008.

[79] A. B. Descalzo, H. J. Xu, Z. Shen, and K. Rurack, “Red/near-infrared boron-dipyrromethene dyes as strongly emitting fluorophores,” *Ann. N. Y. Acad. Sci.*, vol. 1130, pp. 164–171, 2008.

[80] E. Deniz, G. C. Isbasar, Ö. A. Bozdemir, L. T. Yildirim, A. Siemiarczuk, and E. U. Akkaya, “Bidirectional switching of near IR emitting boradiazaindacene fluorophores,” *Org. Lett.*, vol. 10, no. 16, pp. 3401–3403, 2008.

[81] J. Bañuelos, V. Martín, C. F. A. Gómez-Durán, I. J. A. Córdoba, E. Peña-Cabrera, I. García-Moreno, Á. Costela, M. E. Pérez-Ojeda, T. Arbeloa, and Í. L. Arbeloa, “New 8-Amino-BODIPY derivatives: Surpassing laser dyes at blue-edge wavelengths,” *Chem. - A Eur. J.*, vol. 17, no. 26, pp. 7261–7270, 2011.

[82] I. Esnal, J. Bañuelos, I. López Arbeloa, A. Costela, I. Garcia-Moreno, M. Garzón, A. R. Agarrabeitia, and M. José Ortiz, “Nitro and amino BODIPYS: crucial substituents to modulate their photonic behavior,” *RSC Adv.*, vol. 3, p. 1547, 2013.

[83] W. Qin, M. Baruah, M. Van Der Auweraer, F. C. De Schryver, and N. Boens, “Photophysical properties of borondipyrromethene analogues in solution,” *J. Phys. Chem. A*, vol. 109, no. 33, pp. 7371–7384, 2005.

[84] D. Phillips, R. C. Drake, D. V O’Connor, and R. L. Christensen, “Time Correlated Single-Photon Counting (Tcspc) Using Laser Excitation,” *Instrum. Sci. Technol.*, vol. 14, no. 3, pp. 267–292, 1985.

[85] E. Smith and G. Dent, *Modern Raman Spectrocopy: A Practical Approach*. 2005.

[86] “libra manual on Coherent inc” [Online]. Available: http://lasers.coherent.com/lasers/libra-manual. [Accessed: 9-March-2016]

[87] “Topas White specifications on Light Conversion inc” [Online]. Available: http://www.lightcon.com/products/product.php?ID=156 [Accessed: 9-March-2016]

[88] P. F. Tekavec, J. a Myers, K. L. M. Lewis, F. D. Fuller, and J. P. Ogilvie, “Effects of chirp on two-dimensional Fourier transform electronic spectra.,” *Opt. Express*, vol. 18, no. 11, pp. 11015–11024, 2010.

[89] P. Tournois, “Compensation of group delay time dispersion in laser systems,” *Opt. Commun.*, vol. 140, no. 4–6, pp. 245–249, 1997.

[90] M. L. Cowan, J. P. Ogilvie, and R. J. D. Miller, “Two-dimensional spectroscopy using diffractive optics based phased-locked photon echoes,” *Chem. Phys. Lett.*, vol. 386, no. 1–3, pp. 184–189, 2004.

[91] A. Nemeth, J. Sperling, J. Hauer, H. F. Kauffmann, and F. Milota, "Compact phase-stable design for single- and electronic spectroscopy," vol. 34, no. 21, pp. 3301–3303, 2009.

[92] T. Brixner, T. Mančal, I. V. Stiopkin, and G. R. Fleming, "Phase-stabilized two-dimensional electronic spectroscopy," *J. Chem. Phys.*, vol. 121, no. 9, p. 4221, 2004.

[93] "Newton CCD specifications" [Online]. Available: http://www.andor.com/scientific-cameras/newton-ccd-and-emccd-cameras/newton-920 [Accessed: 9-March-2016]

[94] R. Augulis and D. Zigmantas, "Two-dimensional electronic spectroscopy with double modulation lock-in detection: enhancement of sensitivity and noise resistance," *Opt. Express*, vol. 19, no. 14, p. 13126, 2011.

[95] R. Trebino, K. W. Delong, D. N. Fittinghoff, J. N. Sweetser, M. A. Krumbügel, B. A. Richman, and D. J. Kane, "Measuring ultrashort laser pulses in the time-frequency domain using frequency-resolved optical gating," *Rev. Sci. Instrum.*, vol. 68, no. 9, pp. 3277–3295, 1997.

[96] V. P. Singh, A. F. Fidler, B. S. Rolczynski, and G. S. Engel, "Independent phasing of rephasing and non-rephasing 2D electronic spectra," *J. Chem. Phys.*, vol. 139, no. 8, 2013.

[97] F. Fassioli, A. Olaya-Castro, and G. D. Scholes, "Coherent Energy Transfer under Incoherent Light Conditions," *J. Phys. Chem. Lett.*, vol. 3, no. 21, pp. 3136–3142, 2012.

[98] E. E. Ostroumov, R. M. Mulvaney, J. M. Anna, R. J. Cogdell, and G. D. Scholes, "Energy transfer pathways in light-harvesting complexes of purple bacteria as revealed by global kinetic analysis of two-dimensional transient spectra," *J. Phys. Chem. B*, vol. 117, no. 38, pp. 11349–11362, 2013.

[99] F. V. A. Camargo, H. L. Anderson, S. R. Meech, and I. A. Heisler, "Time-Resolved Twisting Dynamics in a Porphyrin Dimer Characterized by Two-Dimensional Electronic Spectroscopy," *J. Phys. Chem. B*, vol. 119, no. 46, pp. 14660–14667, 2015.

[100] I. H. M. Van Stokkum, D. S. Larsen, and R. Van Grondelle, "Global and target analysis of time-resolved spectra," *Biochim. Biophys. Acta - Bioenerg.*, vol. 1657, no. 2–3, pp. 82–104, 2004.

[101] K. M. Mullen and I. H. M. Van Stokkum, "The variable projection algorithm in time-resolved spectroscopy, microscopy and mass spectrometry applications," *Numer. Algorithms*, vol. 51, no. 3, pp. 319–340, 2009.

[102] J. R. Caram and G. S. Engel, "Extracting dynamics of excitonic coherences in congested spectra of photosynthetic light harvesting antenna complexes," *Faraday Discuss.*, vol. 153, p. 93, 2011.

[103] A. Volpato and E. Collini, "Time-frequency methods for coherent spectroscopy," *Opt. Express*, vol. 23, no. 15, p. 20040, 2015.

[104] F. Milota, V. I. Prokhorenko, T. Mancal, H. Berlepsch, H. F. Kauffmann, J. Hauer, H. von Berlepsch, and O. Bixner, "Vibronic and Vibrational Coherences in Two-Dimensional Electronic Spectra of Supramolecular J-A ggregates," *J. Phys. Chem. A*,

vol. 117, no. 29, pp. 6007–14, 2013.

[105] S. T. Cundiff, "Optical three dimensional coherent spectroscopy.," *Phys. Chem. Chem. Phys.*, vol. 16, no. 18, pp. 8193–200, 2014.

[106] V. Butkus, D. Zigmantas, D. Abramavicius, and L. Valkunas, "Distinctive character of electronic and vibrational coherences in disordered molecular aggregates," *Chem. Phys. Lett.*, vol. 587, pp. 93–98, 2013.

[107] A. Chenu, N. Christensson, H. F. Kauffmann, and T. Mančal, "Enhancement of vibronic and ground-state vibrational coherences in 2D spectra of photosynthetic complexes.," *Sci. Rep.*, vol. 3, p. 2029, 2013.

[108] L. Bolzonello, "Ultrafast relaxation dynamics of multichromophoric systems trough advanced optical spectroscopies", PhD Thesis, 2016.

[109] B. Y. P. Ball, "quantum biology," *Nature*, vol.274, pp. 272–274, 2011.

Ringraziamenti

Desidero innanzitutto ringraziare la Prof.ssa Elisabetta Collini, per avermi dato la possibilità di entrare a far parte del suo gruppo di ricerca e per avermi permesso di collaborare, seppure in piccola parte, al lavoro di cui il gruppo si occupa con entusiasmo e dedizione. Vorrei esprimerle la mia gratitudine per la grande disponibilità e cortesia dimostratemi negli sviluppi del mio progetto di tesi e, in particolar modo, per il prezioso aiuto profuso nella stesura di questo elaborato.

Desidero inoltre ringraziare Andrea, Elena e Luca per il tempo dedicatomi e per aver seguito lo sviluppo di questo lavoro di tesi con infinita pazienza. Senza il loro supporto e i preziosi consigli l'esperienza di questi mesi non sarebbe stata la stessa. Ringrazio Cristina per il sostegno dimostratomi da amica e collega.

Un ringraziamento speciale va a mamma Adriana e papà Marcello, per avermi sostenuto instancabilmente negli studi e avermi incoraggiato davanti ad ogni difficoltà. È soprattutto grazie al loro sacrificio se ho potuto intraprendere questo percorso e portarlo a termine con serenità. Grazie a mio fratello Marco, che ha cercato di mettere a dura prova la mia pazienza, e per avermi spinto sempre a farcela da sola davanti ad ogni situazione. Grazie al fratellone Gianluca per l'estrema vicinanza e l'affetto con cui mi ha accudito.

Grazie ai compagni di questi anni universitari, in particolare a Jaci, Nicolò, Dengo, Angela, Riccardo, Dani, Alice per i lieti pomeriggi di studio in biblioteca, le interminabili pause, le grasse risate e soprattutto per aver condiviso le gioie e i dolori che questi cinque anni ci hanno regalato. Grazie ad Enrico, per essersi improvvisato nel ruolo di mentore in questo lungo percorso, e per la giusta dose di ansia di cui mi ha munito nelle svariate occasioni. Grazie a Stefano e Mattia, per aver allietato le lunghe pause caffè e le serate a Birrolandia, e per avermi dato modo di esprimere la mia più esuberante natura. Grazie a Federico, per aver dato un tocco di colore al grigiore delle giornate patavine con la sua folle compagnia. Grazie a Cesco per le lunghe chiacchierate e le immancabili 'paranoie'. Come non ringraziare Roberta, per la vicinanza e per non essersi smentita nel ruolo di compagna di sventure, anche a distanza, Ringrazio Giada, per l'amicizia e l'indescrivibile supporto dimostratimi, le innumerevoli confidenze e per essersi presa cura di me nei momenti di delirio e sconforto. Un ringraziamento speciale va a Rebecca, la persona con la quale più di tutte ho condiviso questa esperienza universitaria. È stato davvero difficile non poter trascorrere negli ultimi mesi intere giornate gironzolando per il dipartimento, inciampando dalle risate e interrogandoci sui perché delle mie sventure. Grazie per la vera amicizia dimostratami. Infine, ringrazio di cuore le amiche 'di una vita' Eulalia e Sara perché né il tempo né i kilometri di distanza sono riusciti ad intaccare il nostro legame.